

Development of piezo-resistive pressure sensors with hybrid printing methods

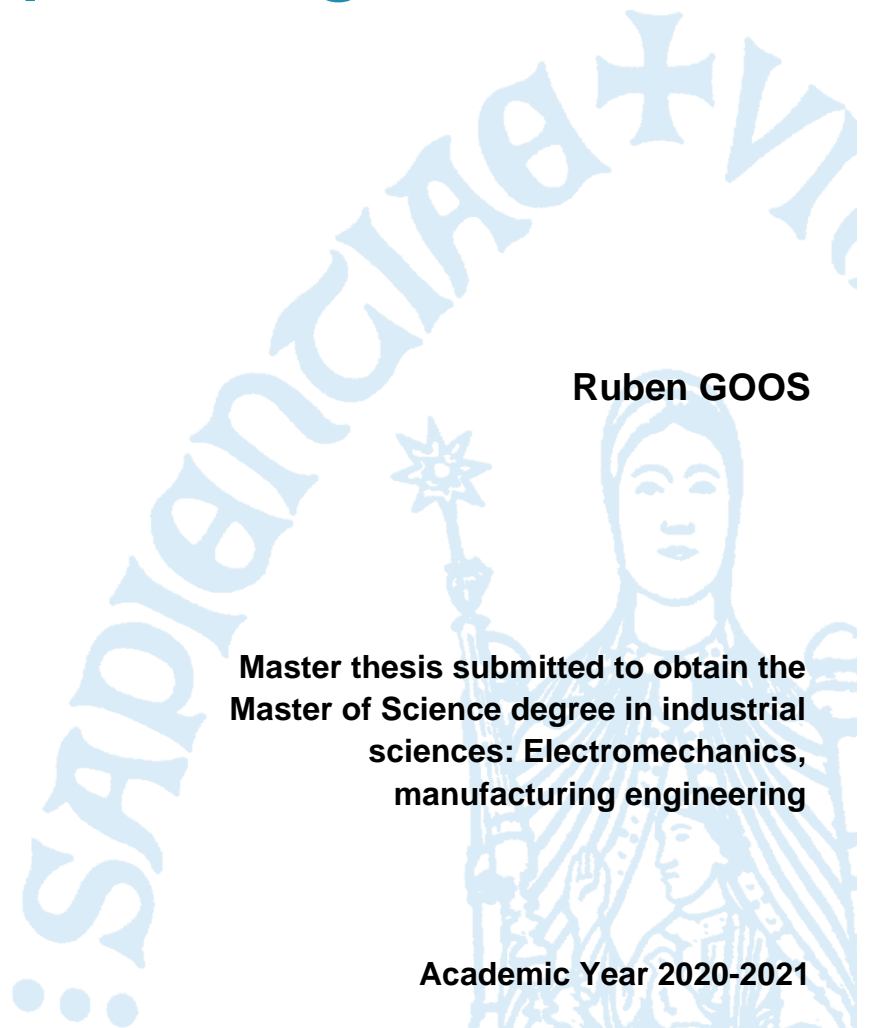
Master Thesis

Ruben GOOS

Promotor: Prof. E. Ferraris
Co-promotor: Eng. A. Verma

**Master thesis submitted to obtain the
Master of Science degree in industrial
sciences: Electromechanics,
manufacturing engineering**

Academic Year 2020-2021



© Copyright KU Leuven

Without written permission of the supervisor(s) and the author(s) it is forbidden to reproduce or adapt in any form or by any means any part of this publication. Requests for obtaining the right to reproduce or utilise parts of this publication should be addressed to KU Leuven, De Nayer (Sint-Katelijne-Waver) Campus, Jan De Nayerlaan 5, B-2860 Sint-Katelijne-Waver, +32 15 31 69 44 or via email fet.denayer@kuleuven.be.

A written permission of the supervisor(s) is also required to use the methods, products, schematics and programs described in this work for industrial or commercial use, and for submitting this publication in scientific contests.

Preface

In the master year, all the knowledge acquired during the study is brought together in the master thesis. I chose this master thesis topic because it offers a nice combination between theoretical aspects, experimental procedures, and the realization of functional components. The topic also fits well with my major in manufacturing engineering and my passion to create and improve. In this preface, I would like to thank everyone who was involved in this project and aided in its establishment during the difficult covid19 period.

First and foremost, I would like to express my gratitude to Prof. Eleonora Ferraris, who allowed me to work on this topic. As supervisor of this project, her comments and advice made sure that the focus was not lost during the thesis and enabled me to create a more critical way of thinking.

I would also like to express my sincere thanks to my co-supervisor Akash Verma. His deep knowledge of the topic and supervision were of key importance to the project. I also thank him for his guidance and assistance during the compression testing experiments.

Next, I would like to thank Miriam Seiti. Not only because her research on the NEBULA 5x-100s provided the base for my experimental determination of the printing parameters, but also because she kept me motivated when the machine was not performing as supposed. I would also like to thank Loren De Vogelaer. As the lab technician of the advanced manufacturing laboratory of KU Leuven Campus De Nayer, he was always around to give critical insights or support where needed. I am also thankful for the guidance that Jie Zhang offered in writing the Matlab code for the data processing.

Finally, I would like to thank all students and Ph.D.'s who were working at the lab. Their presence created a pleasant working atmosphere where there was room for laughter between the experiments.

I am grateful for the wonderful years I have had at De Nayer. These would not have been the same without the close friends I made and the professors and teachers who all earned my gratitude.

Samenvatting

Het doel van dit onderzoek is de validatie van geprinte druk sensoren en de implementatie van deze sensoren op gekromde oppervlakken. De werkwijze van de sensoren berust op het piezo-resistieve effect waarbij de weerstand afhankelijk is van de aangelegde compressie op het desbetreffende piezo-resistieve materiaal. De sensoren zijn geproduceerd met een hybride proces dat gebruik maakt van Aerosol Jet Printing (AJP) en screen print technieken. Voor het printen van de elektroden van de sensoren werd gebruik gemaakt van de NEBULA 5X-100s aerosol jet gebaseerde printer. Dit is een 5-assige machine die de voorbij jaren ontwikkeld en geoptimaliseerd werd aan de advanced manufacturing onderzoeksgroep van KU Leuven Campus De Nayer. Dit toestel is ontwikkeld om een kost efficiënt alternatief te bieden voor het printen van elektronica die minder nauwkeurigheid vereist (~150-200µm) dan wat de beschikbare toestellen op de markt aanbieden (~20 µm).

Deze thesis is opgebouwd uit een literatuurstudie, een onderzoek naar de eigenschappen van geprinte piezo-resistieve sensoren en een experimentele fase waarin piezo-resistieve sensoren ontwikkeld worden op gekromde oppervlakken. In de literatuurstudie is de focus verdeeld over drie aspecten. Eerst wordt er aandacht besteed aan het AJP proces dat gebruikt is voor de productie van de sensoren. Vervolgens wordt er meer informatie gegeven over de piezo-resistieve sensoren en diens eigenschappen. Tenslotte volgt een korte uiteenzetting over het printen op gekromde oppervlakken gebruik makende van het AJP proces.

De eigenschappen van de piezo-resistieve sensoren werden onderzocht doormiddel van compressietesten met variërende input parameters. Vervolgens werd er een configuratie van piezo-resistieve sensoren ontwikkeld op een gekromd oppervlak. Hiervoor is gebruik gemaakt van de NEBULA 5X-100s aerosol jet gebaseerde printer, dewelke eerst enkele verbeteringen onderging om het printgemak te bevorderen. Vervolgens werden op experimentele wijze de optimale printparameters bepaald om CUR Ag-001 zilver inkt te printen op Polyamide (PA) substraat. Er werd ook een validatie van de 5-assige postprocessor uitgevoerd aangezien er voor de eindapplicatie geprint werd op gekromde oppervlakken. Omdat deze echter niet naar behoren werkte is het vervolg van deze thesis uitgevoerd met de 3-assige postprocessor. Vervolgens is het ontwerp voor de sensor configuratie gemaakt m.b.v. Creo, waarna de g-code gegenereerd is met de aangepaste 3-assige postprocessor. De productie van de uiteindelijke sensor op het gekromde PA-substraat kwam tot stand door een combinatie van AJP en screen print technieken.

Er kan geconcludeerd worden dat sensor karakteristieken zoals gevoeligheid, hysteresis, herhaalbaarheid en tijdsdrift een aanzienlijke invloed hebben op de output waarde van de sensor. Verder kunnen we vaststellen dat, gebruik makende van een combinatie van AJP en screenprint technieken, het mogelijk is om functionele piezo-resistieve druk sensoren te produceren op gekromde oppervlakken.

Abstract

The goal of this thesis is the validation of printed piezoresistive pressure sensors and the implementation of these sensors on non-planar substrates. The sensors are produced using a hybrid manufacturing method of Aerosol Jet Printing (AJP) and screen-printing techniques. The NEBULA 5X-100s aerosol jet based printer is used for the production of the sensor electrodes. This is a 5-axis machine that, over the past years, was developed and improved at the advanced manufacturing research group of KU Leuven Campus De Nayer.

This thesis is composed of a literature review, an investigation of the properties of printed piezoresistive sensors, and an experimental phase in which piezoresistive sensors are developed on curved surfaces. The literature review addresses the Aerosol Jet Printing process, piezoresistive sensor properties, and printing on non-planar surfaces using AJP. The properties of piezoresistive sensors are investigated through compression tests with varying input parameters. Next, a configuration of piezoresistive pressure sensors is developed onto a non-planar PA substrate using a combination of AJP and screen-printing techniques.

It was found that, using a combination of aerosol jet-based and screen printing techniques, it is possible to produce functional piezoresistive pressure sensors onto non-planar substrates.

Keywords: Printing of electronics, Aerosol Jet Printing, screen printing, Piezoresistive pressure sensor, hybrid manufacturing

Table of contents

1	Introduction	1
1.1	<i>Problem statement</i>	1
1.2	<i>Goals and objectives</i>	2
2	State of the art	3
2.1	<i>Introduction to printed electronics.....</i>	3
2.1.1	<i>Indirect printing techniques</i>	4
2.1.2	<i>Direct printing techniques.....</i>	5
2.2	<i>Aerosol Jet printing</i>	6
2.2.1	<i>Introduction to Aerosol Jet Printing.....</i>	6
2.2.2	<i>Inks and substrates</i>	7
2.2.3	<i>Working principle of Aerosol Jet printing</i>	10
2.2.4	<i>Factors affecting deposition</i>	13
2.2.5	<i>Pre-and-post-printing treatments.....</i>	15
2.2.6	<i>Applications.....</i>	18
2.3	<i>Piezoresistive sensors.....</i>	20
2.3.1	<i>Introduction</i>	20
2.3.2	<i>Working principle of piezoresistive material.....</i>	21
2.3.3	<i>Piezoresistive sensor configurations</i>	23
2.3.4	<i>Typical sensor characteristics</i>	24
2.4	<i>Freeform printing.....</i>	27
2.5	<i>Conclusion of the state of the art.....</i>	29
3	Materials and methods.....	30
3.1	<i>Project flow and methodological approach</i>	30
3.2	<i>Fabrication of the pressure sensor on planar substrate</i>	31
3.2.1	<i>Inks and substrates</i>	31
3.2.2	<i>Production process</i>	32
3.3	<i>Experimental setup mechanical testing</i>	32
3.3.1	<i>General setup</i>	32
3.3.2	<i>Setup improvements</i>	34
3.3.3	<i>Experimental conditions</i>	34
3.4	<i>Printing process and conditions.....</i>	36

3.4.1	NEBULA 5X-100s AJP	36
3.4.2	Improvements on the NEBULA 5X-100s	37
3.4.3	Inks and substrates	39
3.4.4	Determining printing parameters for the PA substrate	40
3.5	<i>Production of sensing device on non-planar substrate</i>	41
3.5.1	Sensor design	41
3.5.2	Screen printing of the piezoresistive ink	42
3.5.3	Coupling with the readout circuit	43
4	Experimental results and discussion	44
4.1	<i>Experimental results compression testing</i>	44
4.1.1	Ramping force.....	44
4.1.2	Hysteresis	45
4.1.3	Time drift testing	46
4.1.4	Cyclic force	46
4.1.5	Conclusion	47
4.2	<i>Printing parameters NEBULA 5X-100s</i>	47
4.2.1	Results prior experiments.....	47
4.2.2	Results final experiment.....	48
4.2.3	Conclusion	48
4.3	<i>Production of the sensor circuit</i>	49
4.3.1	AJP of the sensor electrodes	49
4.3.2	Screen printing of the piezoresistive material	52
4.3.3	Coupling with the readout hardware.....	52
4.3.4	Validation sensor circuit	53
5	Validation 5-axis movement NEBULA 5X-100s	55
5.1	<i>Experimental procedure and results of the machine movements</i>	55
5.2	<i>Investigation of the postprocessor</i>	56
5.3	<i>Improvements postprocessor</i>	58
5.4	<i>Conclusion</i>	58
6	Conclusion and future work	59
6.1	<i>Conclusion</i>	59
6.2	<i>Perspectives and future work</i>	60
	List of figures	61
	List of tables	64

Bibliography	65
Appendix.....	71
Appendix A: Procedures.....	1
Appendix B: Technical drawings	10
Appendix C: Matlab scripts	17
Appendix D: Experimental results	23
Appendix E: G-code	27
Appendix F: Datasheets.....	32

Symbol list

cP	Centipoise	[mPa·s]
wt. %	Mass fraction	[%]
ρ	Density	[kg/m ³]
A	Cross sectional area	[m ²]
V	Volume	[m ³]
w	Width	[m]
t	Thickness	[m]
FR	Focusing ratio	[%]
sccm	standard cubic centimeters per minute	[cm ³ /min]
R	Resistance	[Ω]
θ	Wetting angle	[$^{\circ}$]
R _a	Average roughness	[m]
R _z	Peak to peak roughness	[m]
f	Frequency	[Hz]
F	Force	[N]
h	Plank's constant	[J s]
e	Electron charge	[C]
m _e	Electron mass	[kg]
P	Pressure	[Pa]
J	Tunneling current	[A]
ϕ	Energy barrier of the polymer	[eV]
S	Distance between nanoparticles	[m]
R _m	Tunneling resistivity	[Ω]
R _c	Resistance across a conductive filler particle	[Ω]
a ²	Contact area between conductive filler particles	[m ²]
σ	Stress	[Pa]
E	Elasticity modulus	[Pa]
D	Conductive filler diameter	[m]
ϑ	Filler volume fraction	[%]

List of abbreviations

AJP	Aerosol jet printing
AM	additive manufacturing
AgNW	Silver nano wires
CAM	Computer aided manufacturing
CIJ	Continuous ink jet
CNT	Carbon nano tubes
DOD	Drop on demand
DW	Direct write
FR	Focusing ratio
GF	Gauge factor
IC	Integrated circuit
IPL	Intense pulsed light sintering
LCD's	Liquid crystal displays
LDW	Laser direct write
MIMIC	Micro molding in micro capillaries
OLED	Organic light emitting diode
P3HT	Poly 3-hexylthiophen
PA	Poly amide
PDMS	Polydimethylsiloxane
PE	Printed electronics
PEDOT/PSS	Poly (3,4-ethylenedioxythiophene) polystyrene sulfonate
PEEK	Polyetherketone
PEN	Polyethylene naphthalate
PET	Polyethylene terephthalate
PI	Polyimide
PMMA	Poly methyl methacrylate
PTFE	Polytetrafluoroethylene
REM	Replica molding
SAMIM	Solvent Assisted Micro Molding
TFT	Thin Film Transistors
UV	Ultraviolet
μ TM	Micro Transfer molding

1 INTRODUCTION

1.1 Problem statement

Nowadays, there is a rising demand for electronics with improved characteristics when it comes to size and energy consumption. Because conventional IC manufacturing techniques are already intensively optimized and have their limitations when it comes to form factors, the industry is looking for alternative techniques to produce electronics [1]. In the past decades, (PE) has gained interest because of its possibility to produce large-area high-quality products that are thin, flexible, lightweight, cost-efficient, and environmentally friendly [1]–[3]. Nowadays there are a lot of different direct and indirect printing techniques, which are already widely used in the industry to create all kinds of components like switches, antennas, and sensors [4]. The direct printing techniques are especially interesting because they allow for a mask-less printing technique, which in some cases can be used to produce electronics on freeform substrates. For example, Optomec® has developed Aerosol Jet® Printers that can perform 5-axis printing [5], [6]. In this text we generically refer to the aerosol jet based printing technology with the abbreviation AJP. This technique was implemented in the own build Nebula 5X-100s aerosol jet-based printer. Instead, the Aerosol Jet® Printing technique developed by Optomec® is abbreviated with AJ®P, and is used for specific parts of the state of the art and the production of the pressure sensors on the planar substrates in the experimental part of this thesis.

At the Advanced Manufacturing Lab (AML) of the Catholic University Leuven (KUL), researchers have developed a pressure sensor, using a combination of AJ®P and screen-printing techniques. Some testing of the sensor has already been done, but further testing is required to establish its full characterization. The final application of the pressure sensor is to measure the correct position of a medical device. This way one can control if the fit between the patient and the medical device is within tolerance by looking at the output value of the sensor.

The current pressure sensor is printed on a flat and smooth surface. The medical device will be made from polyamide, using a 3D printing technique. The surface of the tool will thus be curved and porous. Further investigation is required to produce the sensor on this curved and porous substrate. To determine the pressure applied to the sensor, a readout circuit has been developed in cooperation with Thomas More. In order to use it, a coupling between the pressure sensor and the readout system must be developed.

1.2 Goals and objectives

The main goal of this master thesis is to get a better understanding of the characteristics of printed sensors and the development of a process that allows us to print on curved substrates with the home build aerosol jet-based printer (NEBULA 5X-100s). The characteristics of the pressure sensor on the flat substrate will be determined through testing. Research will be conducted towards parameters as sensitivity, hysteresis, repeatability, and time drift. What is out of scope are temperature and humidity drift testing and UV degradation testing of the sensor. Research will also be conducted to print adequate lines on a curved substrate using the NEBULA 5X-100s aerosol jet-based printer. In these experiments, the influence of input parameters like the number of deposited layers, printing speed and carrier gas flow rate will be determined. What's out of scope is the influence of the focusing ratio, because this is a feature that the machine lacks. Also, the nozzle size is out of scope because this is investigated in previous work. Since the goal is to print on non-planar substrates, validation of the 5-axis postprocessor must be conducted. Using the results of the previous experiments, the piezoresistive sensor will be produced on a curved PA substrate using a combination of AJP and screen-printing techniques. Finally, a coupling between the readout circuit and the sensor is provided. The objectives can be listed as follows:

- 1) Characterization of the piezoresistive pressure sensors on the flat PA substrates, which are produced by a combination of Aerosol Jet[®] Printing (AJ[®]P) and screen-printing techniques.
- 2) Research towards printing on a non-planar porous substrate using the NEBULA 5X-100s aerosol jet-based printer. This implies determining the proper printing parameters and a validation of the 5-axis postprocessor.
- 3) Development and production of the piezoresistive pressure sensor array onto the curved PA substrate using a combination of aerosol jet-based printing and screen-printing techniques.
- 4) Development of a connection between the piezoresistive pressure sensor array and readout hardware.

2 STATE OF THE ART

This chapter contains an overview of the state of the art information on the key topics of this work. First, an introduction to printed electronics is given in section 2.1 with respect to the applications, market, and printing techniques. In section 2.2, the working principle of the AJP process is described along with the possible inks, substrates, and the pre and post-processing treatments. Section 2.3 describes the working principle of piezoresistive pressure sensors and their typical characteristics. Finally, an overview of freeform printing is given in section 2.4.

2.1 Introduction to printed electronics

Printed electronics (PE) is an additive deposition technology where functional material is deposited onto a substrate to form electronic components and circuits. The aim of PE is to make electronic components and circuits using printing technology instead of conventional etching techniques, in order to reduce prototyping cost and ensure a shorter time to market. In fact, PE is no new technique, it's first use dates back to 1950 [1]. In the past decades, PE has gained interest because of its possibility to make large area high-quality products that are thin, flexible, lightweight, cost-efficient, and environmentally friendly [1]–[3]. This leads to the next generation of electronics that are conform to the curves of the human body. Nevertheless, according to Khan et al. [2], PE is not as efficient for signal communication and computation as silicon ICs. They also report that PE suffers from higher power consumption, limited lifetime, and lower performance. On the other hand, PE can be produced using quick and flexible techniques, as will be discussed later, which enables on-demand production and rapid prototyping. Considering all these advantages, it is no surprise that PE-technology is already widely used for industrial applications as printed sensors (pressure, strain, ...) [7], [8], active components like thin-film transistors (TFT) [9], printed antennas for wireless communication, printed energy harvesting and storage (organic solar cells and batteries) [10] and printed displays (OLED) [11]. IDTechEx [3] projected the printed electronics market to grow to US\$96B against the year 2020. The values of other major sectors in the printed electronics business like printed photovoltaics, radio frequency identification, and flexible displays, are illustrated in Table 2.1.

Table 2.1: Market of printed electronics (values from [12], [13])

Year	Market	Value
2020	Printed electronics (general)	\$96B
2017	Printed photovoltaics	\$8B
2016	Radio frequency identification	\$2B
2012	Flexible displays	\$2B

There are many printing techniques available to produce PE applications, which all have their advantages and disadvantages. According to Cruz et al. [4], the choice depends on the desired type of the electronic component (large, small, flexible, ...), the production volume, cost, processability, performance, and reliability. Printing techniques for PE can be divided into direct and indirect printing (Figure 2.1). Indirect printing is a technique where a mask or screen is required to selectively deposit the ink onto the substrate. Direct printing makes no use of a

mask or screen, which is also named a mask-less technique. The following subchapters address those aspects more in detail.

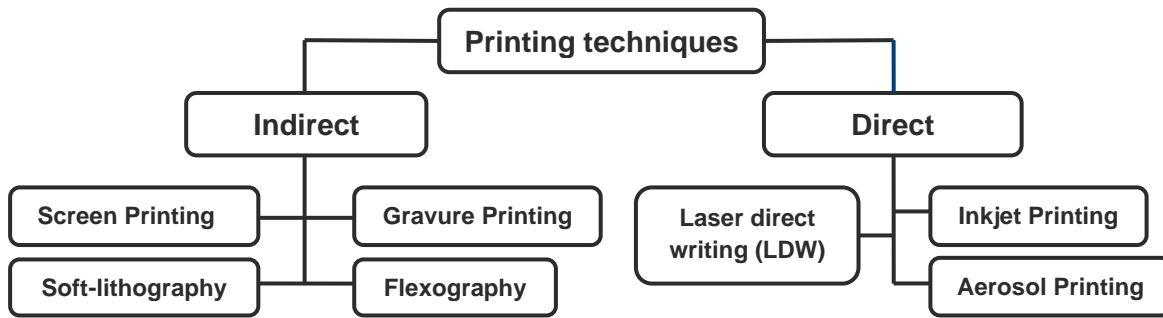


Figure 2.1: Classification of printing techniques for PE [1] [4]

2.1.1 Indirect printing techniques

When an indirect printing method is implemented, the printing process is based on a replication process. Patterns will be transferred to the substrate by means of a master plate which cannot be altered once made. Every print made with the master plate will be identical (within a certain tolerance), which makes this technique ideal to use for high-volume productions [14]. According to Cruz et al. [4], indirect printing techniques are the most commonly used, although they involve restrictions in resolution and the range of used materials (inks, substrates, solvents). Depending on the difference in master plate, indirect printing can be divided into techniques as screen printing, gravure printing, soft lithography, and flexography (Table 2.2).

Table 2.2: Indirect printing techniques

Printing technique	Operating principle	Resolution
Screen Printing [1] [4] [15] [16]	<ul style="list-style-type: none"> Ink is pushed through a screen using a squeegee to form the desired pattern on the substrate. The screen consists of a mesh with stencil. Can be done with a planar or roll-to-roll technique 	30-100 μm
Gravure Printing [4]	<ul style="list-style-type: none"> Roll-to-roll direct relief printing. Substrate passes through impression and gravure cylinder. The pattern is applied in the negative form onto the gravure roll as a sequence of cavities. The gravure roll is submerged into the ink, filling the cavities. Excess ink is scraped off using a doctor blade. 	1-10 μm
Soft Lithography [4] [17] [18]	<ul style="list-style-type: none"> Generic term which includes replica molding (REM), micro-transfer molding (μTM), micro-molding in micro capillaries (MIMIC), and solvent assisted micro-molding (SAMIM). Master mold is made using lithography, which is used to produce multiple stamps with patterned relief structures. Stamp is used to transfer pattern onto substrate. 	<0.1 μm

Flexography [1] [15] [16]	<ul style="list-style-type: none"> • Roll-to-roll direct relief printing. • Substrate passes through impression cylinder and flexible printing plate mounted on a cylinder. • The pattern is applied positively onto the printing plate by a relief structure. • Ink is transferred to the printing plate by an anilox roller. • Lower printing pressure makes it possible to print on flexible substrates. 	5-50 μm
-------------------------------------	--	--------------------

2.1.2 Direct printing techniques

The main difference when using direct printing is that there is no master plate needed. The ink is deposited directly onto the substrate, which lowers the risk of contaminating or damaging the substrate. This means that direct printing is an excellent technique for flexible printing and with the potential of making multi-layered devices. According to Wadhwa et al. [14], indirect printing techniques are also limited to two-dimensional deposition, while direct printing techniques allow printing onto three-dimensional substrates. Direct printing uses a digital image under the format of a CAM file to define the printed pattern. This results in a more flexible technique with lower setup and manufacturing costs [4]. Direct printing can be divided into multiple techniques such as Laser direct-write, inkjet printing, and Aerosol Jet Printing (AJP) as listed in Table 2.3.

Table 2.3: Direct printing techniques

Printing technique	Operating principle	Resolution
Laser direct-write (LDW) [1] [19] [20]	<ul style="list-style-type: none"> • Laser-induced deposition of ink on the substrate. • Pulse laser transfers ink from optical transparent donor substrate to acceptor substrate. • The pattern is created by the translation of donor and acceptor substrate. • Resolution is dependent on the focus of the laser. 	<0.1 μm
Inkjet Printing [4] [15] [21]	<ul style="list-style-type: none"> • The ink is sprayed directly onto the substrate. • The ink is of low viscosity and consists of metal nanoparticles dispersed into a solvent. • Continuous inkjet (CIJ): Flow of ink droplets that are controlled by an electrostatic field. • Drop on demand (DOD): Ink is ejected when a pulse is applied to a pressure transducer. 	20-200 μm
Aerosol Jet Printing (AJP) [15] [14]	<ul style="list-style-type: none"> • Aerosolized ink is jetted directly onto the substrate according to a given pattern. • Wide range of printable inks. • Ultrasonic or pneumatic atomization. 	5-30 μm

2.2 Aerosol Jet printing

This chapter contains state of the art information about the Aerosol Jet Printing process. First, an introduction to the printing process is given with respect to the general working principles and factors influencing the process. Next, the available inks and substrates which can be used for the AJP process are discussed. Then, the working principles and parameters affecting the deposition are explained. Afterwards, pre and post-processing techniques are discussed. Finally, some industrial applications for AJP are given.

2.2.1 Introduction to Aerosol Jet Printing

Aerosol Jet[®] Printing (AJ[®]P) is a relatively new, direct writing, printing technique developed by Optomec[®] Inc. In the recent years AJP has gained interest, due to its advantages as high resolution, flexibility, and a wide variety of printable inks [15]. With an ink viscosity that ranges from 1 to 2500 cp, [22] a wide variety of materials can be printed such as metal inks [23], ceramic inks [24], conductive polymers [25] and biological matter [26]. In the AJP technique, the ink is first placed into an atomizer where it is aerosolized into small liquid particles. Next, the aerosolized ink is transported to the nozzle where it is focused and deposited onto the substrate. Unlike inkjet printing, which uses a stream of ink droplets to form a pattern, AJP forms a pattern using a continuous jet of aerosolized ink. The AJP technique can print with writing speeds up to 200mm/s and a deposition rate of 0,25mm²/s. While printing, a nozzle-to-substrate stand-off distance of 1-5mm should be maintained [27]. According to Hoey et al. [28], this large range in stand-off distance makes it possible to print complex designs onto non-planar substrates, using a 5-axis platform. The main differences in properties between ink jet printing and Aerosol Jet printing are illustrated in Table 2.4.

Table 2.4: Comparison between the properties of Ink Jet and Aerosol Jet printing. [14][27][29]

Properties	Ink Jet	Aerosol Jet Printing
Print speed (mm/s)	Up to 5000	Up to 200
Throughput (m ² /s)	0.01-0.5	0.01-0.5
Line width (μm)	2-200	5-30
Feature size (μm)	>30	10-200
Ink viscosity (cP)	10-20	0.7-2500
Metal loading (wt.%)	<20	>60

The goal of AJP is to produce objects (circuits, antennas, electrodes, ...) of optimal quality while reducing the variation in output, just like with any other production technique. This is especially important for the final application of this thesis where a sensor circuit will be produced using aerosol jet-based printing. According to Mahajan et al. [30] (Figure 2.2), the quality of deposition is dependent on multiple factors like apparatus, process, design, material, substrate, and environment. According to Wilkinson et al. [31], Factors like the apparatus, design, and process are considerably easy to control, while factors like the substrate and environment are less predictable. The control of material properties presents the biggest challenge. According to Wadhwa et al. [14], temperature instability and solvent evaporation of the ink cause material-related fluctuations like pre-drying of the ink and material build-up in the

nozzle. This can also be caused by a change in environmental temperature or relative humidity. Other causes for these material-related fluctuations are the material/solvent ratio and the type of solvent, as will be explained in section 2.2.2 along with the substrates. The apparatus and process are explained respectively in section 2.2.3 and 2.2.4, while more information about the design is provided in section 2.3.3.

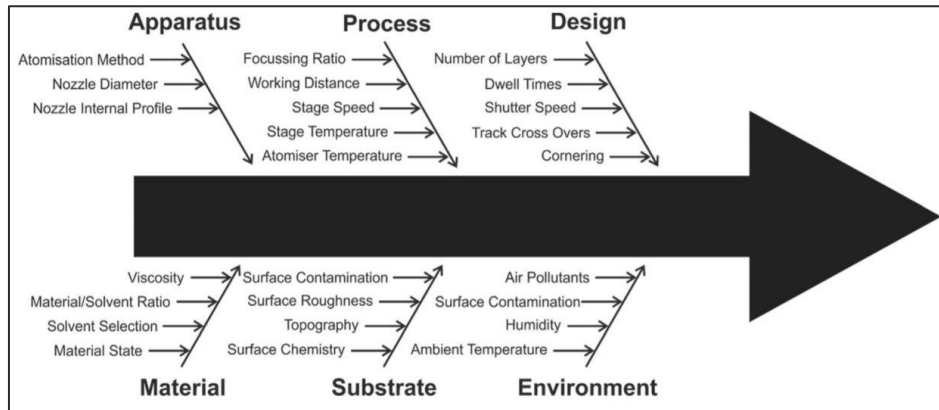


Figure 2.2: Influencing parameters on the AJP process [30]

2.2.2 Inks and substrates

This chapter provides knowledge about the ink and substrate properties and addresses frequently used inks and substrates for the AJP process, as described in the literature.

2.2.2.1 Inks for AJP

Using the Pneumatic AJP technique, which will be used in the experimental part of this thesis and is discussed in section 2.2.3, inks can be printed with viscosities ranging from 0.7 to 2500cp and particle sizes up to 500nm. This results in a wide range of materials that can be deposited such as metal nanoparticles, conductive polymers, carbon nanotubes, ceramics, and biological materials. To print, the ink must be formed in a dense and homogenous aerosol, and have good adhesion to the substrate. The ink must be chosen according to the desired characteristics of the printed application (low resistivity, biocompatible, ...), and is typically composed out of nanoparticles (conductive or not conductive) dispersed or dissolved into a solvent (water or organic). According to Kamysny et al. [32], the nanoparticles provide the desired properties to the printed lines, while the solvent determines the properties of the ink. The solvent must be selected according to the intended application, e.g. 2D or 3D printing. The dispersion of the nanoparticles in the solvent should be stable to obtain an ink with predictable performances. To obtain this, the addition of a stabilizing agent is required. Wettability, viscosity, and surface tension are important ink characteristics because they determine the drop size, wetting of the printed lines on the surface, and print accuracy [32]. To improve the ink characteristics, other additions can be made such as anti-foaming agents (which causes breakdown of present foam), wetting agents (to improve wettability), surfactants (to reduce the viscosity and surface tension) [33] and dispersants (to reduce coagulation) [14].

Due to their large surface-to-volume ratio, aerosol droplets lose a lot of solvent when brought in contact with a dry gas stream. This brings forward the challenge to control the evaporation throughout the entire printing process. As the solvent is lost during the process (atomization, transportation, and deposition), the physical properties of the ink, such as solid loading fraction and viscosity will be altered. Yang et al. [25] reported that the use of a high volatility solvent

can result in the complete evaporation of this solvent. The pattern is then produced with dry nanoparticles and has a high number of porosities and surface roughness. Through evaporation, a loss of droplet mass can also lead to ink droplets with insufficient inertia to be impacted on to the substrate. To produce a qualitative print, a thin liquid layer must be formed onto the substrate which has to be dried afterward. This is achieved by the combination of high and low-volatility solvents. The high volatility solvent evaporates after atomization and saturates the carrier gas. This leads to stable droplet volumes in the aerosol during transport. When the aerosol is brought in contact with the sheath gas, the low-volatility solvent will start to evaporate. Complete evaporation of the solvent before deposition can be avoided by adding 10% of low-volatility solvent to the ink.

According to Wadhwa et al. [14], inks containing a high volatility solvent can be used to create small feature sizes (below 20 μm). The high volatility solvent evaporates faster, resulting in fast drying of the in-flight droplets. This results in a narrower deposition width. On the other hand, inks containing a low volatility solvent have a longer drying time and can be used when a more uniform ink spread is desired.

When it comes to the printing of electronics a few types of ink are especially important. Conductive metal and conductive polymer ink will be used in the experimental section of this thesis and are discussed here more in detail. An overview of the most important inks is summarized as follows:

Conductive metal ink is widely used for the production of connectors, electrodes, antennas, etc. because of its high conductivity. It typically consists of metal nanoparticles dispersed in a highly volatile solvent. Metals that are often used are gold (Au), silver (Ag), copper (Cu), and aluminum (Al) with conductivities of respectively 2.44, 1.59, 1.72, and 2.65 $\mu\Omega\cdot\text{cm}$ [15]. Since there is only a slight difference in conductivity, other factors such as cost and chemical inertness become deciding parameters. Because of its low cost (compared to gold) and its high conductivity and chemical inertness, silver is the most used material when it comes to metal ink.

Conductive polymer ink is composed out of organic material which possesses low conductivity compared to metals. Nevertheless, they are very interesting for the production of electronics because they are flexible, soft, inexpensive, and lightweight. Because of its superior conductivity, thiophene (PEDOT/PSS) is the most common used conductive polymer for PE. PEDOT itself is insoluble, but with the addition of polystyrene sulfonic acid (PSS) it can be dispersed in an aqueous solvent. Kim et al. [34] were able to produce transistors using PEDOT/PSS. To increase the conductivity of PEDOT/PSS, Alemu et al. [35] proposed a simple film treatment with methanol which increases the conductivity by four orders of magnitude.

Semiconductive ink is widely used to produce thin-film transistors (TFT's) and liquid crystal displays (LCD's). The semiconductive inks can be divided into p-type and n-type semiconductors. P-type semiconductors are positively charged and thus have a larger hole concentration than electron concentration. N-type semiconductors are negatively charged and thus have a larger electron concentration than hole concentration [15]. According Li et al. [36], poly 3-hexylthiophen (P3HT) is extensively used as a semiconductor due to its good stability and solubility.

Dielectric ink is also used in the production of printed electronics. It can serve as a capacitance or insulating layer. According to Hedges et al. [37] commonly used materials are epoxy, acrylic, PMMA, polyimide, and PTFE.

2.2.2.2 Substrates for AJP

The substrates on which can be printed play a vital role in the applications for printed electronics. With the use of the AJP technique, it is possible to print on both flat and curved substrates as proven by Blumenthal et al. [38] who printed heating elements onto the leading edge of a rotor blade. The substrate can be chosen according to the final application or compatibility with the printing process. Important substrate characteristics are flexibility/stiffness, surface roughness, transparency, low thermal expansion, heat resistance, and cost.

Rigid substrates are most traditionally used in the manufacturing of electronics. But AJP also allows us to manufacture electronics on curved, flexible, and even stretchable substrates.

Flexible substrates can be used when the electronics must be bendable or attachable to a curved surface. Cao et al. [39] were able to produce thin-film transistors (TFT's) on a flexible Kapton sheet using the AJP process. The Kapton substrate was cleaned with isopropyl and deionized water. Next, conducting silver ink was printed onto the substrate and sintered in an oven at 150°C for 60min.

Stretchable substrates are often used for wearable or human health monitoring devices. According to Qingshen et al. [40], stretchable conductive materials or flexible designs must be used to survive stretching and maintaining reasonable conductivity. Shweta et al. [41] were able to produce flexible wearable strain sensors onto Opsite Flexgrid® substrate using AJP. The silver nanoparticle ink was locally laser sintered to increase conductivity without damaging the substrate. They reported that the sensor is stretchable and can detect large induces strain.

Some of the most commonly used substrate materials are summarized in the following table:

Table 2.5: Commonly used AJP substrates and their characteristics

Substrate	Thickness [μm]	Transparency [%]	Process temperature limit [°C]	Notes
Glass [1]	30-700	90	400	<ul style="list-style-type: none"> • Widely used for displays • Brittle and heavy weight
Paper [1][2]	20-250	-	130	<ul style="list-style-type: none"> • Flexible • Biodegradable
PET [40][2]	16-100	90	80	<ul style="list-style-type: none"> • Flexible plastic film • Low heat resistance
PEN [40][2]	12-250	87	120	<ul style="list-style-type: none"> • Flexible plastic film • Low cost
PEEK [40][2]	12-1500	54	143	<ul style="list-style-type: none"> • Flexible plastic film • Expensive
PI [40][2]	12-125	-	300	<ul style="list-style-type: none"> • Flexible plastic film • High heat resistance
Steel [1]	200	-	600	<ul style="list-style-type: none"> • Flexible/stiff • Heat resistant

2.2.3 Working principle of Aerosol Jet printing

This section gives a detailed explanation of the working principles behind the Aerosol Jet Printing process.

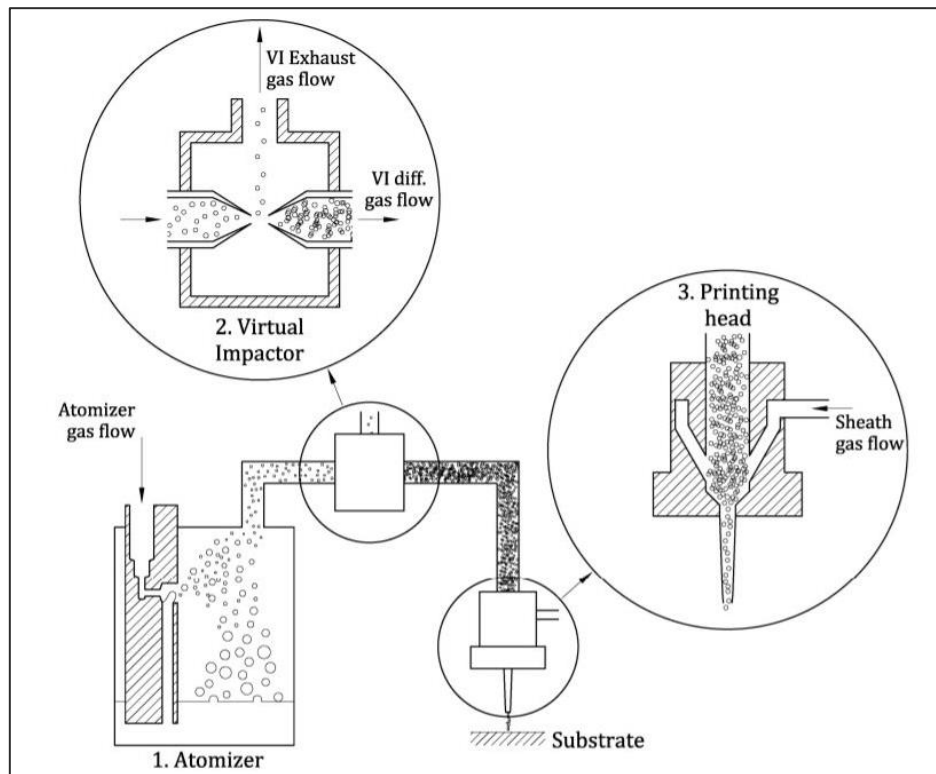


Figure 2.3: Schematic illustration of the pneumatic Aerosol Jet printing process [42]

First, the ink inside the atomizer is transformed into an aerosol. Depending on the type of atomizer, atomization can be done ultrasonically or pneumatically. In a pneumatic system, which is of interest for this work (Figure 2.3), the aerosol is transported to the virtual impactor. The virtual impactor is a component that reduces the aerosol flow by diverging some of the carrier gas and some fine aerosol droplets to an exhaust flow. This results in a homogeneous and dense mist, which is then fed to the nozzle where it is deposited onto the substrate [42]. When an ultrasonic atomizer is used instead of a pneumatic atomizer, no virtual impactor is required, and the aerosol flow is transported directly to the printing head.

2.2.3.1 Atomizer

In the atomizer, the ink is transformed into an aerosol, which is a state where liquid ink droplets are suspended in a carrier gas (mostly pressurized air or nitrogen). According to Wilkinson et al. [31], the aerosol would be ideally monodispersed, meaning that all ink droplets are of uniform size, and have a high density of ink droplets which are large enough to be deposited onto the substrate, but not so large that they cause nozzle clogging or a reduction in print resolution. Aerosolization can be achieved by either an ultrasonic or pneumatic atomizer. A comparison of characteristics between the pneumatic and ultrasonic atomizers is given in Table 2.6.

Table 2.6: Comparison between pneumatic and ultrasonic atomization [14][29]

Properties	Pneumatic atomization	Ultrasonic atomization
Ink viscosity (cP)	0.7-2500	0.7-10
Ink particle size (nm)	50-500	<50
Max. ink solid load (wt.%)	75	55
Type of ink solvent	Low vapor pressure (<13Pa) and high boiling point (>180°)	High vapor pressure and low boiling point (volatile)
Possible materials	<ul style="list-style-type: none"> • Metal ink • UV curable epoxy • Carbon resistor paste 	<ul style="list-style-type: none"> • Metal ink • Aqueous ink • Organic semiconductor

Ultrasonic atomizer

According to Wadhwa et al. [14], in an ultrasonic atomizer, a vial of low viscosity ink (0.7-10cp) with maximal particle sizes of 50 nm [14] is suspended above a piezoelectric transducer which is submerged in a transfer medium. As the piezoelectric transducer oscillates at high frequencies, it produces high-frequency pressure waves which propagate through the transfer medium (mostly water) to the vial of ink. Inside the vial, this results in standing waves on the ink surface. According to Wilkinson et al. [31], the superposition of multiple standing waves inside the bottle results in the formation of large peaks on the ink surface. Due to shear, the tips of those peaks are pinched, resulting in the formation of small droplets. These droplets are then suspended in the carrier gas, creating an aerosol that is driven to the deposition head. The working principle of an ultrasonic atomizer is schematically illustrated in Figure 2.4. According to Mette et al. [23], this technique typically produces aerosols of low density with droplet sizes ranging from 2 to 5 μm .

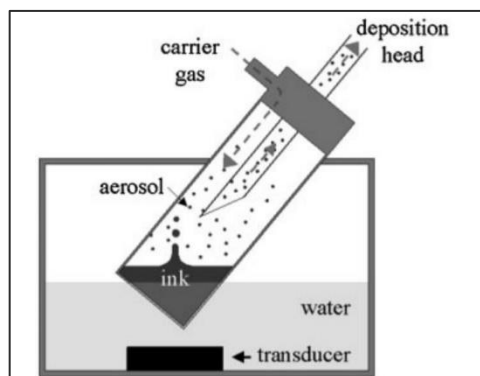


Figure 2.4: Schematic illustration of the ultrasonic atomizer [23]

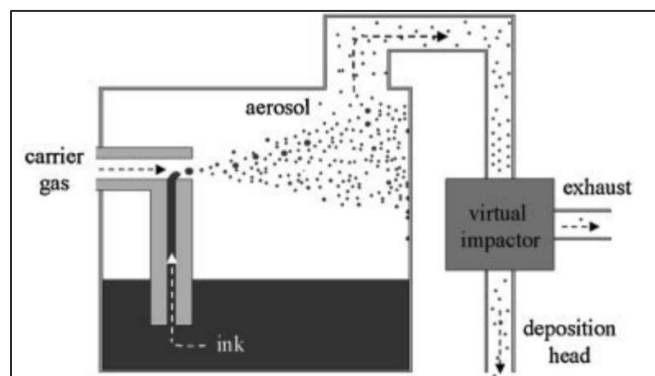


Figure 2.5: Schematic illustration of the pneumatic atomizer [23]

Pneumatic atomizer

According to Wilkinson et al. [31], the pneumatic atomizer is tolerant to inks with higher viscosity, ranging from 1 to 2500cp, and particle sizes up to 0.5 μm . In the pneumatic atomizer, a compressed carrier gas is expanded, resulting in a high-velocity gas stream. When this high-velocity gas stream passes over the ink supply channel, according to the Venturi principle, a region of reduced pressure is created which draws the ink from the reservoir to the atomizer nozzle. When the ink reaches the high-velocity gas stream, the top layer breaks down into

droplets suspended in the carrier gas. The aerosolized ink is then propelled onto the sidewall of the atomizer. According to Mette et al. [23], big droplets with high inertia will reach the sidewall and be extracted from the aerosol, while small droplets with low inertia stay in the carrier gas and are transported to the virtual impactor. The working principle of a pneumatic atomizer is schematically illustrated in Figure 2.5.

In the virtual impactor, a region of stagnant flow is used to separate droplets from the aerosol stream based on their inertia. Small droplets with low inertia are not able to pass the stagnant flow region and will be ejected, together with a large amount of carrier gas (major flow). Large droplets with high inertia are able to pass the stagnant flow region and are transported to the deposition head (minor flow). The working principle of a virtual impactor is schematically illustrated in Figure 2.6 [31].

2.2.3.2 Focusing and deposition

The focusing and deposition of the aerosolized ink is done by the printing head. The aerosol is guided into the nozzle where it is surrounded by a secondary gas flow. According to Saleh et al. [43], the secondary gas flow, also called sheath gas, prevents the aerosol from coming in direct contact with the nozzle. The sheath gas also focuses the aerosol stream onto the substrate, where the width of the printed lines will be a fraction of up to one-tenth of the actual nozzle diameter. According to Wilkinson et al. [31], the sheath gas also enables the AJP-technique to print consistent with a stand of distance ranging from 1 to 5mm, which makes it possible to print on uneven or slightly curved substrates. A schematic of the printing nozzle is illustrated in Figure 2.7.

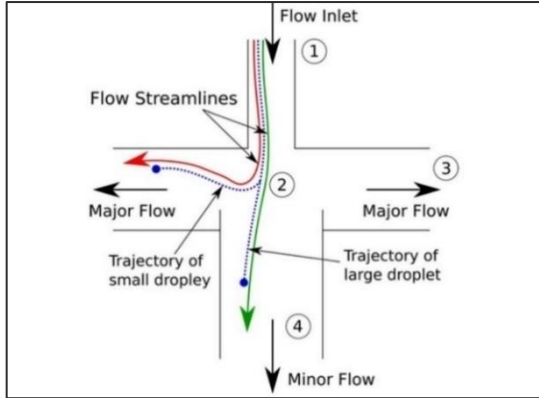


Figure 2.6: Schematic illustration of the virtual impactor [31]

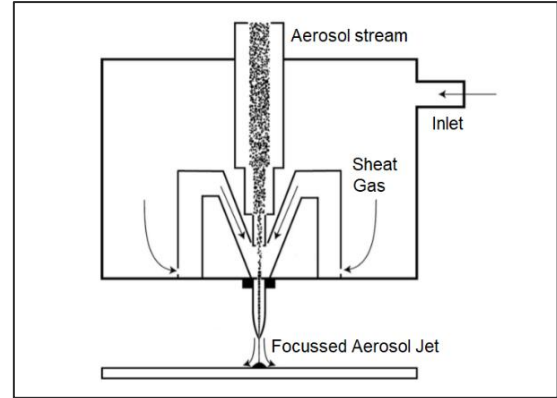


Figure 2.7: Schematic illustration of the deposition head with annular sheet gas [31]

According to Mahajan et al. [30], the aerosol surrounded by the sheath gas exits the nozzle with a velocity (V_e), density (ρ_e), and aerosol cross-section (A_e). If there is no loss in mass the following equation applies:

$$\rho_e \cdot A_e \cdot V_e = \rho_s \cdot A_s \cdot V_s \quad 2.1$$

where A_s is the cross-section of the printed line, V_s the print speed, and ρ_s the line density. By rearranging the previous equation, parameters that control the width (w) and thickness (t) of the printed line are given by:

$$w \cdot t \approx A_s = \left(\frac{\rho_e}{\rho_s} \right) \cdot \frac{V_e \cdot A_e}{V_s} \quad 2.2$$

2.2.4 Factors affecting deposition

This section explains the influence of some key printing parameters on the properties of the printed lines. Research groups have been investigating printing parameters [27], [30], [44], [45] to get a better understanding of the printing process. The parameters which influence the process and need to be controlled include the nozzle diameter, carrier gas flow, sheath gas flow, offset distance, temperature, and print speed. A review of the literature reveals that these parameters can be narrowed down to a few key parameters:

- Focusing ratio
- Nozzle size
- Carrier gas flow rate
- Print speed

Mahajan et al. [30] were the first to identify the focusing ratio as the ratio between the sheath gas flow rate and the carrier gas flow rate:

$$\text{Focusing ratio (FR)} = \frac{\text{Sheath gas flow rate}}{\text{Carrier gas flow rate}} \quad 2.3$$

Mahajan et al. [30] investigated the effect of the previously mentioned key printing parameters. Single-pass silver lines were printed using an AJP printer with three different nozzle sizes (100 μm , 150 μm , and 200 μm) and stage speeds ranging from 1 to 100mm/s. N₂-gas was used as carrier and sheath gas with flow rates ranging from 0-50 and 0-200 standard cubic centimeters per minute (sccm). The printed lines were sintered in an oven at 200°C. The result of their research is illustrated in Figure 2.8-Figure 2.11.

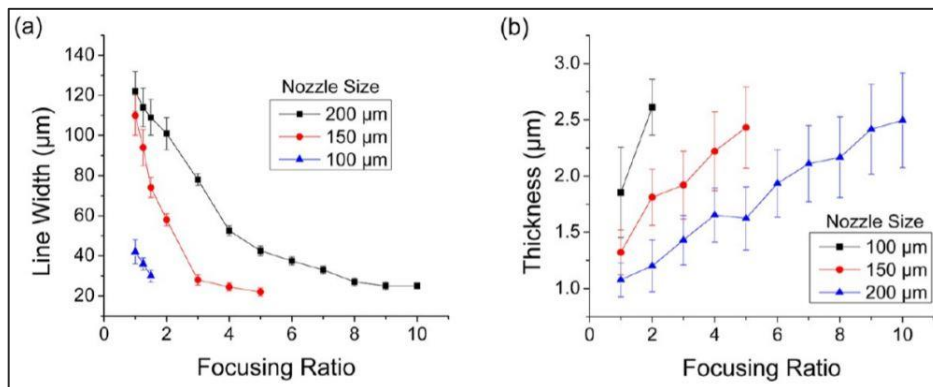


Figure 2.8: Effect of focusing ratio on (a) line width and (b) thickness for different nozzle sizes. [30]

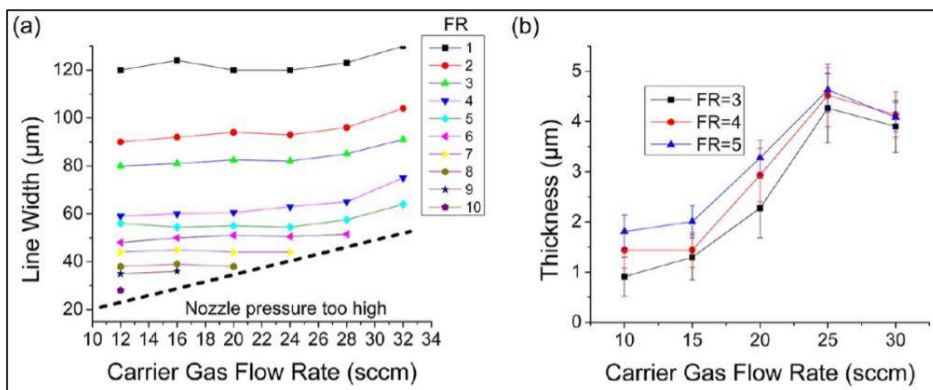


Figure 2.9: Effect of carrier gas flow on (a) line width and (b) thickness for different focusing ratios. [30]

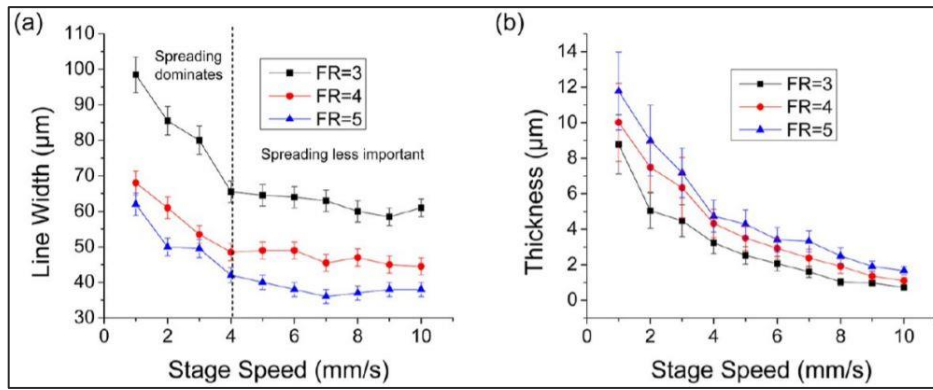


Figure 2.10: Effect of stage speed on (a) line width and (b) thickness for different focusing ratios.[30]

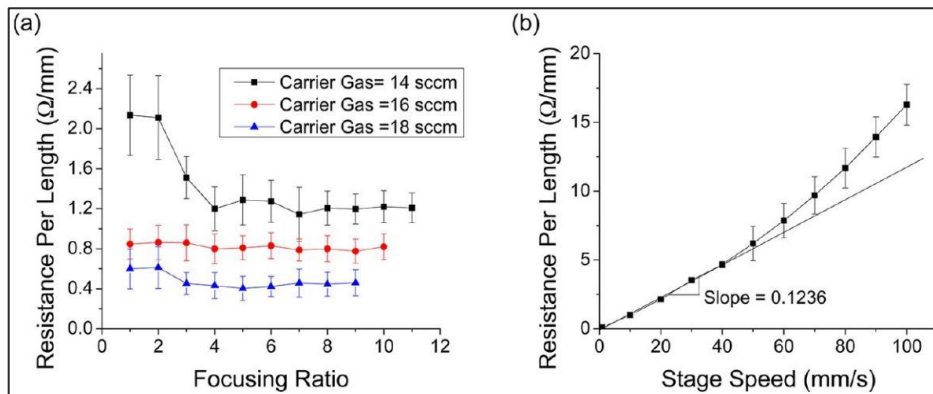


Figure 2.11: Effect of (a) focusing ratio and (b) stage speed on resistance per length. [30]

The following table gives a summary of the results obtained by Mahajan et al. [30] It lists the change in line width, line thickness, and electrical resistance with an increase of the corresponding process variable.

Table 2.7: Effect on line width, thickness, and resistance for independently increasing each of the process variables [31] (increase: ↑, decrease: ↓, no effect: -)

Process variable	Line width	Line thickness	Resistance
Focusing ratio (FR) ↑	↓	↑	-
Nozzle diameter ↑	↑	↓	-
Carrier gas flow rate ↑	-	↑	↓
Stage Speed ↑	↓	↓	↑

From this table, we can conduct that the line width increases with increasing nozzle diameter but decreases with increasing focusing ratio and stage speed. On the other hand, the line width is not influenced by the carrier gas flow rate. We also conduct that the line thickness increases with increasing focusing ratio and carrier gas flow rate but decreases with increasing nozzle diameter and stage speed. When looking at the table we can see that the electrical resistance is not influenced by the focusing ratio or nozzle diameter. On the other hand, the electrical resistance decreases with increased carrier gas flow rate and increases with increased stage speed.

2.2.4.1 Overspray

According to Chen et al. [46], overspray is one of the key problems when it comes to AJP. Not only does it result in a loss of material, but when not controlled, it makes it impossible to print quality lines close to each other. As seen in Figure 2.12, overspray is a region of unwanted deposited droplets that occurs around printed lines. According to Secor et al. [47], when depositing the aerosolized ink onto the substrate, small droplets with insufficient inertia are carried away from the deposition axis and form the overspray region. Larger droplets with sufficient inertia remain instead within the beam and impact the substrate along the deposition axis, to form the deposition pattern. In recent years, a lot of research has been conducted to get a better understanding of this phenomenon [46], [47]. This research shows that overspray can be minimized by decreasing the atomization flow rate and the stand-off distance. Verheecke et al. [45] also reported that excessive overspray occurs when the print head temperature and sheet gas flow rate are set too high. This increases the drying of the ink which leads to an increase in overspray.

Williams et al. [48] conducted experiments to assess the overspray compared to the printed area. This was done by introducing an overspray ratio (OR = overspray area/feature area). To evaluate the overspray, squares of different sizes were Aerosol Jet Printed onto a POEGMA substrate using Cy5-BSA ink. They report that the overspray is negligible for large feature sizes (>500 μm), but considerable for smaller feature sizes (<50 μm). At feature sizes below 50 μm , the overspray area is of the same order of magnitude as the print itself, which leads to a decreased accuracy. The overspray ratio for different feature sizes is illustrated in Figure 2.12.

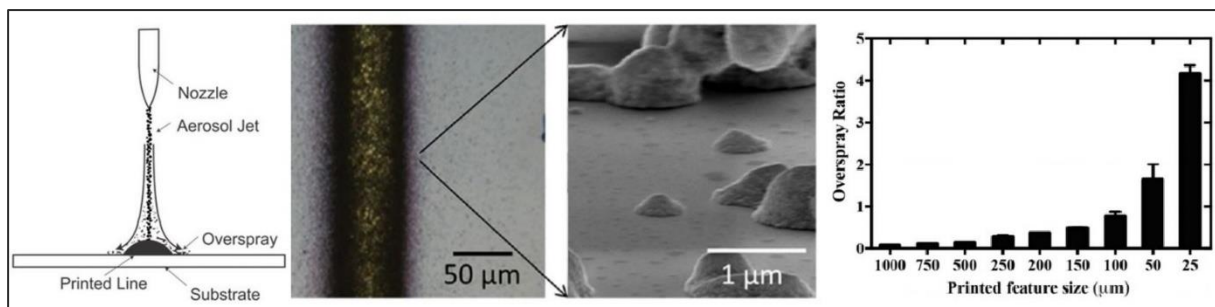


Figure 2.12: Overspray phenomenon, combination of [31] and [48]

2.2.5 Pre-and-post-printing treatments

2.2.5.1 Pre-printing treatments

Pre-printing treatment of the substrate surface is often required to increase printability. The printability of a surface can be improved by increasing its wettability (corona treatment) and by decreasing the surface roughness (polishing).

Corona treatment is a technique to increase the surface energy of the substrate, using a low-temperature corona plasma. According to Lynch et al. [49], the corona plasma is generated by a high voltage, high-frequency generator. The created energy will dissolve the stable O_2 molecules in the air into reactive O^- and O_3 molecules. The Reactive O^- molecules will react with the C molecules of the substrate's surface, resulting in the formation of polar oxygen groups at the surface of the substrate. This way, according to Hasan et al. [1], a hydrophilic surface is created which has increased wettability, as seen in Figure 2.13 where a line was printed on a hydrophilic and hydrophobic surface using silver ink [15]. The wettability of a

surface can be described with the wetting angle θ , as seen in Figure 2.14. Good wettability of the surface is obtained when the wetting angle ranges from 0-90°.

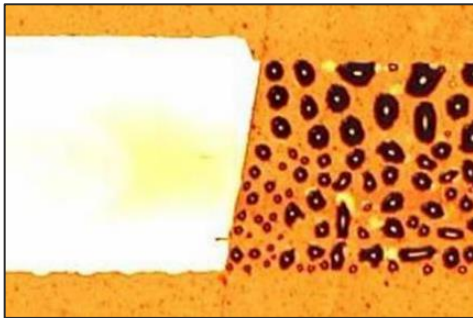


Figure 2.13: Ag line printed on a hydrophilic surface (left) and hydrophobic (right) surface [1]

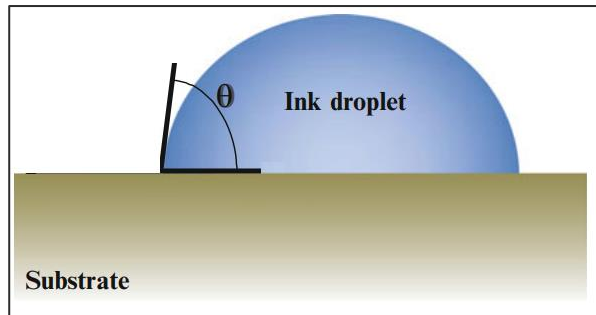


Figure 2.14: Wetting angle of a droplet on substrate [52]

Lynch et al. [49] reported that the corona treatment of the surface is limited by reactions such as polymeric chain scission and ablation of the surface. Virgilio et al. [50] conducted experiments on a PDMS substrate to see how the input voltage and exposure time influence the wetting angle. In their case, an input voltage of 4.5kV and exposure time of 200s gave the optimal result.

Polishing of the substrate can be done to decrease the surface roughness. Ihalainen et al. [51] conducted experiments where Ag-lines were printed on substrates with low (PET) and higher roughness (paper). They experienced that higher printing resolution and lower edge waviness were achieved with smooth and non-porous substrates. They also found a linear increase in resistance with the surface roughness.

In previous work, conducted by Eng. A. Verma at the advanced manufacturing laboratory of KU Leuven Campus De Nayer, silver ink (Metalon[®] JS A221E) was used to print lines onto a 3D-printed polyamide (PA) substrate. Because it was 3D-printed, the substrate has a rather high surface roughness ($R_a=6\mu\text{m}$, $R_z=31\mu\text{m}$). This high surface roughness resulted in poor printing of the silver lines. A solution was found in the polishing of the substrate with approximately 600 and 2400 grit paper. By decreasing the grit size step-by-step, the roughness of the surface decreased until the desired value was reached.

2.2.5.2 Post-printing treatments

After deposition of the ink, the metal nanoparticles are usually coated with organic materials. These organic coatings are a remain of the stabilizing agent used to disperse the nanoparticles into the ink but prevent the transfer of electrons between the metal nanoparticles. According to Roshanghias et al. [52], the printed lines thus have a large resistivity and require post-processing. The sintering process will evaporate any leftover solvent and make the nanoparticles lose their organic coating, resulting in direct contact between the nanoparticles. On the other hand, sintering will also heat the nanoparticles to a temperature, below the melting point, where the atoms of the particles will be diffused over the particle boundaries, fusing them together. This results in improved electrical conductivity and adhesion from the pattern to the substrate. The sintering process is schematically illustrated in Figure 2.15. Scheutz et al. [53] reported that due to the nano-scale particle sizes, the temperature required for the sintering

process is much lower than the bulk-material melting temperature. The sintering temperature for silver inks is typically in the range of 200°C.

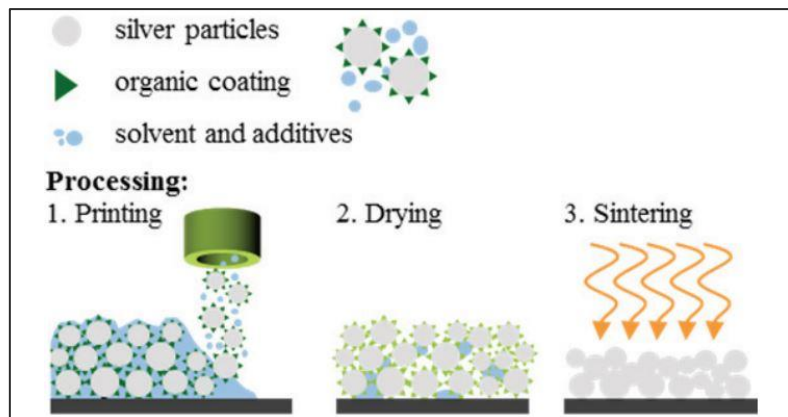


Figure 2.15: Schematic illustration of the sintering process [52]

Sintering is conventionally done by heating the deposited ink. At the same time, however, the substrate is also exposed to this heat. Because the substrate is usually made from flexible polymers such as PET, extreme heating of the substrate must be avoided. This led to the development of different sintering techniques, which can be implemented according to the substrate and desired characteristics of the printed pattern. Some of the most conventionally used sintering techniques are discussed in what follows:

Ohmic sintering is a technique where a voltage is applied to the conductive printed paths. This results in a current flowing through the paths, which have a certain resistance. According to the Joule effect, the resistance of the paths will dissipate the electrical energy and transform it into heat which leads to sintering. According to Kamyshny et al. [32], this method reduces substrate heating since the heat is only concentrated in the conducting paths. In order to work, ohmic printing requires sufficient conductivity of the printed paths. This can be obtained with a pre-treatment step such as thermal pre-heating or IPL pre-sintering, which typically brings the conductivity to 0.15% of the bulk material [52]. According to Roshanghias et al. [52], the conductivity of the printed paths increases with increasing input current. A major disadvantage of ohmic sintering is that when a certain conductivity is reached, insufficient heat is generated to sinter the surrounding of the pre-sintered path. On the other hand, this enables ohmic sintering to be a very selective process, by rinsing away the non-sintered material from the substrate. This results in an increased resolution of the printed tracks [52].

Laser sintering is a technique where a laser is used to induce heat into the printed lines. The laser spot is usually smaller than the linewidth, which means multiple passes are required to sinter the complete pattern. Niittynen et al. [54] reported that when a substrate is used which is transparent to the laser wavelength, direct exposure of the laser to the substrate will not cause heating or deforming of the substrate. However, the substrate will experience indirect exposure to heat, caused by the radiation conducted through the ink. The process temperature, which depends on the laser power and scanning speed, can locally exceed the glass transition temperature. Roshanghias et al. [52] reported that when the scanning speed is kept constant the affected area by laser sintering expands with increasing optical power. This results in an increased conductivity of the tracks when the laser power is increased. Zenou et al. [55] reported that selective laser sintering technology can be used to sinter the central

parts of the printed pattern. Afterward, the non-sintered parts can be easily removed by rinsing with an adequate solvent. This results in a high-resolution pattern that is only limited by the properties of the optical laser system.

Intense pulsed light sintering (IPL) is a sintering technique where intense short pulses of light are used to increase the temperature of the printed ink locally and rapidly. The light source used for this technique is typically a xenon lamp which emits at wavelengths ranging between UV and IR. According to Niittynen et al. [54], when silver nanoparticle ink is used in combination with a transparent substrate, the emitted light is only absorbed by the ink. This results in a rapid temperature rise of the ink while the substrate remains unaffected. However, the substrate will experience indirect exposure to heat, caused by the radiation conducted through the ink. A disadvantage of IPL is that it is only suited for 2D or mildly curved substrates. As the distance between the light source and substrate increases, the intensity of the light decreases. On a curved substrate, this results in over-sintered and under-sintered parts of the pattern [52]. Sheuts et al. [53] conducted experiments on a 5-axis IPL-machine to investigate the influence of change in z-direction. They reported that the substrates can be moved up to 5mm outside the focus point of the light beam without significant changes to the resistance of the pattern. Roshanghias et al. [52] reported that an increase in energy density of the light pulses significantly increases the conductivity of the printed patterns.

Thermal sintering is a technique where heat is applied to the printed pattern by means of a convection oven. This is the most commonly used technique because of its simple nature. Disadvantages of thermal sintering are a long processing time ranging from 30-200min and the restrictions for temperature-sensitive substrates. According to Roshanghias et al. [52], the high conductivity obtained by this process compared to alternative processes, as discussed earlier, is worth the long processing time. They also report that thermal sintering results in a uniform structure which is due to the fact that diffusion of atoms relies heavily on the sintering temperature and time. The high diffusion rate combined with the grain growth results in a dense and homogenous microstructure that has a high conductivity [52].

2.2.6 Applications

This section contains some state of the art applications which can be produced using the Aerosol Jet Printing process. Although AJP is a rather new technique, it is widely used for industrial applications due to the advantages mentioned in section 2.2.1. Some of the most common applications are thin-film transistors (TFT's) [9], organic light-emitting diodes (OLED) [11], and photovoltaic cells [10]. These applications are discussed more in detail:

Thin film transistors (TFT's) are usually produced using lithography techniques. The desire for a low-cost and flexible technique has led to the development and use of the AJP-printing technique to produce TFT's. Lu et al. [9] used this technique successfully to print TFT's consisting of four different layers as shown in Figure 2.16. In the first step, the channel region is printed using carbon nanotube (CNT) ink which is rinsed with toluene. Next, the source and drain electrodes are printed using AgNW (silver nanowire) ink. Then a dielectric h-BN layer is printed on top of the channel region and de gate and source electrodes. Finally, the gate electrode is printed on top of the dielectric layer using the same AgNW ink as used for the source and drain electrode.

Organic light-emitting diodes (OLED) are widely used over conventional LED's because they offer benefits like a wider viewing angle and low-temperature producibility on large substrates. AJP-printing enables a high-speed deposition of the patterned materials, resulting in a mechanically robust and lightweight emission display. Tait et al. [11] used this technique to create OLED's as a stack of luminescing and carrier transporting materials, as shown in Figure 2.17. First, the anode was created by depositing a transparent indium tin oxide (ITO) layer onto the substrate. Next, an edge cover layer (ECL) is deposited to define the emitting area, which is covered with a hole injection layer (HIL). Then, an emissive layer (EL) is added and covered with an electron transport layer (ETL), topped with a cathode layer. In high-resolution displays, the pixel density can be increased by decreasing the opening between the ECL layer [11].

Organic solar cells are an interesting technique to convert solar energy into electricity. The use of AJP to produce solar cells has the advantage that they are more lightweight and flexible than conventionally used silicon solar cells. Kopola et al. [10] used the AJP technique to produce organic solar cells illustrated in Figure 2.18. First, the Al/Cr/Al layer was deposited by a shadow mask. Next the photoactive layer (P3HT:PCBM) and light-absorbing layer (PEDOT:PSS) were spin-coated. Finally, a grid of fine Ag lines was printed using the AJP technique [10].

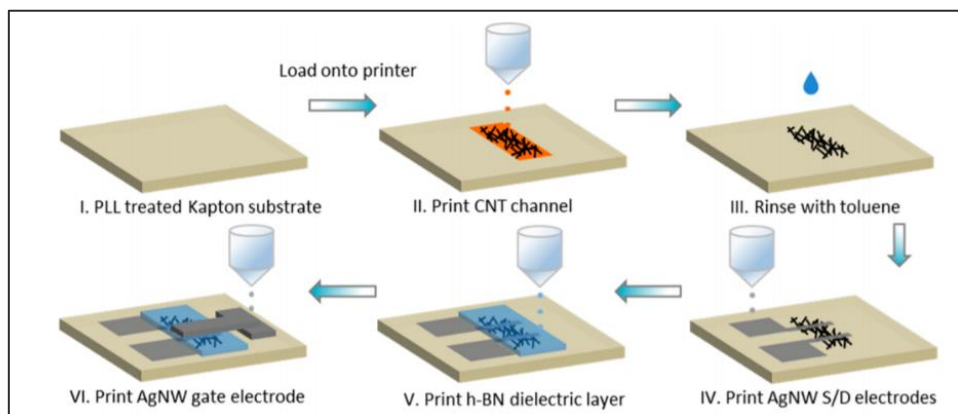


Figure 2.16: Schematic production process of TFT using AJP [9]

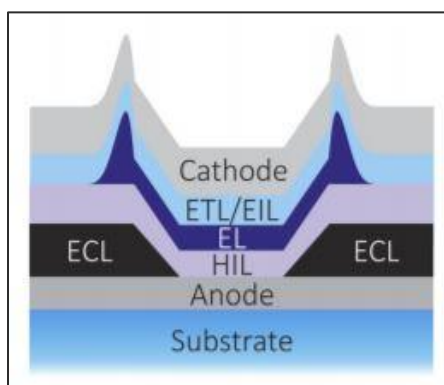


Figure 2.17: Schematic illustration of the OLED [11]

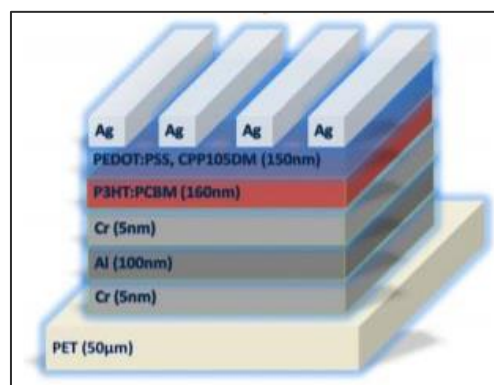


Figure 2.18: Schematic illustration of the solar cell structure [10]

2.3 Piezoresistive sensors

This chapter contains the state of the art information about printed piezoresistive-based pressure sensors. In the experimental part of this thesis, printed piezoresistive pressure sensors are tested and implemented on freeform substrates. An overview of these aspects is key to deeply understand the characteristics of the sensor. First, an introduction to printed sensors is given with respect to the advantages and applications. Next, the working principle of the piezoresistive material is described and the sensor configuration is explained. Finally, a description of key sensor parameters is given along with the experimental conditions to analyze them.

2.3.1 Introduction

Nowadays, according to Khan et al. [2], the need for flexible, large-area pressure sensors is increasing, with applications in the biomedical, automotive, and aerospace industry. According to Narakathu et al. [56], conventionally made silicon pressure sensors are often expensive, produced on a rigid substrate, and lack the properties required for various sensing applications. To overcome these problems, sensors can be printed on flexible substrates which are thin, lightweight, flexible, and cost-efficient. Polzinger et al. [57] reported that multiple printing techniques can be used to produce pressure sensors. They also report that screen printing is the most common technique, but that direct printing techniques as inkjet printing and AJP are gaining more importance. In the field of printed electronics, the three major pressure sensor types are piezoresistive-based, capacitive-based, and piezoelectric-based sensors, which all have different working principles.

Polzinger et al. [57] were able to produce capacitive pressure sensors, based on printed differential interdigital capacitors (IDC). Silver ink from Sun Chemical Corporation was inkjet-printed onto an injection molded polybutylene terephthalate (PBT) substrate, and sintered for 1h at 200°C. The sensitive polymer layer was deposited through AJP. When compressing this sensor type, a change in capacitance is a measure for the applied pressure.

Rajala et al. [58] were able to produce piezoelectric pressure sensors on a flexible PET substrate. First, a 100nm thick layer of silver ink was screen printed to provide the bottom electrode. The active PVDF-TrFE layer was screen printed on top of the silver electrode, which was then sintered at 120°C for 3h. Finally, the top electrode was made by applying silver paint using a brush. When this sensor type is compressed, the active layer generates a charge which is a measure for the applied pressure.

Ramalingame et al. [59] were able to produce a piezoresistive sensor matrix, which is based on multi-walled carbon nanotubes dispersed in a polymer matrix. Silver electrodes were screen printed onto a flexible Kapton sheet and sintered in an oven at 150°C for 2h. The functional layer, PDMS Sylgard 184, was then cast and cured at 120°C for 4h to create a self-sticking layer that is put on top of the silver electrodes. When this sensor type is compressed, the resistance of the active layer decreases which is a measure for the applied pressure.

Kappassov et al. [60] reported that piezoresistive pressure sensors are less sensitive to electromagnetic interference and have less complex data acquisition systems than those of capacitive pressure sensors, which was also confirmed by Adjami et al. [61]. In this study, we will investigate the characteristics of piezoresistive-based sensors more in detail.

2.3.2 Working principle of piezoresistive material

Piezoresistive sensors convert an applied pressure, as a result of a force, into a change of impedance. According to this change of impedance, one can determine the applied pressure by means of a readout circuit. Piezoresistive materials are used to provide a change in resistance when a force is applied. According to Valle-Lopera et al. [8], the relationship between the applied force (F) and the resistance of the material can be described by:

$$R = \frac{\rho \cdot K}{F} \quad 2.4$$

Where ρ is the resistivity and K is a function of the surface roughness and elastic properties of the material. As seen in the previous equation, the resistance of the piezoresistive material is inversely proportional to the applied force. The electrical resistance will be in the range of mega ohms when no force is applied and decrease to kilo ohms when the applied force increases [8]. The piezoresistive layer is typically a conductive polymer, which is made by dispersing conductive nanoparticles into a non-conductive polymer matrix. According to Ramalingame et al. [59], polydimethylsiloxane (PDMS) is widely used as background for the piezoresistive layer, because of its flexibility, biocompatibility, and temperature stability. However, Kappassov et al. [60] reported that the use of elastic materials results in hysteresis in the piezoresistive layer and a decrease in sensitivity due to wear. They also report that the characteristics of the material can change according to temperature and moistness and that there is low repeatability after multiple deformations. According to Ramalingame et al. [59], the piezoresistive properties of the composite are dependent on the choice of nanoparticles used in the polymer matrix. Carbon nanotubes (CNT's) are widely used as nano-fillers, with a concentration ranging from 1wt% to 8wt% and a pressure limit ranging from 5 kPa to 200kPa.

Wang et al. [62] developed a pressure sensor where carbon black dispersed in a silicone rubber is used as a piezoresistive layer. Figure 2.19a shows the structure of this carbon black/silicone rubber nanocomposite, where phase A is a rubber molecule chain, phase B is crosslinking between the rubber chains, phase C is a macro-rubber which is absorbed by the carbon black surface, and phase D is the carbon black nanoparticle. Phases C and D act as a framework, which is connected by elastic phases A and B which form the background of the material. When pressure is applied to the material, the gap between the carbon black particles decreases, resulting in the formation of local conductive paths. As showed in Figure 2.19b, an effective conductive path is formed where the local conductive path penetrates the outer insulating layer.

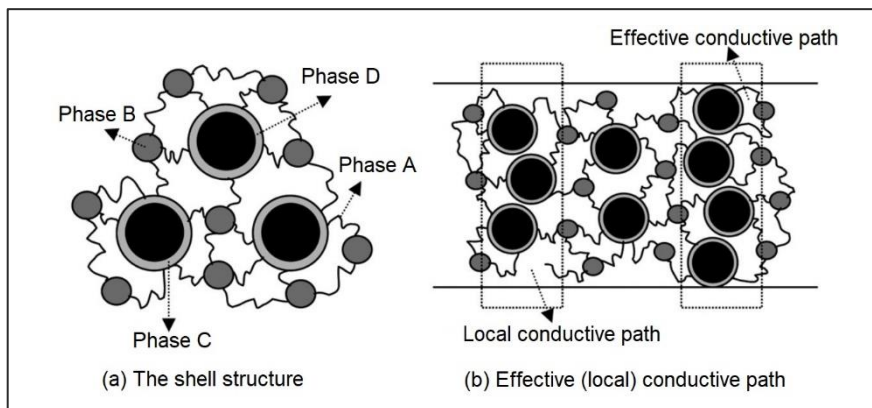


Figure 2.19: Schematic diagram for the shell structure (a) and the effective (local) conductive path (b) of a nanocomposite [62]

The conductive path is a result of the so-called, tunneling effect. This is the crossing of electrons between closely spaced nanomaterials, through the non-conductive barrier between them. According to Zhang et al. [63], the total resistance in a conductive polymer is determined by the combined resistance of the conductive particles and the polymer matrix. They report that the resistance of the paths perpendicular to the current flow can be neglected when assuming that the resistivity of the matrix is constant in the entire composite. This results in a relationship where the number of conductive particles between the electrodes, and the number of conductive paths influence the resistance, as seen in the following equation:

$$R_0 = \frac{(L - 1)R_m + LR_c}{S} \approx \frac{L(R_m + R_c)}{S} \quad 2.5$$

where R_0 is the conductive polymer resistance, R_m the resistance between two neighboring filler particles, R_c the resistance across a conductive filler particle, L the number of particles forming the conductive path, and S the number of effective conductive paths. When the distance between the conductive filler particles is very large, no current flows through the particle gap. When the distance between the conductive particles decreases, a tunneling current flows from one particle to another through the polymer separation. According to Kalantri et al. [64], the tunneling current (J) at an applied voltage (V) can be expressed by the following equation:

$$J = \frac{3\sqrt{2m\phi}}{2s} \cdot \left(\frac{e}{h}\right)^2 \cdot V \cdot \exp\left(-\frac{4\pi s}{h}\sqrt{2m\phi}\right) \quad 2.6$$

where m and e are electron mass and charge respectively, ϕ is a constant for the energy barrier of the polymer between two neighboring filler particles, h is Plank's constant, and s is the distance between the nanoparticles.

Zhang et al. [63] reported a proportional relationship between the tunneling resistivity (R_m) and the contact area (a^2) between two conductive filler particles. This leads to the following equation:

$$R_m = \frac{V}{a^2 J} \quad 2.7$$

Combining equation 2.3 and 2.4 results in:

$$R_m = \frac{8\pi h s}{3a^2 \gamma e^2} \exp(\gamma s) \quad 2.8$$

where:

$$\gamma = \frac{4\pi}{h}\sqrt{2m\phi} \quad 2.9$$

The conductivity of the conductive filler particles is very high, compared to the conductivity of the polymer matrix, and can thus be neglected ($R \sim 0$). Taking this into account and substituting equation 2.8 in equation 2.5 gives:

$$R_0 = \frac{L}{S} \left[\frac{8\pi h s}{3a^2 \gamma e^2} \exp(\gamma s) \right] \quad 2.10$$

Kumar et al. [65] reported that when a piezoresistive material is subjected to stress, the resistance changes due to the change in particle separation. This is caused by the difference in compressibility between the conductive filler particles and the polymer matrix. Assuming that

the distance between the particles decreases from s_0 to s when pressure is applied, the relative resistance (R/R_0) can be calculated by:

$$\frac{R}{R_0} = \frac{s}{s_0} \exp[-\gamma(s_0 - s)] \quad 2.11$$

where R_0 is the initial resistance of the composite and s_0 the initial distance between the conductive nanoparticles. The deformation of the conductive filler particles is in the range of a few nanometers and can be neglected compared to the deformation of the matrix. The distance between neighboring particles can thus be expressed as:

$$s = s_0(1 - \varepsilon) = s_0 \left(1 - \frac{\sigma}{E}\right) \quad 2.12$$

where ε is the strain of the polymer matrix. Wu et al. [66] reported that the initial distance between filler particles, which are spherical and arranged in a cubic lattice, can be determined by:

$$s_0 = D \left[\left(\frac{\pi}{6\vartheta}\right)^{1/3} - 1 \right] \quad 2.13$$

where D is the conductive filler particle diameter and ϑ the volume fraction of the filler in the composite matrix. Substituting equation 2.12 and 2.13 in 2.11 results in:

$$\frac{R}{R_0} = \left(1 - \frac{\sigma}{E}\right) \exp \left\{ -\gamma D \left[\left(\frac{\pi}{6\vartheta}\right)^{1/3} - 1 \right] \frac{\sigma}{E} \right\} \quad 2.14$$

$$\frac{R}{R_0} = f(\sigma, E, D, \vartheta, \varphi) \quad 2.15$$

Looking at equation 2.15, we can conclude that the most important parameters affecting the relative resistance are: applied stress (σ), the elasticity modulus of the polymer matrix (E), the conductive filler diameter (D), the filler volume fraction (ϑ), and the constant for the energy barrier of the polymer (φ).

2.3.3 Piezoresistive sensor configurations

In this section, a general view of the sensor configuration is explained, along with some advantages and disadvantages of different configurations.

A piezoresistive pressure sensor typically consists of an insulating layer, an electrode layer, and a piezoresistive layer. The electrode layer can be printed onto the substrate by means of screen printing [67] or AJP [68] techniques, and typically consists of silver ink. The substrate can be rigid or flexible, dependent on the sensor application. According to Ramalingame et al. [59] and Ahmad et al. [67], the objective of the electrode layer is to give a physical readout point for the change in resistance of the piezoresistive layer. According to Valle-Lopera et al. [8], the piezoresistive layer is either screen printed between two electrodes (Figure 2.20a), or on top of a planar finger-like structure of two electrodes (Figure 2.20b). They also report that the finger-like structure increases the sensitive contact area [8]. According to Yaniger et al. [69], the width of the finger electrodes is typically in the order of 0.4mm. At last, an insulating layer is added which spreads the applied force over a wider area and isolates the sensor from external conductors or voltages which reduces interference. According to Ramalingame et al.

[59], PDMS is widely used as an insulating layer because of its high stability, flexibility, and biocompatibility. Khan et al. [70] conducted microscopic tests on a screen-printed MWCNT/PDMS piezoresistive layer, using a scanning electron microscope (SEM). The samples were sintered in a vacuum at a temperature of 80°C for 5 hours. They observed a porous structure with pinholes, which indicates complete evaporation of the solvent. They also report that when a silver electrode is printed on top of the MWCNT/PDMS-layer (as in the sandwich sensor structure of Figure 2.20a), the conductive ink penetrates the pinholes, resulting in short-circuiting of the sensor. This is something to keep in mind when choosing the sensor configuration.

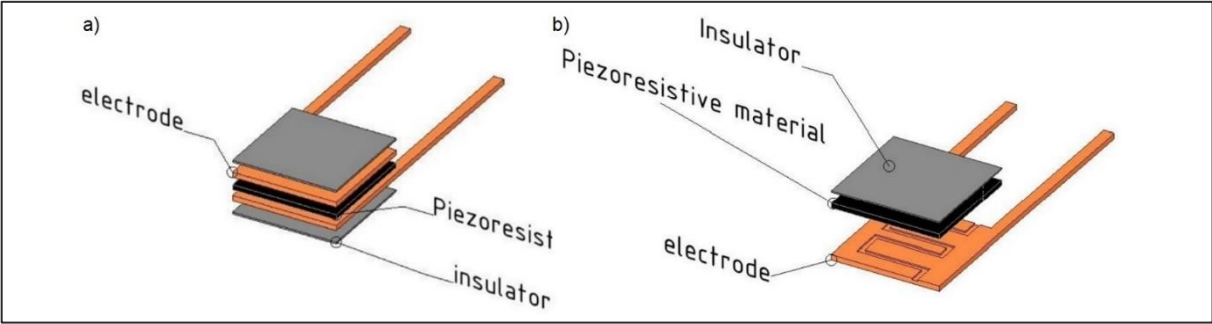


Figure 2.20: Sandwich sensor structure (a) planar finger sensor structure (b) [59]

According to Woo et al. [7], the electric properties of the piezoresistive layer can be strongly enhanced by an increase in the number of print passes. They conducted tests where CPDMS ink was used to print the piezoresistive layer, which consists of 10wt% CNT’s dispersed in a PDMS matrix. They report an exponential decrease in electrical resistance when the number of print passes is increased. Kappasov et al. [60] confirm this theory by reporting that the resistance of the piezoresistive layer does not only depend on the deformation, but also on the total thickness of the layer.

2.3.4 Typical sensor characteristics

The performance of a sensor can be described by multiple parameters. Key sensor parameters such as hysteresis, sensitivity, repeatability, and temperature and humidity drift are discussed in Table 2.8.

Table 2.8: Key sensor parameters

Key sensor parameter	Discussion
Hysteresis [59] [71] [8]	<ul style="list-style-type: none"> This is the difference in output value between increasing and decreasing force. Caused by the viscoelasticity of the piezoresistive ink and substrate. Optimal: as low as possible. (expressed as %)
Sensitivity [59]	<ul style="list-style-type: none"> The sensor's sensitivity is a measure for the change of output value in function of a change of input. In the case of a piezoresistive sensor, the input value is a force and the output value is a change in resistance. (Expressed as ΩPa^{-1})

Repeatability [59] [67] [72]	<ul style="list-style-type: none"> This is the capability of the sensor to produce an equal response each time the same input is applied. Optimal: As high as possible.
Stability [59] [67] [8][72]	<ul style="list-style-type: none"> This is the capability of the sensor to produce a constant output value when a constant force is applied over a period of time. Change in stability is called drift of the sensor. Optimal: stability as high as possible, drift as low as possible.
Temperature & humidity range [67][73]	<ul style="list-style-type: none"> When the environmental conditions (temperature and relative humidity) change, the characteristics of the sensor will be altered. An operating range can be determined in which the sensor shows acceptable variation in output.

2.3.4.1 Hysteresis

Hysteresis is the difference in output value between increasing and decreasing load. Ramalingame et al. [59] produced a piezoresistive sensor on a flexible Kapton sheet. The sensor was composed of printed silver lines, and the active piezoresistive layer was synthesized by dispersing MWCNT's into a PDMS matrix. Hysteresis of the sensor was determined by a readout of the resistance while increasing the pressure from the starting value to 640kPa followed by a decrease to the starting value. They report that there is a notable difference between the loading and unloading curve which is caused by the viscoelastic effect of the PDMS layer. They also report that the hysteresis effect reduces with increased applied pressure from 60% at 100kPa to 0.8% at 640kPa, as illustrated in Figure 2.21. Similar results were reported by Valle-Lopera et al. [8]. They plotted the output value of four different sensors (S1: Velostat, S2: EX-STATIC fabric, S3: home build sensor, S4: thruMode MatrixTM) for increasing and decreasing load, as seen in Figure 2.22.

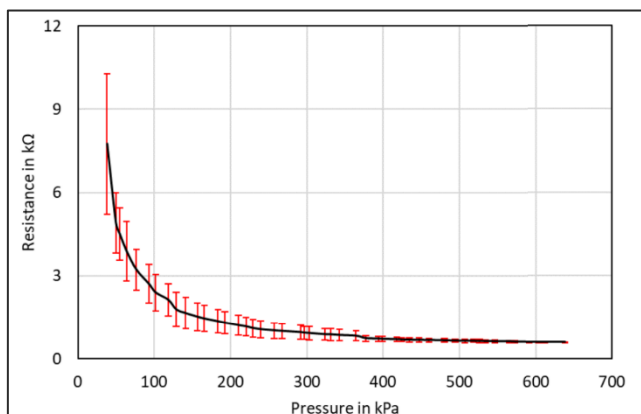


Figure 2.21: Sensor hysteresis Ramalingame et al. [59]

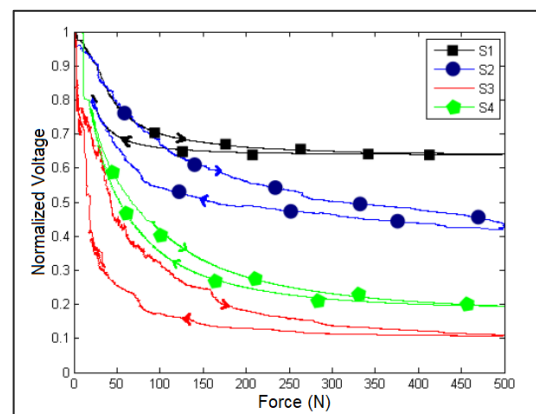


Figure 2.22: Sensor hysteresis Valle-Lopera et al. [8]

2.3.4.2 Sensitivity

The sensitivity of a sensor is a measure for the change in output value in function of a change in input. In the case of a piezoresistive pressure sensor, the input value is the applied pressure and the output value is the change in resistance. According to Ramalingame et al. [59], the sensitivity of a piezoresistive sensor differs for different load regions as shown in Figure 2.23. During the load-cycle, the sensitivity varies from $4.3 \text{ k}\Omega \text{ kPa}^{-1}$ to $3.5 \text{ }\Omega \text{ kPa}^{-1}$. During the

unloading cycle, the sensitivity varies from $1.2 \Omega \text{ kPa}^{-1}$ to $7.8 \text{ k}\Omega \text{ kPa}^{-1}$. They report that the different sensitivity regions are caused by the compressibility of the material and the concentration of nano-fillers in the composite layer. When pressure is applied, the composite layer gets compressed fast at first, resulting in high sensitivity. When a certain threshold is reached, further compression of the composite layer decreases while the applied pressure is increased, resulting in a decrease in sensitivity.

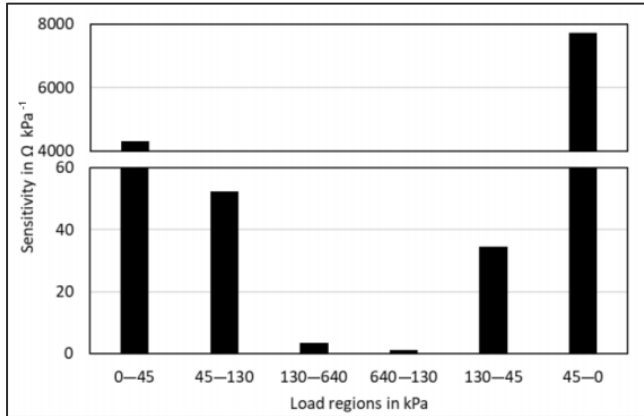


Figure 2.23: Sensitivity of a piezoresistive sensor [59]

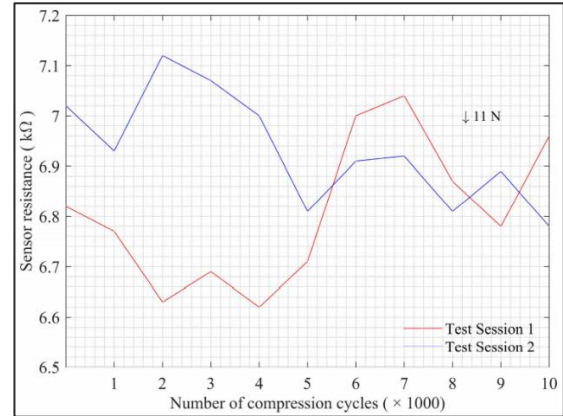


Figure 2.24: Cyclic test of a piezoresistive sensor [67]

2.3.4.3 Repeatability

The repeatability of a sensor is its capability to produce an equal response each time the same input is applied. Ahmad et al [67] conducted repeatability tests on a home build piezoresistive pressure sensor. The pressure sensor was made by screen printing conductive electrodes and a pressure sensing layer onto a PET substrate. For the repeatability test, the sensor was subjected to two sessions of ten thousand actuations, using a force of 11N, while monitoring the resistance after each actuation. They reported a maximum deviation of 8% in the sensor resistance as seen in Figure 2.24, although the characteristics of the sensor were maintained. Cyclic repeatability tests were also performed by Ramalingame et al [59]. They subjected their pressure sensor to twenty compression cycles at a rate of 2Ns^{-1} with a maximum force of 50N. The nano-fillers in the polymer matrix are randomly distributed and when cured, the polymer matrix prevents re-agglomeration of the nano-fillers. They report that when the composite is subjected to a cyclic load, relaxation of the composite occurs, resulting in better stability of the polymer matrix. This so-called ‘mechanical training’ results in improved stability and repeatability of the sensor, while reducing the hysteresis.

2.3.4.4 Stability

The stability of a sensor is its capability to produce a constant output value when constant pressure is applied over a period of time. The stability of the sensor output value can be investigated by applying a constant force to the sensor and monitoring the resistance over a period of time. Ahmed et al. [67] conducted time drift testing, where constant loads ranging from 2-25N were applied to the sensor over a time of 24 hours. To reach a steady-state, the sensors were first given 20 seconds of initializing time. As seen in Figure 2.25, the sensor resistance evolves to a near-constant value in the first hour. This is due to the electrical drift in the piezo resistors. Ramalingame et al. [59] and Valle-Lopera et al. [8] also conducted time drift experiments that showed similar results.

2.3.4.5 Temperature and humidity operating range

The sensor's behavior differs according to the temperature and humidity. The operating range of the sensor corresponds to the range in temperature and humidity which causes acceptable variation. The influence of temperature and humidity on the sensor's characteristics can be investigated by applying a variation in temperature and humidity to the sensor while monitoring the resistance. Ahmed et al. [67] conducted tests where their piezoresistive sensor was put into an environmental chamber where the temperature was varied at constant humidity. They report a higher variation in colder to hotter tests, while in the hotter to colder tests there is less variation at first but a higher sudden increase of resistance, as shown in Figure 2.26.

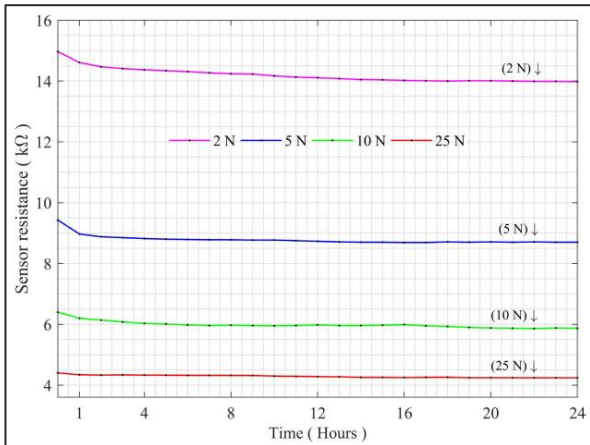


Figure 2.25: Time drift testing at constant load [67]

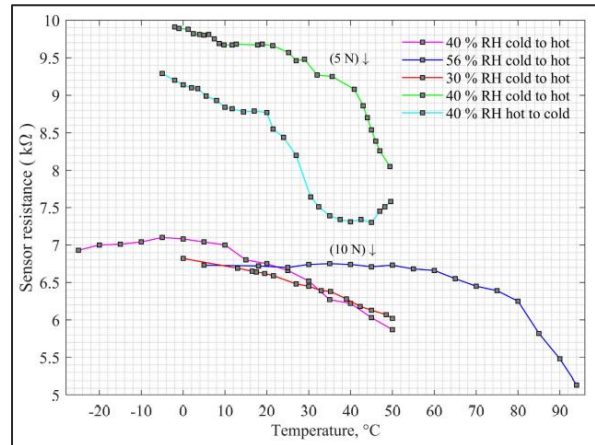


Figure 2.26: Temperature and humidity drift testing [67]

2.4 Freeform printing

Aerosol Jet printing can be used to produce printed electronic components and circuits on planar and freeform substrates. This is an important part of this thesis since piezoresistive pressure sensors are produced on freeform substrates using a combination of AJP and screen printing techniques. According to Paulsen et al. [74], applications with dimensions ranging from millimeters to centimeters include antennas onto substrates like body armor for military personnel and aircraft fuselages. This is possible because of the relatively high standoff distance (1 to 5mm) between the nozzle and substrate, and the long focal length of the aerosol beam. According to Bruce King et al. [5] this allows to print over trenches as illustrated in Figure 2.27, where silver lines were printed over a 500µm trench using Aerosol Jet® printing.

A traditional approach to produce electric circuits onto a curved substrate is to first produce the circuit onto a flexible substrate, and then glue it to the desired curved substrate. With AJP, direct printing of the circuit onto the curved substrate can be achieved [5]. When moving beyond printing on substrates with micro-scale height differences, AJP can use 3 to 5 motion axes to create complex circuits onto freeform substrates. Neotech has developed 5-axis AJ®P systems to enable the production on freeform substrates [6]. Figure 2.28 shows an antenna printed directly onto a curved substrate. Paulsen et al. [74] reported that the antenna is produced by translating the deposition head in the xyz-direction, while the orientation of the printhead was kept normal to the build plate. They report that no rotation of the printhead was

required as the AJP printing process can print on surfaces that are tilted by up to 45 degrees relative to the axis of deposition.

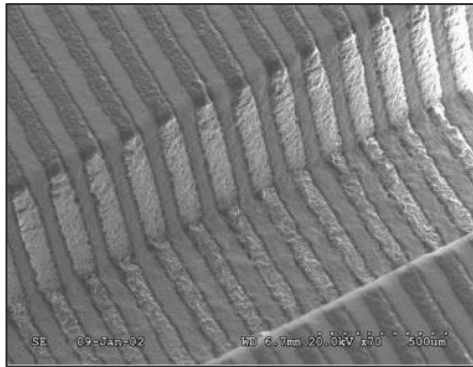


Figure 2.27: Silver lines printed over a 500µm trench [5]

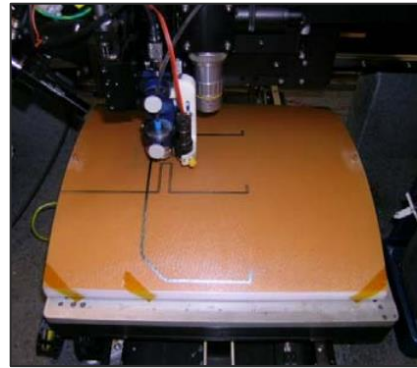


Figure 2.28: Antenna printed on curved substrate [6]

Blumenthal et al. [38] produced a heating element onto the leading edge of a rotor blade using the AJP technique. The deposition nozzle remained fixed while the substrate was attached to a motion-controlled build plate. The printing paths were designed as a 2D projection onto the 3D substrate. To print the entire circuit onto the leading edge, the pattern was separated into three different prints, which required re-orientation of the substrate in between. This is illustrated in Figure 2.29.

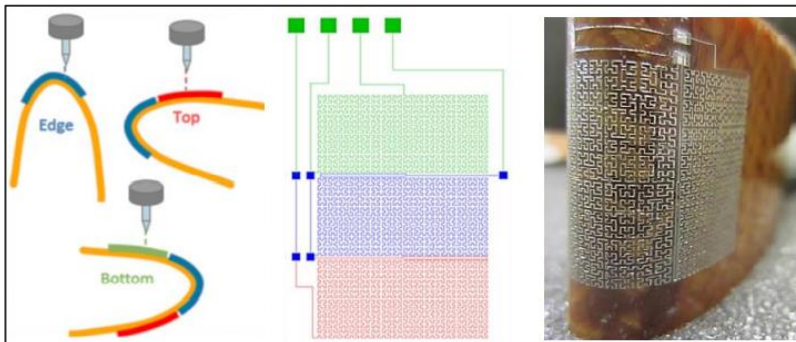


Figure 2.29: Serial printing patterns for the production of a heating element. Adjusted from [38]



Figure 2.30: 5-axis printing on ping pong ball [75]

In previous work, conducted by Deprince et al. [75] at the advanced manufacturing laboratory of KU Leuven Campus De Nayer. 5-axis printing onto a ping pong ball was done using a home build aerosol jet-based printer (NEBULA 5X-100s), as seen in Figure 2.30. The printing pattern was designed using Creo parametric, which was then converted to an NGC-file, using the own build postprocessor. The NGC-file was then uploaded onto the Linux CNC software which operates the machine.

2.5 Conclusion of the state of the art

Printing techniques can be divided into direct and indirect techniques. Direct printing techniques are limited to two-dimensional deposition, while indirect printing techniques allow printing on three-dimensional substrates. Direct printing techniques will thus be preferred to produce the piezoresistive pressure sensor on the non-planar substrate. With a wider range of printable **inks**, AJP has the advantage over inkjet printing when it comes to printable material. Especially when a pneumatic atomizer is used, ink viscosities up to 2500cp, particle sizes up to 500nm, and solid loadings up to 75wt.% are possible.

Aerosol Jet Printing (which is an indirect printing technique) is a preferred choice to produce electronics on three-dimensional substrates. However, the piezoresistive layer in the previous sensor configuration was printed using a planar screen-printing technique. To produce the sensor on the three-dimensional substrate, this technique must be adapted. In AJP, the ink is nebulized into an aerosol which is transported to the nozzle where it is continuously deposited onto the substrate. By movement of the nozzle (and) or print bed, the desired pattern is created where the line width and thickness are mainly affected by the focusing ratio, nozzle diameter, carrier gas flow rate, and stage speed. The resistance of the printed lines can be decreased by increasing the carrier gas flow rate (and) or decreasing the stage speed. Knowledge of the AJP process and its characteristics will play a vital role in the production of the sensor electrodes using the NEBULA 5X-100s aerosol jet-based printer.

Pre-and-post-printing treatments can be conducted to increase the properties of the final product. To increase the printability of the porous PA substrate, polishing can be done to decrease the surface roughness, and a corona treatment can be done to increase the surface wettability. To improve the conductivity and the adhesion to the substrate, the printed pattern can be sintered below the processing temperature of the substrate. After a review of sintering techniques, thermal sintering is preferred because of its simple nature and high obtained conductivity.

Piezoresistive sensors are chosen over capacitive sensors because they are less sensitive to electromagnetic interference and have less complicated data acquisition systems. The piezoresistive material used for the sensor undergoes a change in resistance when a force is applied. According to the literature, a planar finger-like sensor structure is more optimal and easier to produce than a sandwich sensor structure. This gives reason to implement this structure for the final design of the sensor. According to the literature, key sensor parameters are hysteresis, sensitivity, repeatability, stability, and temperature & humidity operating range. These parameters can be determined by testing.

Non-planar printing can be conducted using AJP, which is able to print on slightly curved substrates due to the relatively high standoff distance (1-5mm). When printing on non-planar substrates with bigger curvatures, a 5-axis machine is preferred although literature tells that the AJP process is able to print on surfaces that are tilted by up to 45 degrees relative to the axis of deposition. The 5 axis NEBULA 5X-100s will thus be used to produce the pressure sensor on the curved substrate.

3 MATERIALS AND METHODS

This chapter describes the materials and methods used in this master thesis. First, the project flow and methodological approach used for this master thesis are described in section 3.1. Next, the fabrication process of the 2D pressure sensor is explained in section 3.2. Section 3.3 discusses the mechanical testing setup which is used to characterize the 2D pressure sensors. Finally, the fabrication of the pressure sensor on the curved PA substrate is discussed in section 3.4.

3.1 Project flow and methodological approach

In this master thesis, an experimental approach is used to characterize and further develop pressure sensors which are produced by a hybrid manufacturing technology of AJP and screen-printing techniques. The overall flow of the experimental part of this master thesis is illustrated in Figure 3.1. First, characterization of the piezoresistive pressure sensors, printed on a flat substrate, is done using a compression setup. Next piezoresistive pressure sensors are produced onto a non-planar substrate using a combination of AJP and screen printing techniques. To do this, the printing parameters which ensure optimal conductivity along with the 5-axis printing of NEBULA-5X100s are assessed. The sensor design is made using Creo parametric 5.0, and the g-code is extracted using a previously build postprocessor. The final stage is to test the functionality of the produced sensor and provide a coupling with the readout circuit.

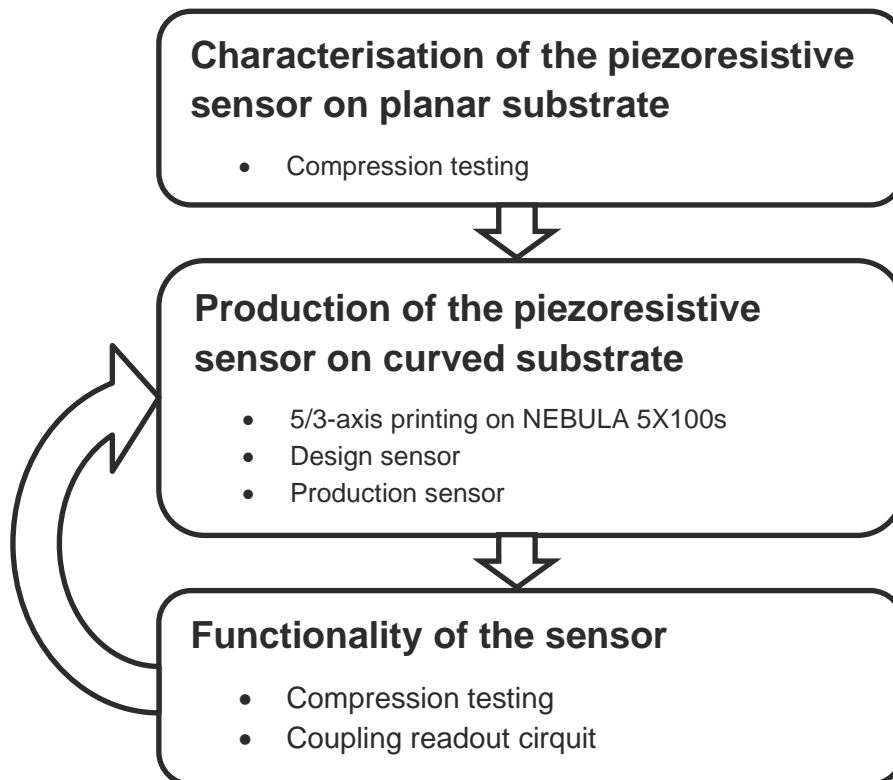


Figure 3.1: Project flow and methodological approach

3.2 Fabrication of the pressure sensor on planar substrate

The pressure sensors, which are used for the experimental compression testing, are developed by Eng. A. Verma at the advanced manufacturing laboratory of KU Leuven Campus De Nayer. More specifically, a configuration of six sensors with different dimensions is produced onto a single substrate. The range in sensor dimensions allows us to investigate the relationship between sensor size and piezoresistive behavior. The sensor circuit consists of Aerosol Jet[®] Printed silver lines which act as electrodes. The piezoresistive ink is screen printed between the electrodes and provides the active material, from which the resistance will change in function of the applied pressure. This sensor configuration is produced on a flat polyamide (PA) substrate, as shown in Figure 3.2, where the sensors are also enumerated ranging from 1 to 6. This aids in the description of a certain sensor cell e.g. “sensor PA_1” has the biggest sensing area and is located in the upper left corner of the PA substrate. This description will be used to discuss the experimental results in section 4.1. Three samples of the sensor configuration were made to increase the reliability of the experimental results. In section 4.1, these different samples will be referred to as board1, board2, and board3.

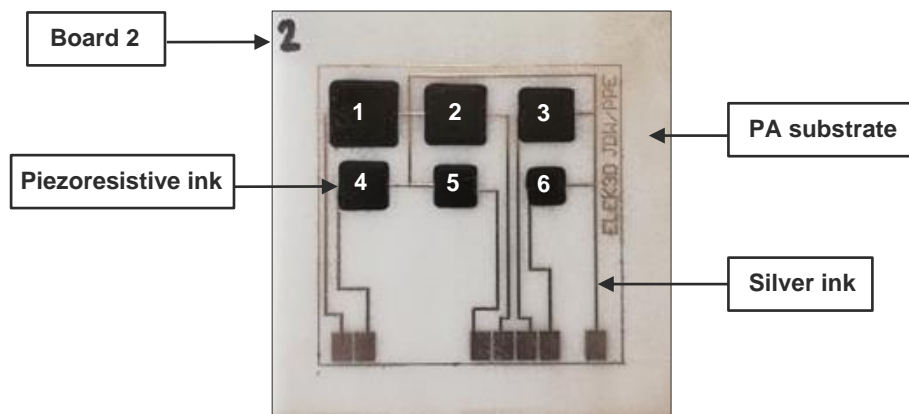


Figure 3.2: Arrangement of 6 piezoresistive pressure sensors printed on PA substrate, with a sensing area ranging from 100mm² to 25mm², and label strategy

3.2.1 Inks and substrates

This section discusses the inks and substrates that are used for the production of the piezoresistive pressure sensor on the planar substrates.

The substrate, which acts as a base for the sensor configuration, is a 3D printed polyamide (PA) board with a melting temperature ranging from 172 to 180°C and an average roughness (Ra) of 6µm. This relatively higher roughness is due to the fact that the substrate is 3D-printed. Grinding and polishing of the substrate were done to decrease the surface roughness, using 600 and 2400 grit paper. The lower surface roughness enhances the printability of the substrate and the conductivity of the printed lines.

Two types of ink were used for the production of sensors. The first type is a conductive silver ink (Metalon[®] JS A221E) which is used to print the conductive paths. The second type is piezoresistive ink (Carbon EMS CI 2050) which is used to print the piezoresistive pressure elements. More information about the mixing ratio of the two ink components (CI-2050HR and CI-2050LR) is provided in section 3.5.2. The properties of the inks are given in Table 3.1.

Table 3.1: Ink properties

Name	Metalon® JS A221E	Carbon EMS CI 2050
Technique	Ultrasonic AJ®P	Screen printing
Type	Conductive silver ink	Piezoresistive carbon ink
Solid content	40-60 wt% Ag	31 wt%
Other content	3-10 wt% 2,2-oxybisethanol 2-10 wt% isopropyl alcohol	/
Dynamic viscosity	10-20 mPas	2500 mPas
Average particle size	35 nm	/
Appearance	Brown to grey	Black
Cure temperature	120-200°C for 120min	150°C for 10min

3.2.2 Production process

The production process of the sensor board can be divided into multiple steps. First, the conductive lines are Aerosol Jet® printed onto the substrate, using the Metalon® JS A221E ink and the Optomec 300 series Aerosol Jet® printer. The printing parameters are shown in Table 3.2. Next, the conductivity of the printed lines is improved by sintering them in an oven at 150°C for 2 hours. On top of the sintered silver electrodes, the piezoresistive pressure elements are screen printed, using the Carbon EMS CI 2050 ink. Three printing passes were done with a 30µm thick screen. The conductivity of the piezoresistive pressure elements is improved by sintering in an oven at 150°C for 45min.

Table 3.2: Printing parameters for Optomec 300 series

Parameter	Value
Atomizer gas flow	65 sccm
Sheath gas flow	45 sccm
Printing speed	7 mm/s
Table temperature	23°C
Number of layers	7

3.3 Experimental setup mechanical testing

This section explains the mechanical testing setup which is used to characterize the pressure sensors printed onto the flat substrates.

3.3.1 General setup

To determine the characteristics of the sensor, mechanical testing of the sensor is required. The input of the mechanical tests is a compression force, which results in pressure. When pressure is applied to the piezoresistive element, the resistance of this element will decrease.

The force is applied by the Instron 3367 testing system which is equipped with a 5kN load cell. The change in resistance is then recorded by the Rigol DM3068 digital multimeter. The data obtained from the loadcell and the digital multimeter is then processed by a Matlab script. The experimental setup is illustrated in Figure 3.3. The following paragraph gives a detailed explanation of the reported components.

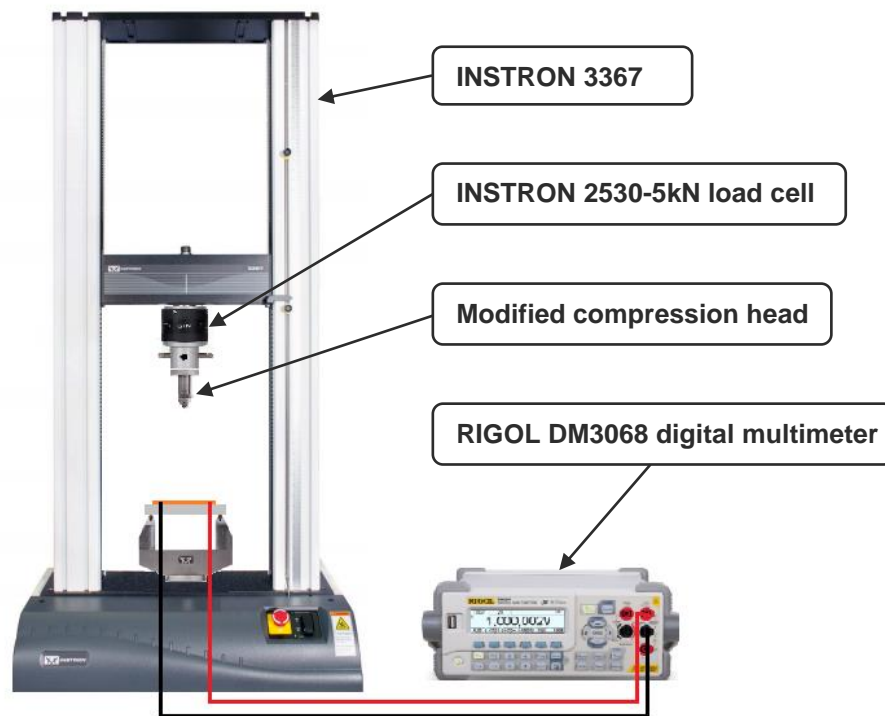


Figure 3.3 Experimental setup

The **Instron 3367** is a mechanical testing system that can perform high-quality tensile, compression, and bending tests. For the experiments conducted in this master thesis, only the compression feature is needed.

The **Instron 2530-5kN load cell** is mounted onto the crossbeam of the Instron 3367 mechanical testing system. The load cell makes sure that the correct load is applied and monitored at all times. The loadcell also allows us to zero out the tare weight of the compression head as discussed later. Before testing, the complete setup is also calibrated. During the measurement, the applied load is registered with a sampling rate of 50Hz.

The **compression head** is mounted onto the load cell and transfers the force, which is regulated by the loadcell, to a pressure exerted onto the piezoresistive material of the sensor.

The **Rigol DM3068 digital multimeter** is used to measure the change in resistance when the applied force is increased. 4-wire resistance measurement is preferred because of its higher accuracy, but because there is only a limited space to attach the probes onto the sensor, a 2-wire resistance measurement is conducted. After each measurement, the data are saved onto a removable drive. The settings of the digital multimeter are specified in Table 3.3.

Because of the difference in sampling rate between the Instron 3367 (50Hz) and the Rigol digital multimeter (2Hz), the number of recorded force data is 25 times more than that of the change in resistance over the same period of time. A Matlab code is written to combine those two data sets, which can be consulted in Appendix C: Matlab scripts. A procedure on how the Matlab code works and how to use it can be consulted in Appendix A: Procedures.

Table 3.3: Settings of the digital multimeter

Setting	Value
Measurement type	Resistance
Range	Auto range
Sampling frequency	2Hz

3.3.2 Setup improvements

The experimental setup to conduct the pressure testing experiments is improved in three different iterations. In previous experiments, a round compression head along with a three-point bending setup was used to perform the compression testing, as seen in Figure 3.4a. Because the round compression head lacks the quality to distribute the applied force evenly across the sensor surface, a new compression head was designed. The new compression head has a flat contact surface of 10-10mm to distribute the applied force evenly across the surface, as seen in Figure 3.4b. However, it was found that the substrate was bending excessively due to the three-point bending setup, influencing the measured data. Hence, the testing setup was adjusted so no bending of the substrate would occur, as seen in Figure 3.4c.

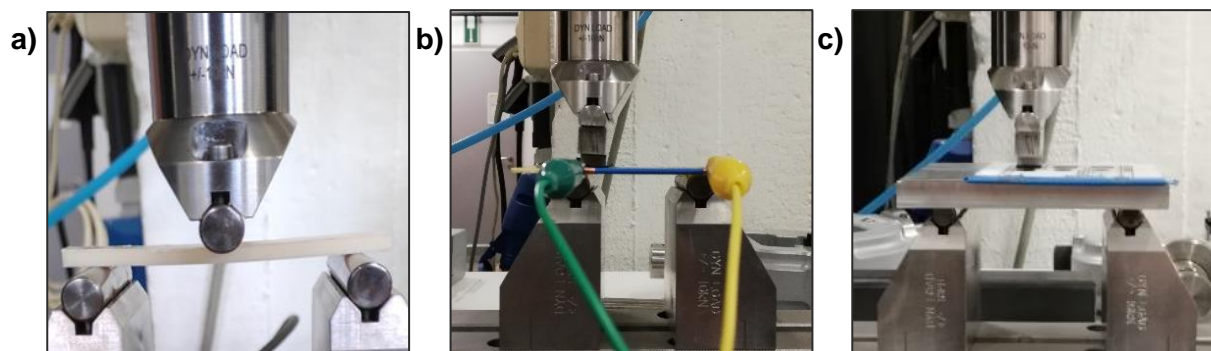


Figure 3.4: Change in experimental setup | a) first setup; b) second setup; c) third setup

3.3.3 Experimental conditions

Based on the knowledge acquired in section 2.3.4, multiple experiments are proposed to determine the characteristics of the piezoresistive pressure sensors printed onto the flat PA substrate. These experiments along with their testing conditions are discussed in the following.

A **ramping force** test will be conducted where a force-cycle, 0-125-0N, is applied to the sensors to determine which sensor size gives the highest change in resistance for a given amount of pressure. Comparing the change in resistance for increasing and decreasing force also gives information about the hysteresis of the sensors. Note that for each experiment, three measurements (repetitions) are conducted on each sensor of the three boards.

Next, a **cyclic force** test is conducted where the sensors are exposed to multiple pressure cycles, 0-125-0N, to determine the repeatability of the sensors. Finally, a **constant force** test is conducted where a force of 125N is applied over a period of time. This shows the stability of the sensor in function of the time, also known as time drift. Note that the cyclic and constant force experiments are conducted on sensor one (S1) of the three substrates, where three

repetitions were done for each sensor. Between each of these repetitions, the sensor is given 30 min time to reach again its initial condition. The conducted experiments along with the testing conditions are listed in Table 3.4.

Table 3.4: Conducted tests and testing conditions

	Ramping force	Cyclic Force	Constant force
Conducted on	PA S1-S6	PA S1	PA S1
Min force (N)	0	0	0
Max force (N)	125	125	125
Compression rate (N/s)	3	10	3
# cycles (l)	/	50	/
Holding time (min)	/	/	10

To perform the measurements with crocodile clamps, the non-conductive tape is applied over the conductive boundary, which is printed around the sensor configuration. This is illustrated in Figure 3.5a. The compression head is also equipped with a 1mm thick **rubber patch**, which has the same dimensions as the compression head, as seen in Figure 3.5b. This compensates for alignment errors and provides an insulating layer between the conductive piezoresistive material and compression head. Compression testing is done on all sensor sizes, as seen in Figure 3.2. When using a rigid compression head, the smaller sensors are exposed to a higher pressure because the force is spread over a smaller area. Using a rubber insert between the rigid compression head and the piezoresistive material allows us to spread the applied force over the same area for each sensor. Since the piezoresistive material has a thickness of only 30 μ m, the rubber insert will deform under the applied force making contact with both substrate and piezoresistive material. This way the applied load is always distributed over the area of the rubber patch, resulting in an equal pressure for each experiment no matter the sensor dimensions. This is schematically illustrated in Figure 3.5c. Vulcanized rubber is used as patch material because of its low hysteresis and high elastic properties. To increase the reliability of the results, three repetitions are performed per sensor.

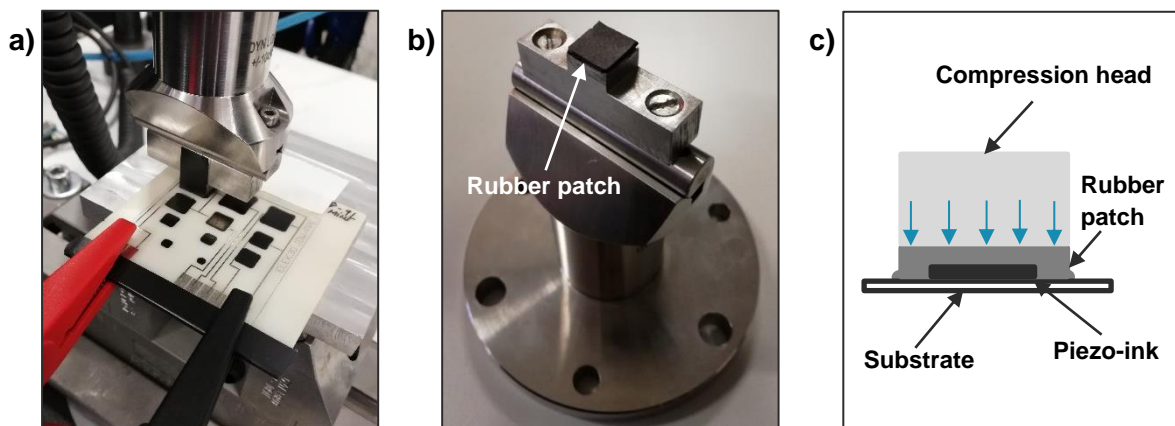


Figure 3.5: a) non-conductive tape and crocodile clamps; b) rubber patch on compression head; c) distribution of pressure through rubber patch

3.4 Printing process and conditions

This section discusses the materials and methods which are used to investigate the printing process and conditions adopted for the production of the sensor on a freeform PA substrate. The NEBULA 5X-100s AJP, which is used for the production of the sensor electrodes, is discussed along with some improvements. Next, the inks and substrates which will be used in this master are discussed, along with the experiments conducted to determine the printing conditions on the curved PA substrate.

3.4.1 NEBULA 5X-100s AJP

For the fabrication of the pressure sensor on the curved PA substrate, the NEBULA 5X-100s aerosol jet-based printer is adopted. This machine is developed at the advanced manufacturing laboratory of KU Leuven, Campus De Nayer. Over the past years, extensive research and improvements have been made to improve the printing quality. This resulted in a low-cost, 5-axis aerosol jet-based printer that can produce printed electronics with a line resolution between 100-300 μm , and which is based on pneumatic atomization. As seen in Figure 3.6, compressed air (or N_2) is provided to the input of the pneumatic atomizer (1) which leads to the aerosolization of the ink inside. This aerosolized ink will then pass through the virtual impactor (2) and finally reach the nozzle (3) where it is deposited onto the substrate. The substrate is fixed onto the 3-axis printing bed (4).

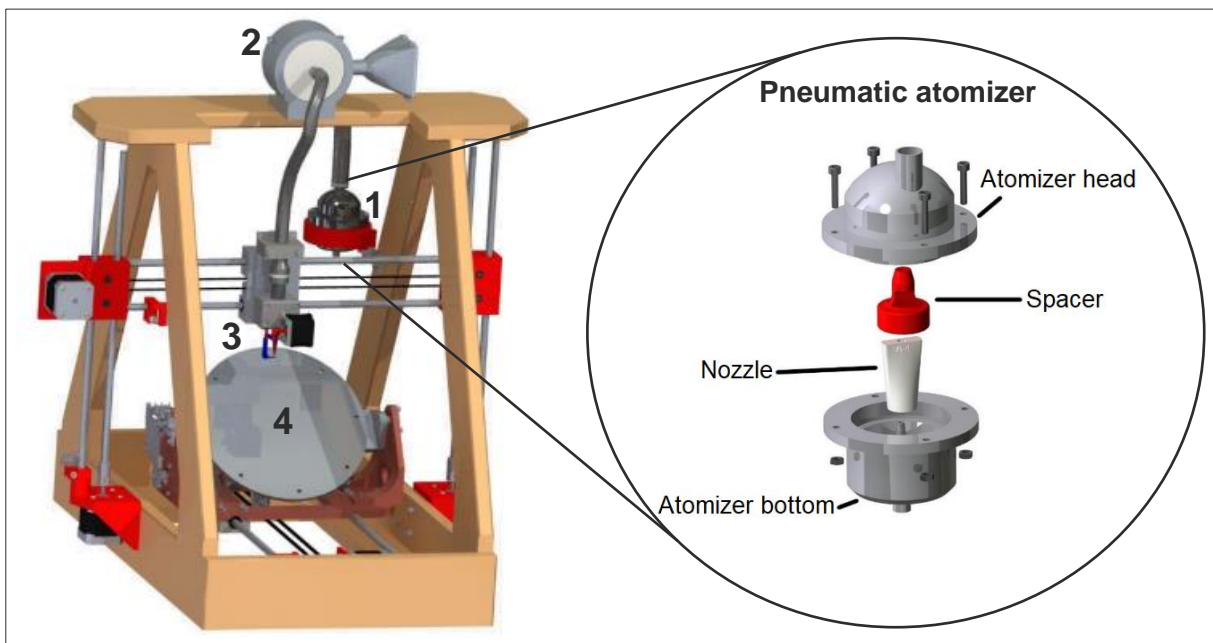


Figure 3.6: NEBULA 5X-100s Aerosol Jet based printer

The following gives a description of the main components:

Compressed air is supplied by the compressed air network of the advanced manufacturing laboratory of KU Leuven Campus De Nayer. Before entering the atomizer, the compressed air passes through a pressure regulator FESTO. This is necessary because the standard air pressure (8bar) is too high to operate the machine with. The pressure regulator thus reduces the pressure to an appropriate value, as regulated by the operator.

In the **pneumatic atomizer (1)**, the compressed air enters through the atomizer bottom, as seen in Figure 3.6. The compressed air flows through the nozzle, resulting in aerosolization of the ink by the venturi effect. The spacer keeps the nozzle in the right place and allows for a good distribution of the aerosolized ink. The atomizer head is rounded to increase aerosol flow through the atomizer. The drain channel is placed eccentrically on the atomizer head, which results in a plate impactor to prevent the distribution of large ink droplets.

In the **virtual impactor (2)**, a region of stagnant flow is used to separate droplets from the aerosol stream based on their inertia. Small droplets with low inertia are not able to pass the stagnant flow region and will be ejected, together with a large amount of carrier gas (major flow). For environmental safety, the ink particles of the excess flow are absorbed by a filter. Large droplets with high inertia are able to pass the stagnant flow region and will be transported to the deposition head (minor flow). This results in a higher density of the aerosol.

The **Nozzle (3)** consists of a syringe and Nordson EFD precision tip. The aerosol coming from the virtual impactor enters the syringe and is focused by the EDF precision tip. The leur-lock connection makes it easy to replace/change the precision tip. Different sizes of precision tips are available from Nordson EFD, as shown in Table 3.5.

Table 3.5: Nordson EFD precision tips

Color	Olive	Grey	Green	Pink	Blue	Red	Clear
Diameter (mm)	1.6	1.9	0.84	0.58	0.41	0.25	0.2
Length (mm)	31.6	31.6	31.6	31.6	31.6	31.6	31.6

The **5-axis setup (4)** of the NEBULA 5X-100s enables to print on curved substrates. 5-axis movement is obtained by the combination of the two translation axes of the deposition head in combination with the translation, and two rotation axes from the printing bed.

3.4.2 Improvements on the NEBULA 5X-100s

During the experimental part of this master thesis, improvements were made to the NEBULA 5X-100s aerosol jet-based printer to improve the ease of use and conformance of the machine. A discussion of these improvements is given in the following paragraph.

3.4.2.1 Virtual impactor

A new virtual impactor was printed using the files from Deprince et al. [75]. The production of the virtual impactor was done using Fused Filament Fabrication, on a Prusa i3 MK3S. The cross-section of this virtual impactor is illustrated in Figure 3.7a. When testing this design with leak detector, it was found that the printed screw thread did not guaranty an airtight fit as expected. We also noticed air escaping through the pores of the printed material. Because the ink contains silver nanoparticles which are harmful to the human body when inhaled, the distribution of the aerosolized ink to the environment should be avoided.

This led to the improved design as seen in Figure 3.7b, where an airtight seal is provided by applying a flexible sealing ring between the top and bottom part. The sealing ring is then brought under tension using the bolts which also provide the joining of top and bottom parts. A technical drawing of the virtual impactor can be consulted in Appendix B: Technical drawings.

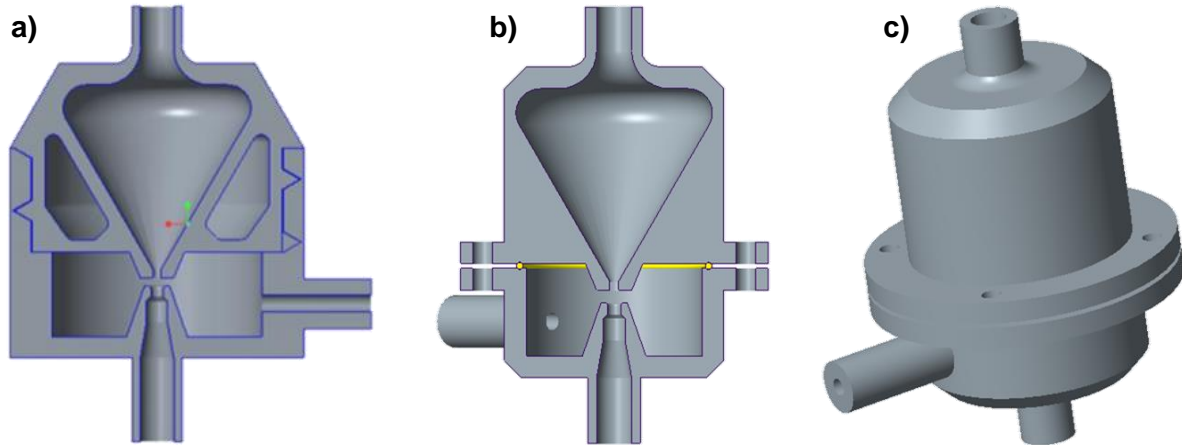


Figure 3.7: Virtual impactor | a) cross-section of the previous design; b) cross-section of the improved design; c) full view of the improved design

In an attempt to make the surface of the printed virtual impactor airtight, the parts were produced using Acrylonitrile Butadiene Styrene (ABS) instead of polylactic Acid (PLA), because this allows us to smoothen the surface using acetone. The acetone melts the outer ABS surface of the part, which results in a pore-free surface when hardened again. This way, almost no air can penetrate the surface of the part. The acetone treatment process can be consulted in Appendix A: Procedures. On the other hand, it was found that the ABS reacts with the ink inside, resulting in thickening of the ink. This was confirmed by David Bogaerts who used similar methods in his master thesis. This led to the production of the virtual impactor using PLA filament but with an increased number of outer layers (5 layers at 0.2mm layer thickness).

3.4.2.2 Filter

The filter is mounted on the exhaust flow of the virtual impactor. The function of the filter is to prevent ink particles from entering the environment. In previous work conducted by Deprince et al. [75], a filter design was made, but both filter and files were lost over the years. This gave reason to design a new filter as illustrated in Figure 3.8a. The filter material is compressed between the grids and mounted onto the holder. The grids are chamfered to increase airflow. The production of the filter was done using Fused Filament Fabrication on a Prusa i3 MK3S. A technical drawing of the filter can be consulted in Appendix B: Technical drawings.

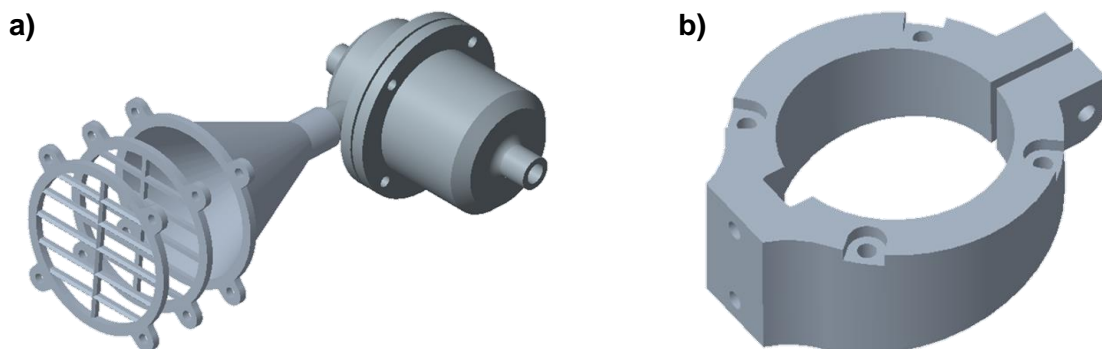


Figure 3.8: a) filter; b) bracket atomizer

3.4.2.3 Bracket atomizer

In a previous optimization study conducted by Deprince et al. [75] at the advanced manufacturing laboratory of KU Leuven Campus De Nayer, a new atomizer design was proposed to increase ink aerosolization. To install the new atomizer onto the frame of the NEBULA 5X-100s, a new bracket had to be designed as shown in Figure 3.8b. A technical drawing of the bracket can be consulted in Appendix B: Technical drawings.

3.4.3 Inks and substrates

The inks and substrates which are used for the production of the pressure sensor on the freeform substrate are discussed in the following section.

Two types of **ink** were used for the production of the sensors onto the freeform substrate. The first type is conductive silver ink (CUR AG-001) which is used to print the conductive paths. The second type is piezoresistive ink (Carbon EMS CI 2050) which is used to print the piezoresistive pressure elements. More information about the mixing ratio of the two ink components (CI-2050HR and CI-2050LR) is provided in section 3.5.2. The properties of the inks are given in Table 3.6.

Table 3.6: Ink properties

Name	CUR AG-001	Carbon EMS CI 2050
Technique	Pneumatic AJP	Screen printing
Type	Conductive silver ink	Piezoresistive carbon ink
Solid content	19%wt	31 wt%
Other content	10-30% silver nanoparticles 25-55% 2-Phenoxyethanol 0-15% Propylene carbonate 0-35% butan-1-ol; n-butanol	/
Dynamic viscosity	8,2 mPas	2500 mPas
Average particle size	100 nm	/
Appearance	Dark grey	Black
Cure temperature	120-200°C	120°C for 10min
Supplier	AGFA	EMS

Multiple **substrates** are used during the experimental part of this master thesis. In the first stage of printing with the NEBULA 5X-100s, test prints are done using the glass slides which are illustrated in Figure 3.9a. These slides are convenient to use for quick testing because they are reusable and can withstand high sintering temperatures. Before printing on the slides, they are cleaned with isopropanol and cloth. After studying the results of the printed lines, the glass slides can be reused by removing the sintered silver ink using isopropanol and cloth. In the second stage, printing will be done on the flat PA substrate as illustrated in Figure 3.9b. The PA substrate is produced by Materialise® using selective laser sintering (SLS). Because of this production method, the surface of the substrate has a relatively high roughness. The roughness can be decreased by polishing of the substrate until the desired surface quality is

reached. For the application of this master thesis, freeform printing of the sensor is done on the curved PA substrate, as illustrated in Figure 3.9c, which has a curvature with a radius of 95mm. The melting temperature of polyamide is around 180°C. During sintering, one must keep in mind to stay below this melting point.

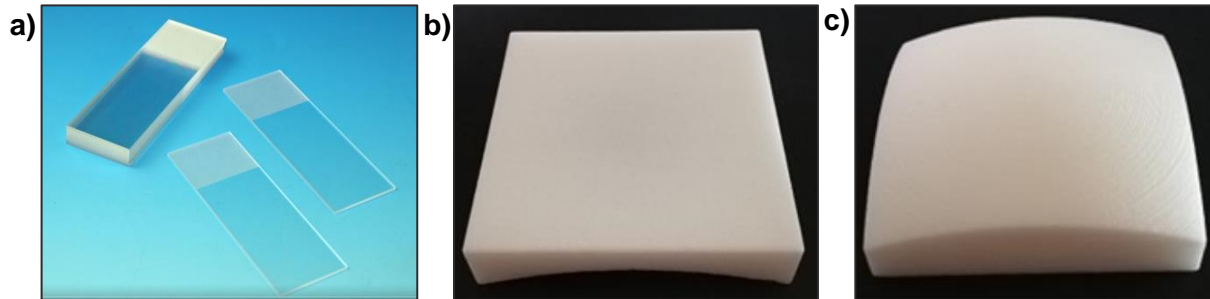


Figure 3.9: Substrates | a) glass slides [website VWR]; b) flat PA substrate; c) curved PA substrate

3.4.4 Determining printing parameters for the PA substrate

This section discusses how the optimal printing parameters of the NEBULA 5X-100s are assessed for the PA substrate. During the printing process, input parameters play a vital role in the characteristics of the final product. Experiments are conducted to determine the optimal printing and sintering parameters for the PA substrate. Because it is hard to predict the outcome of these experiments, an iterative approach is used where the parameters are altered after each iteration to increase the conductivity of the printed lines. The initial printing parameters are based on previous work conducted by Miriam Seiti at the advanced manufacturing laboratory of KU Leuven Campus De Nayer. To determine the optimal process parameters, three iterations were conducted where process parameters as the substrate, number of layers, sintering time, and sintering temperature were investigated. From these experiments, we can conclude that we are able to print on the PA substrate when polished with 2400 grit paper. We also noticed that the minimal number of printed lines to obtain proper conductivity is around 30 printing layers. To obtain maximal conductivity, it was also found that the printed lines need to be sintered at 150°C for 4 hours. This resulted in the optimal process parameters as illustrated in Table 3.7. When designing an electrical circuit, knowledge of the line width is useful to create a filled region with the right amount of overlap. In this master thesis, the line width will be used to design the readout pads for the sensor configuration.

Table 3.7: Process parameters for PA substrate

Parameter	Value	Parameter	Value
Nozzle diameter	0.84 mm	Substrate	Polished PA (2400grt)
Stage speed	50 mm/min	Layers	30, 40, 50
Atomizer pressure	1.5 bar	T_{sinter}	150°C
Standoff-distance	1.5 mm	t_{sinter}	4h

The production and measurement devices used to perform these experiments are listed below:

The Weiss Technik Heraeus oven in the materials science lab of KU Leuven Campus De Nayer is used to sinter the printed lines. By adjusting the temperature of the oven or altering

the sintering time, different sintering conditions can be achieved. This is an important feature as will be shown in section 4.2 where sintering conditions play a vital role in the conductivity of the printed lines.

The Hiox KH 8700 digital microscope in the materials science lab of KU Leuven Campus De Nayer is used to examine the printed lines. Using the low range resolution lens, an enlarged view of the printed lines can be studied to obtain critical information about the printing and sintering process. Using this tool, measurements can be made to determine the line width, which is especially interesting for the design of the sensor circuit, and to inspect the overall quality of the printed patterns before and after sintering (overspray, cracks, etc...)

The Hama EM393B multimeter is used to examine the conductivity of the printed lines. The resistance over a certain length can be measured by applying the probes of the multimeter onto the ends of the printed lines. Note that the adhesion between the printed lines and the substrate is not great, and one must be cautious not to damage the lines with the probes.

3.5 Production of sensing device on non-planar substrate

3.5.1 Sensor design

This section provides a detailed explanation of the sensor design. The construction of the sensor consists of 3 major parts (substrate, electrodes, and piezoresistive ink) as illustrated in Figure 3.10c. The electrodes are printed on the curved substrate using the NEBULA 5X-100s aerosol jet-based printer. Once sintered, the piezoresistive element is screen printed between the electrodes. The design for the sensor was made using Creo. Figure 3.10a shows a representation of the sensor design on a flat surface. However, the surface of the substrate is curved as seen in Figure 3.10b. In order to produce the sensor on the curved substrate, a three-dimensional model of the sensor was developed. In previous research, the NEBULA 5X-100s was used to print electronics on flat substrates, where the g-code was created either by hand or Creo Manufacturing. Since the sensor will be produced on a curved substrate, three or five-axis movement is needed to form the conductive paths. Creo Manufacturing will be used to extract the g-code. A step-by-step procedure to create the g-code from the envisioned sensor design can be consulted in Appendix A: procedures.

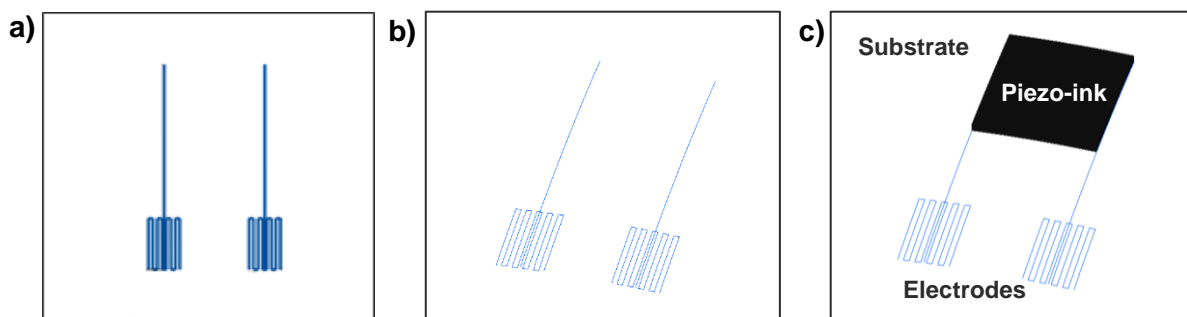


Figure 3.10: a) 2D sensor sketch; b) projected sketch on curved substrate; c) complete sensor with piezoresistive material between electrodes

3-axis machine movements are first used to create the toolpaths, given the limited curvature of the substrate. The use of a 5-axis postprocessor is also investigated, as discussed later.

Those 3-axis toolpaths follow an exact replica of the substrate curvatures when i,j,k-coordinates are used to create the g-code. A disadvantage of the 3-axis machining is that the printing nozzle is not always perpendicular to the surface or the substrate, which restricts us to curvatures of up to 45 degrees relative to the axis of deposition to reach reliable deposition.

3.5.2 Screen printing of the piezoresistive ink

3.5.2.1 Carbon EMS CI 2050 piezoresistive ink

Carbon EMS CI 2050 piezoresistive ink is used to perform screen printing. The ink is composed of two components which must be mixed to obtain optimal piezoresistive properties. The first component is CI-2050HR (High Resistance), which contains the conductive carbon black particles. The second component is CI-2050LR (Low Resistance), which forms the polymer matrix around the carbon black particles. The composition of the ink does not only affect the piezoresistive properties but also influences the initial resistance of the piezoresistive material. The more wt% CI-2050LR is used in the composition of the ink, the higher the electrical resistance will be. Since the readout circuit has a maximal operating range of 40k Ω , the electrical resistance of the screen-printed ink must be kept below this value. According to the data from the ink supplier and experiments conducted on the curved PA substrate, an optimal ratio of 60wt% CI-2050HR: 40wt% CI-2050LR was found. This ratio will thus be used to produce the sensors onto the curved PA substrate.

3.5.2.2 Screen printing

The next step in the production of the pressure sensor is screen printing the piezoresistive ink between the electrodes. This completes the sensor circuit as shown in Figure 3.11a. To perform the screen printing, a patterned metal screen is used as illustrated in Figure 3.11b. The screen consists of a metal sheet with a thickness of 30 μm , which is stretched over an aluminum frame. For our application, only the upper left square in the pattern, which measures 10x10mm, is used. Normally screen printing is done on flat surfaces. However, the surface of the PA substrate on which the sensor electrodes are printed is curved. To overcome this problem a squeegee is designed, as illustrated in Figure 3.11c, where the edge has a curvature exactly the same as the curvature of the substrate. The technical drawing of the squeegee can be consulted in Appendix B: Technical drawings. Because the screen is so thin, locally elastic deformation of the screen is possible, which allows the screen to follow the curves of the substrate. The slight deformation of the screen in combination with the curved edge of the squeegee allows to perform screen printing onto the curved substrate. A detailed explanation of the screen printing procedure can be consulted in Appendix A: Procedures.

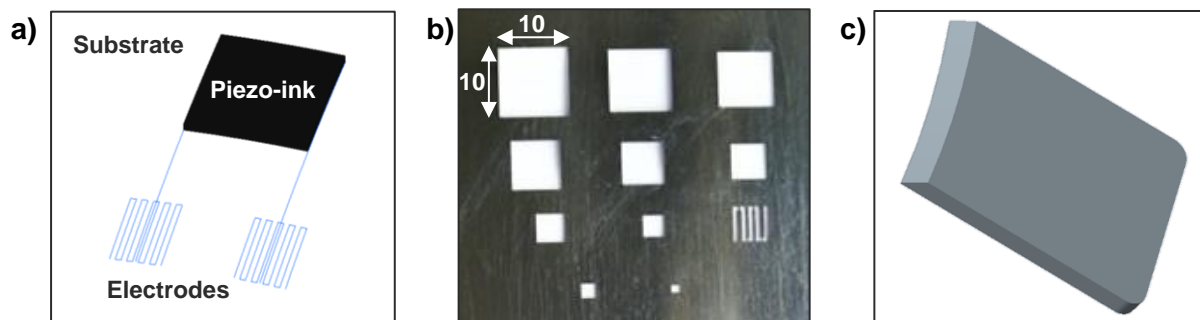


Figure 3.11: a) position of piezo-ink between electrodes; b) screen for printing; c) curved squeegee

3.5.3 Coupling with the readout circuit

3.5.3.1 Conductive epoxy adhesive

The coupling between the piezoresistive pressure sensors and the readout circuit is provided by conductive copper wires (Figure 3.12a). Soldering the wires directly onto the contact pads would exceed the maximal process temperature of both the contact pad and substrate. To overcome this problem, conductive epoxy adhesive is used to attach the wires onto the contact pads. The conductive epoxy adhesive consists of two components. The first component (Bis-F Epoxy Resin Metallic Silver) is mixed with the second component (Aliphatic Amines Metallic Silver) at a 1 to 1 volume ratio. The conductive epoxy adhesive hardens at room temperature and provides a conductive connection between the contact pads and output wires.

3.5.3.2 Pull relief

To prevent tension from being applied directly onto the connection between the contact pads and the output wires, a pull relief has been designed as seen in Figure 3.12b. The pull relief is mounted to the side of the PA substrate. When tightening the bolt, the output wires are clamped between the pull relief and the substrate, as illustrated in Figure 3.12c. This way, when external tension is applied to the wires, the forces will be absorbed by the pull relief avoiding failure of the connection between output wire and contact pad.

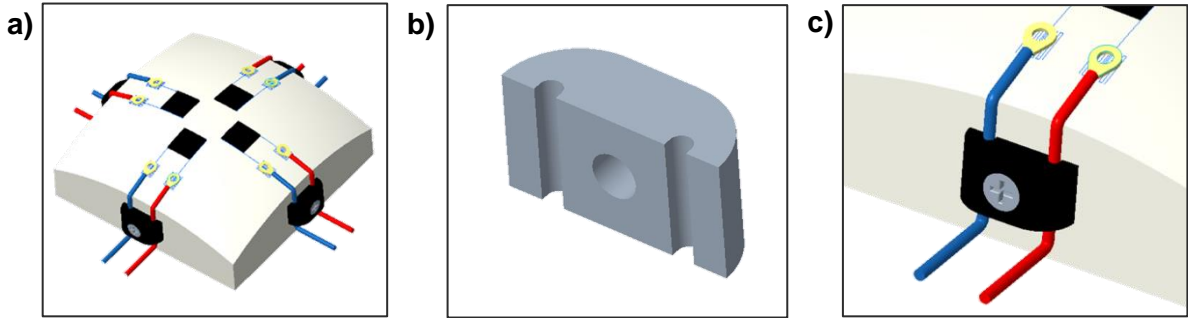


Figure 3.12: a) Coupling readout hardware; b) CAD pull relief; c) Pull relief in assembly

4 EXPERIMENTAL RESULTS AND DISCUSSION

This chapter consists of three parts in which the results of the experiments are reported. Section 4.1 describes the results that were obtained for the sensor characterization. The results of the experiments regarding the printing parameters of the NEBULA 5X-100s aerosol jet-based printer are discussed in section 4.2. Section 4.3 discusses the production process of the piezoresistive sensor with respect to AJP of the sensor electrodes, screen printing of the piezoresistive ink, and providing a coupling with the readout circuit.

4.1 Experimental results compression testing

4.1.1 Ramping force

During the ramping force test, the force is increased from 0 to 125N with a compression rate of 3N/s. The change of resistance in function of the applied pressure for each of the sensor sizes and on each of the three different boards is illustrated in Figure 4.1, along with the combined data of all the boards together. The mean sensitivity and standard deviation for the three boards can be consulted in Table 4.1, along with the mean sensitivity and standard deviation of all data combined.

When looking at the measurements, We can see that the sensors have two regions of sensitivity, which are caused by the compressibility of the material. When pressure is applied, the composite layer gets compressed fast at first resulting in high sensitivity. When a certain threshold is reached, further compression of the composite layer decreases while the applied pressure is increased, resulting in a decrease in sensitivity. The first region ranges from 0-0.1MPa and has a high sensitivity, while the second region ranges from 0.1-1.25MPa and has a notable lower sensitivity. We can also see quite some difference in the total change of resistance for the different sensor sizes over the multiple boards (standard deviation), particularly for the high sensitivity region. According to the literature, this can be due to the fact that the amount of conductive filler particles can vary in the batch of prepared ink, resulting in different piezoresistive characteristics from batch to batch. On the other hand, there is no visible relationship between the dimensions of the sensor (contact area) and the change in electrical resistance.

Table 4.1: Mean sensitivity and standard deviation for the two regions of sensitivity (low & high load)

Board	Region 1 (low load)		Region 2 (high load)	
	Mean sensitivity (Ω/MPa)	Std (Ω/MPa)	Mean sensitivity (Ω/MPa)	Std (Ω/MPa)
1	120.52	47.06	6.18	0.74
2	113.52	26.86	7.57	1.01
3	106.60	16.83	6.39	0.33
All	117.63	17.61	6.39	0.49

When looking at the results of Table 4.1, we can conduct that the sensitivity in the first region is about 20 times higher than the sensitivity in the second region. The standard deviation of the sensitivity is also about 40 times higher in the first region than in the second region. From this, we can conduct that although the first region is the most sensitive, it is also more unpredictable than the second region which is less sensitive but more predictable. Since the mean sensitivity of both regions is more or less the same for all of the sensors on the three boards, we can conclude that the sensor size does not influence the sensitivity.

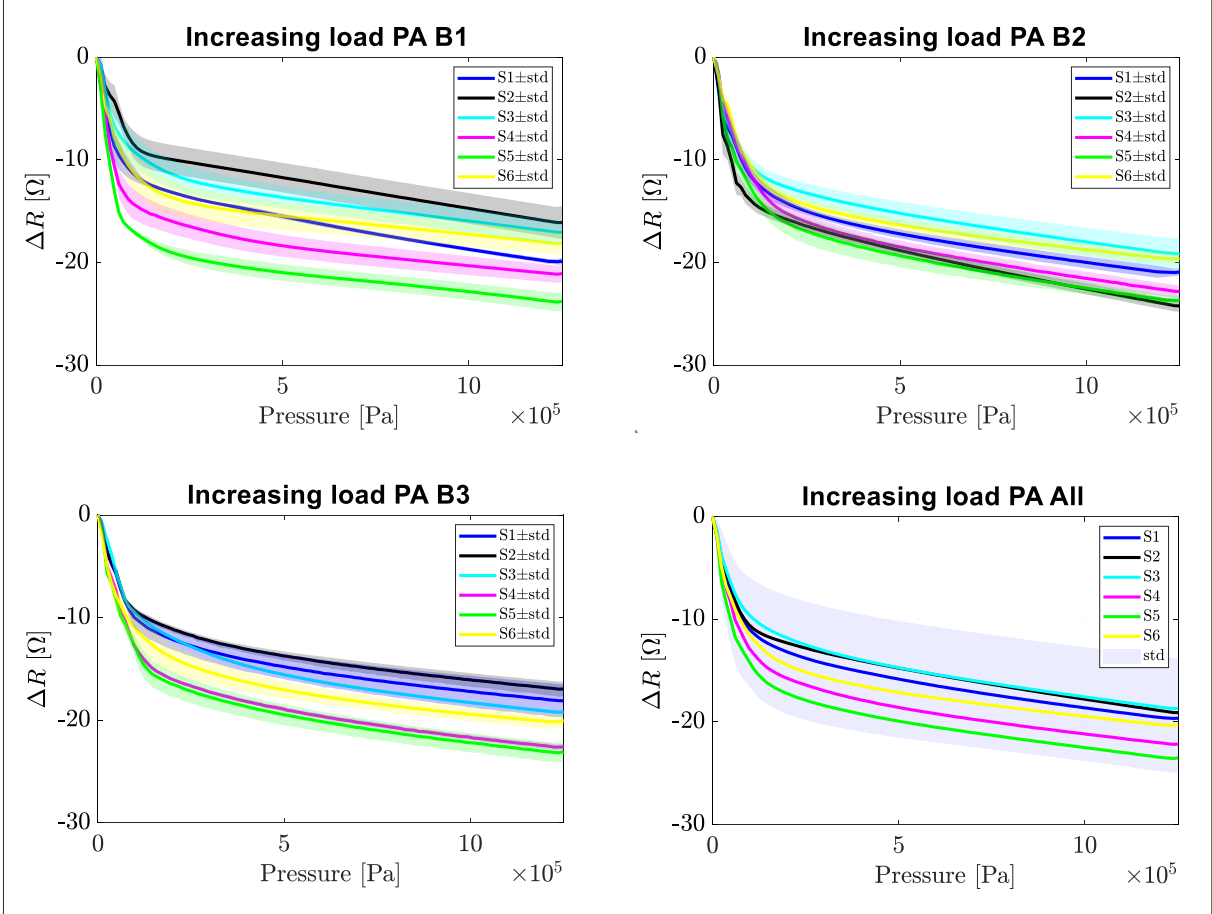


Figure 4.1: Increasing load | change in resistance in function of pressure

4.1.2 Hysteresis

During the hysteresis test, sensor one of each board is exposed to a loading and unloading cycle. First, the force is increased from 0 to 125N with a compression rate of 3N/s. Afterward, the force is decreased again from 125 to 0N with a negative compression rate of -3N/s. The change of resistance in function of the applied pressure is illustrated in Figure 4.2, along with the combined hysteresis data of sensor one for all boards combined.

When looking at the results, we can see that the change in resistance is higher during the loading cycle than during the unloading cycle. This phenomenon is called the hysteresis of the sensor and can be seen as the area between the loading and unloading cycle. From this we can conduct that the hysteresis is particularly present in the region of high sensitivity, although it is only in small amounts.

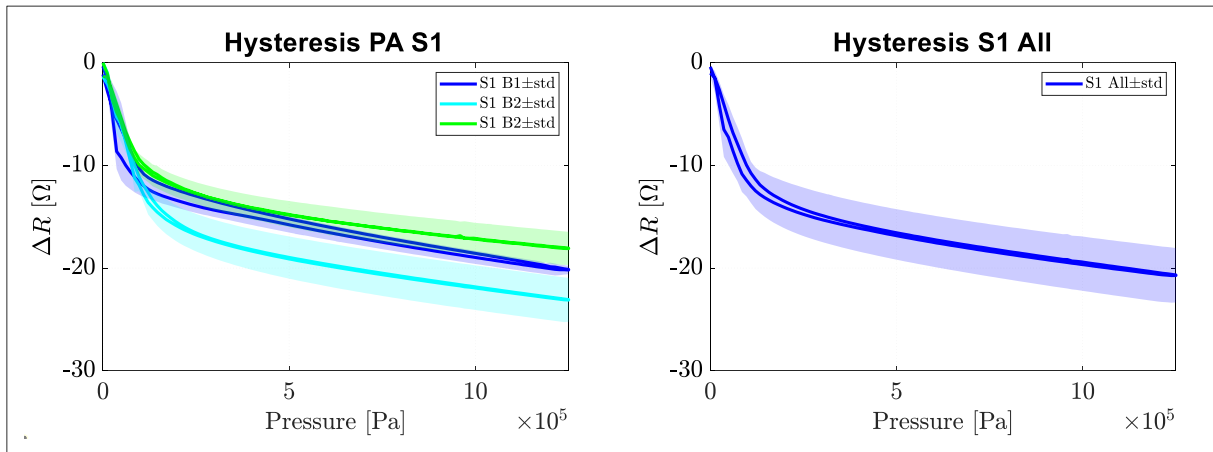


Figure 4.2: Hysteresis | change in resistance in function of pressure

4.1.3 Time drift testing

During the time drift test, sensor one of each board is exposed to a force that increases from 0 to 125N with a compression rate of 3N/s. Afterward, the force is kept constant at 125N over a period of 600s. The change of resistance in function of time is illustrated in Figure 4.3, along with the combined time drift data of sensor one for all boards combined.

When looking at the results we can see that the change in resistance decreases $13,16 \pm 3,84\%$ over a period of 600s. This is a rather high drift as compared to the literature where time drift values of 5% are reported. During the time drift, relaxation of the composite occurs, resulting in better stability of the polymer matrix. This results in improved stability, as can be seen in Figure 4.3, where the change in resistance seems to evaluate to a near-constant value.

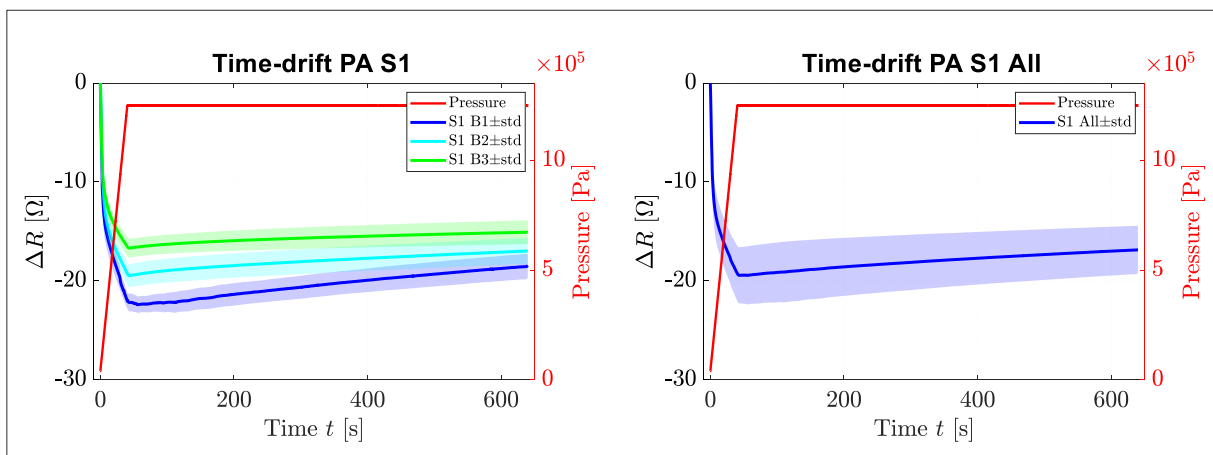


Figure 4.3: Time drift | change in resistance at 125N in function of time

4.1.4 Cyclic force

During the cyclic force test, sensor one of each board is exposed to 50 loading and unloading cycles where the load increases and decreases between 0 and 125N at a compression rate of 10N/s. The change of resistance in function of the number of cycles is illustrated in Figure 4.4. Figure 4.4 also shows the combined cyclic data of sensor one for all boards combined. When looking at the results we can see that the change in resistance decreases $28,34 \pm 16,95\%$ over a period of 50 cycles. This is a rather high change in resistance as compared to the literature where a change in resistance of 8% is reported under cyclic loading. During the cyclic loading,

relaxation of the composite occurs, resulting in better stability of the polymer matrix. This so-called ‘mechanical training’ results in improved stability and repeatability of the sensor. The improvement of the stability can also be seen in Figure 4.4, where the change in resistance seems to evaluate to a constant value.

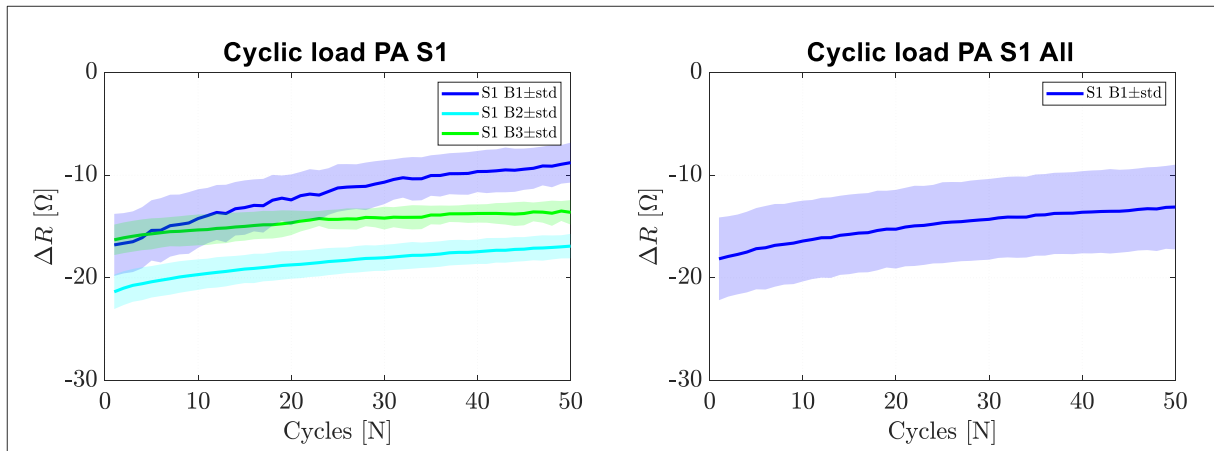


Figure 4.4: Cyclic force | change in resistance in function of loading cycles

4.1.5 Conclusion

From the results of the previous experiments, we can conclude that the piezoresistive sensors have a mode of high sensitivity and low reliability ranging from 0 to 0,1MPa, where there also is a slight amount of hysteresis, opposed to a second mode with low sensitivity and high reliability which ranges from 0,1 to 1,25MPa. We can also conclude that the sensor size does not influence the sensitivity of the sensor and that the change in resistance decreases in function of both time and number of compression cycles.

4.2 Printing parameters NEBULA 5X-100s

This section reports the results that were obtained for determining the optimal printing parameters of the NEBULA 5x-100s on PA substrate. To determine these optimal printing parameters, experiments are conducted as explained in section 3.4.4. The results of these experiments are discussed in what follows.

4.2.1 Results prior experiments

To investigate the influence of the number of printed layers on line width and resistance, a first experiment is conducted where multiple lines with different amounts of print passes were printed on PA substrate. From these results, we can conduct that the line width increases with the number of layers. We also notice that the lines do not conduct until 25 layers are printed and that the resistance seems to decrease with an increasing number of layers. In a second experiment, silver lines are printed onto a glass substrate. This way we can increase the sintering temperature and time without risking melting the substrate. From these results, we can conclude that a higher sintering time and temperature were needed to obtain good conductivity. The results of these experiments can be consulted in Appendix: D.

4.2.2 Results final experiment

From the combined results of the prior experiments, we can decide that the conductivity increases with an increasing number of layers and sintering time and temperature. This led to a final experiment where silver lines were printed on the polished PA substrate. To increase the conductivity, more print passes were used than in previous experiments along with a sintering temperature and time of respectively 150°C and 4h. Microscopic images of the lines with different amounts of layers are illustrated in Figure 4.5.

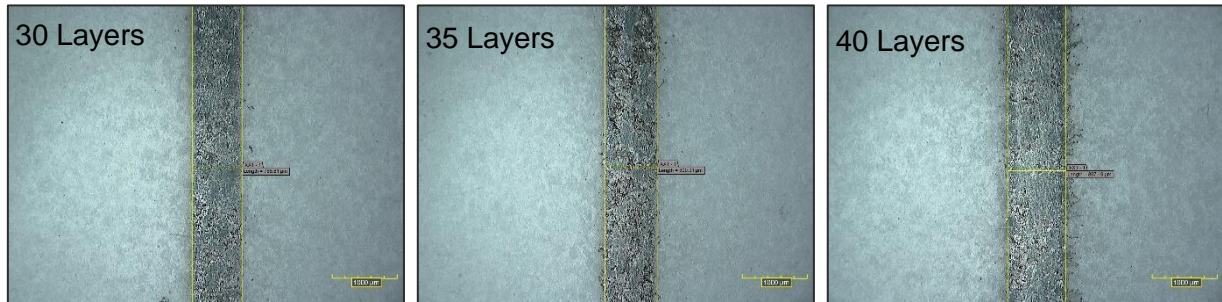


Figure 4.5: Silver lines printed on polished PA substrate after sintering

When looking at the microscopic images, we can see that the amount of deposited ink increases with the number of printed layers. This is also reflected in the average line width of the printed layers, which is illustrated in Table 4.2 along with the average electrical resistance of the lines.

Table 4.2: Line width and conductivity on polished PA after sintering i.f.o. number of layers.

Number of layers	Average line width (μm)	Average resistance (Ω)
30	768.01	157.42
35	805.23	84.27
40	900.00	43.91

From these results, we can conduct that an increase in printed layers results in an increase in line width and conductivity. When compared with the results of the prior experiments, it is remarkable that there is a big increase in conductivity (2.16 k Ω at 30 layers \leftrightarrow 157.42 Ω at 30 layers). This is caused by the higher sintering temperature (150°C) and longer sintering time (4h).

4.2.3 Conclusion

From the conducted experiments, it is clear to see that an increase in the number of layers results in increased line width and conductivity. We also notice that better conductivity is achieved at higher sintering temperatures (150°C), and longer sintering times (4h).

4.3 Production of the sensor circuit

This chapter describes the production of the sensor circuit. First, the results of the production of the sensor electrodes on the curved PA substrate are discussed. Next, the results of the screen printing process are given along with the coupling of the circuit with the readout hardware.

4.3.1 AJP of the sensor electrodes

This section contains the results that were obtained for AJP of the sensor electrodes. First, a proof of concept is conducted to estimate and prevent possible problems that might occur during the printing process. With these results, an improved sensor design is made and manufactured.

4.3.1.1 Proof of concept

The design of the sensor electrodes, as seen in Figure 4.6a, was made using Creo as discussed in section 3.5.1. The improved postprocessor “uncx01.p05” is used to extract the 3-axis g-code.

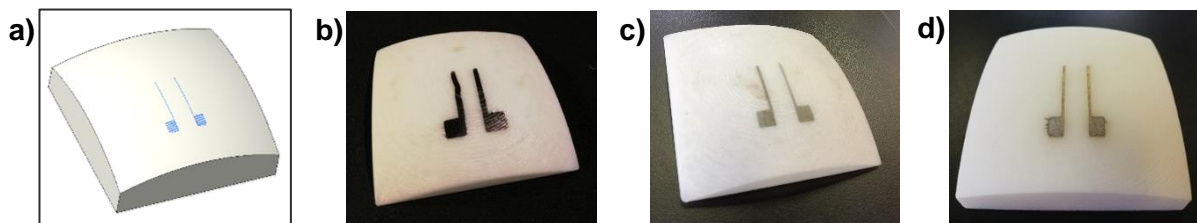


Figure 4.6: a) CAD sensor electrode design; b) pattern tested on PLA with text marker; c) pattern tested on PLA with AJP; d) sensor electrodes printed on PA substrate

First, a proof of concept is conducted where the g-code is tested on a PLA replica substrate with a text marker mounted on the position of the nozzle, as seen in Figure 4.6b. This is done to save on silver ink and PA substrates. From the results of this experiment, we can conduct that the machine executes the g-code properly. Next, the sensor electrodes are Aerosol Jet Printed onto a PLA replica substrate, as seen in Figure 4.6c. This is done to check if the ink is deposited properly onto the curved substrate without using one of the good PA substrates. Finally, production of the sensor electrodes onto the PA substrate is conducted, as seen in Figure 4.6d. Production parameters are used as described in Table 3.7 with a total of 20 printed layers. Although the electrodes look nicely printed, their conductivity is on the lower side with a resistance of approximately 950Ω over the entire length of one electrode. This is not acceptable and gives reason for an improved sensor design.

4.3.1.2 Improved sensor design

The improved sensor design is illustrated in Figure 4.7a. To improve printability, the sensor design is divided into four parts which can be printed separately. The four parts list: left electrode, left contact pad, right electrode, and right contact pad. Note that the workpiece cannot be removed from the build plate and that the workpiece zero point must be maintained during the printing process to avoid misalignments. The g-code can be consulted in Appendix

E: G-code. The length of the electrodes is shortened to 20mm so there is less opportunity for cracks to occur. Also, note that the distance between the two electrodes is set to 9mm. The piezoresistive material will be screen printed between the electrodes using a square pattern of 10x10mm. A slight under dimensioning of the distance between the electrodes (9mm as opposed to 10mm) will compensate for any alignment issues in the process and guarantees a proper connection. The contact pads and electrodes are made overlapping. This ensures a good connection, with a minimal increase in electrical resistance. The distances between neighboring lines in the meander structures, which form the contact pads, are set to 0.4mm. This value was based on the results of the experiments conducted in section 4.2.2, which showed that the line width of the printed lines averages around 0.8mm. This implies that there is an overlap of 50% between every neighboring printing pass, which results in a completely filled area with excellent conductivity. The contact pads will be used as a connection point with the readout hardware.

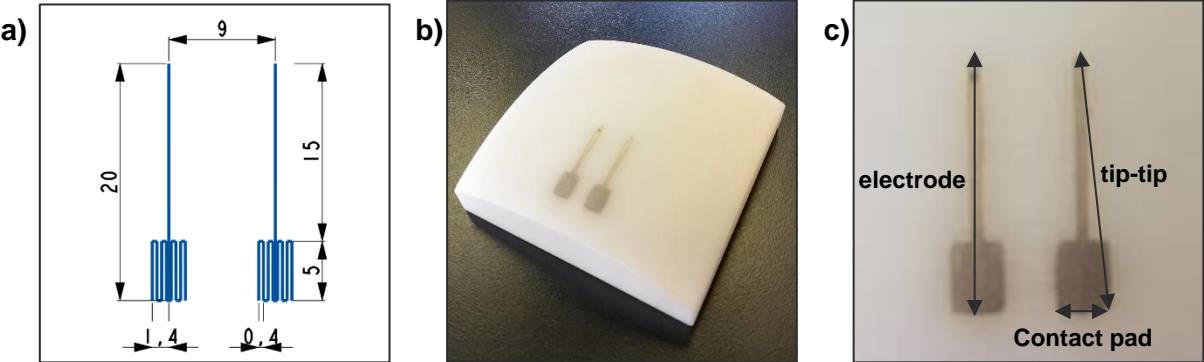


Figure 4.7: a) improved sensor design; b) sensor electrodes printed on curved PA substrate; c) top view of electrodes with indications

The sensor electrodes are produced onto the curved PA substrate as seen in Figure 4.7b. Production parameters are used as described in Table 3.7 with a total of 40 printed layers, which is double the amount used in the proof of concept. The resistance of the sensor circuit is measured in three different ways, as shown in Figure 4.7c. A distinction is made between the resistance of the electrode, the contact pad, and the total tip-to-tip resistance of the electrode. The values of these measurements are reported in Table 4.3. From these measurements, we can conclude that the electrodes are printed very well, with a biggest tip-to-tip resistance of only 16.56Ω. This is negligible compared to the resistance of the piezoresistive material, screen printed between the electrodes, which will be in the kilo-ohm range.

Table 4.3: Electrical resistance of different parts sensor electrodes

	Average resistance left (Ω)	Average resistance right (Ω)
Electrode	15.43	14.19
Contact pad	1.65	2.02
Tip-tip	16.56	15.41

4.3.1.3 Sensor matrix configuration

Because of the successful production of the improved sensor design onto the PA substrate, a design for a sensor configuration consisting of four pairs of sensor electrodes is made as

illustrated in Figure 4.8a. The g-code used for this sensor configuration is the same as for the improved sensor design and can be consulted in Appendix E: G-code. The four pairs of electrodes are then produced with the previously mentioned g-code by rotating the substrate 90° around the c-axis for every different pair of electrodes.

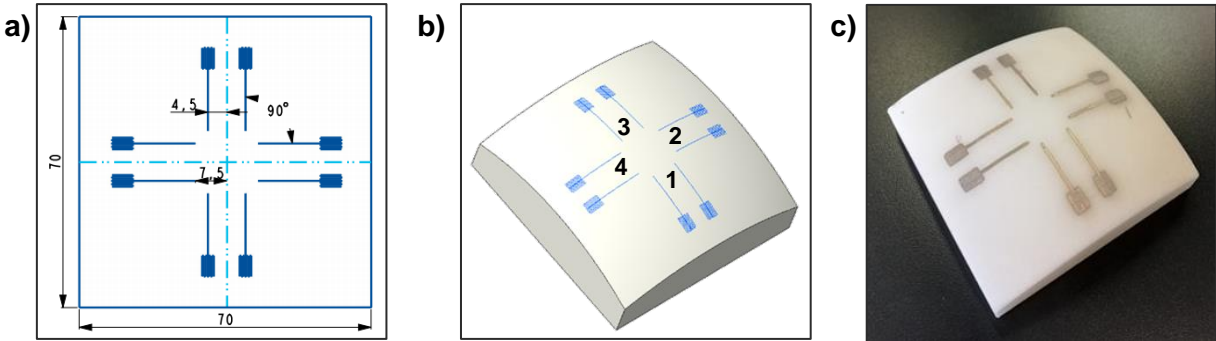


Figure 4.8: a) sensor configuration design; b) sensor electrode configuration printed on PA substrate; c) indications for table

The sensor configuration is produced onto the curved PA substrate as seen in Figure 4.8c. Production parameters were used as described in Table 3.7 with a total of 40 printed layers. Again, the resistance of the sensor circuit is measured in three different ways, as shown in Figure 4.7c. Since the circuit now consists of 4 pairs of electrodes, enumeration is used as illustrated in Figure 4.8b. The values of these measurements are reported in Table 4.4.

Table 4.4: Electrical resistance of different parts sensor configuration

#	Average resistance left (Ω)			Average resistance right (Ω)		
	Contact pad	electrode	Tip-tip	Contact pad	electrode	Tip-tip
1	1.65	15.43	16.56	2.02	14.19	15.41
2	2.21	18.78	19.02	3.03	26.03	26.43
3	2.15	27.58	29.29	2.70	23.01	23.35
4	2.29	35.17	36.49	2.66	58.20	60.04

From these measurements, we can conduct that the electrodes are printed very well, with a biggest tip-to-tip resistance of only 60.04 Ω . It is also noteworthy that there are slight differences in the electrical resistance between the different electrodes, although the values of electrical resistance are all in the same range. For example, the tip-tip resistance of the right electrode of sensor four is almost four times higher than the tip-tip resistance of the right electrode of sensor one (60.04 > 15.41). This however will be negligible compared to the resistance of the piezoresistive material, screen printed between the electrodes, which will be in the kilo-ohm range.

4.3.1.4 Conclusion

Using the NEBULA aerosol jet-based printer and the 3-axis g-code, we were able to produce functional silver electrodes. This is especially the case for the improved sensor design where the resistance stays below 60.04 Ω .

4.3.2 Screen printing of the piezoresistive material

The next step in producing the piezoresistive sensor circuit is screen printing the piezoresistive material between the sensor electrodes. This is done as explained in section 3.5.2. To discuss the different parts of the sensor circuit, enumeration is used as illustrated in Figure 4.9a. The final sensor configuration, which is produced with a hybrid manufacturing technique of AJP and screen printing, is illustrated in Figure 4.9b. An enlarged view of a single pressure sensor can be consulted in Figure 4.9c.

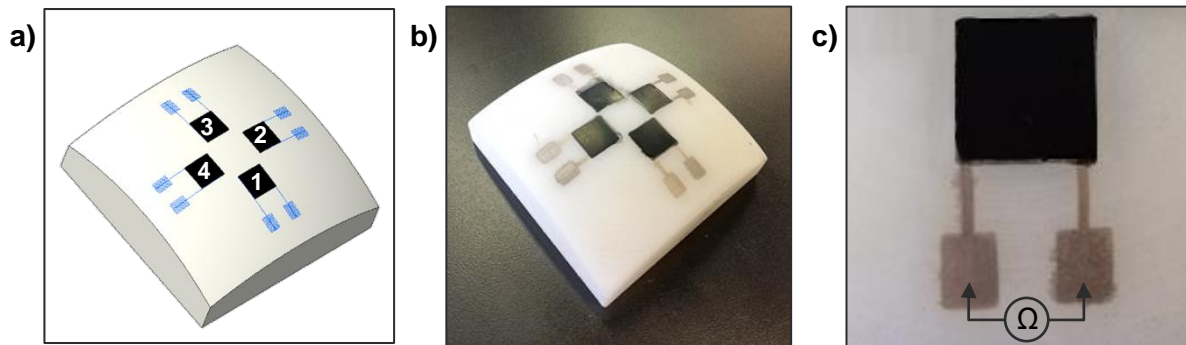


Figure 4.9: a) enumeration of sensors; b) sensor configuration printed on PA substrate; c) enlarged view of a single pressure sensor

Since the readout circuit has a maximal operating range of $40\text{k}\Omega$, the electrical resistance of the screen-printed ink must be kept below this value. The electrical resistance of each sensor circuit can be consulted in Table 4.5, according to the enumeration of Figure 4.9a. The electrical resistance is measured between the contact pads as illustrated in Figure 4.9c.

4.3.3 Coupling with the readout hardware

The final step is providing a coupling between the piezoresistive pressure sensor matrix and the readout hardware. This is done as explained in section 3.5.3. To discuss the different connections of the sensor circuit, enumeration is used as illustrated in Figure 4.10a. The final sensor configuration printed on the curved PA substrate, containing the output wires and pull relief, is illustrated in Figure 4.10b. To investigate the influence of the conductive epoxy adhesive on the conductivity of the sensors, the electrical resistance is measured between the output wires as illustrated in Figure 4.10c. The measured values are illustrated in Table 4.5.

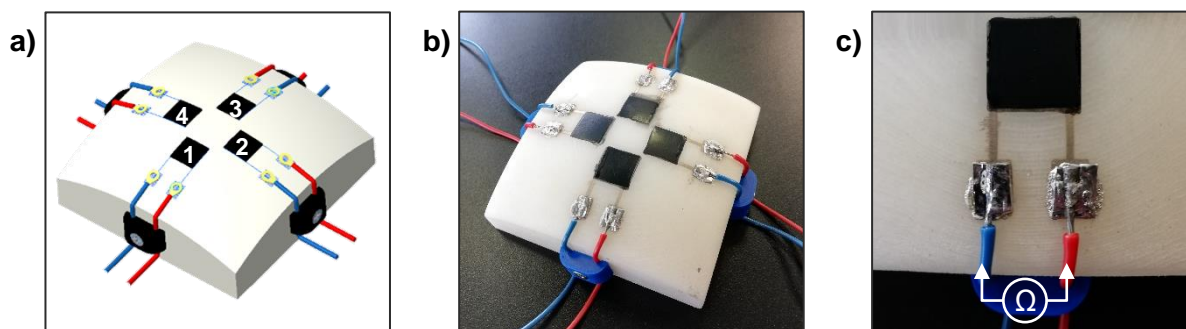


Figure 4.10: a) enumeration of sensors; b) sensor configuration with output wires; c) enlarged view of wire connection to contact pad

When looking at the results in Table 4.5, it is noteworthy that there are slight differences in electrical resistance ($R_{S1}=11,65k\Omega \leftrightarrow R_{S4}=4,94 k\Omega$) although the sensors were produced with the same batch of piezoresistive ink. According to the literature, this can be due to the fact that the number of conductive filler particles can vary slightly in the batch of prepared ink, resulting in slightly different characteristics. When looking at the results, we can conclude that the influence of the conductive epoxy adhesive, used to secure the output wires onto the contact pads, is negligible compared to the input resistance of the sensors.

4.3.4 Validation sensor circuit

In order to validate the functionality of the sensor matrix configuration, pressure testing of the piezoresistive pressure sensors is conducted. Since this is just to prove that the sensors are working, the sensor is actuated using a fingertip. Non-conductive latex gloves are worn to prevent influencing the measurement with the conductivity of the human skin. The results of these experiments are illustrated in Figure 4.11.

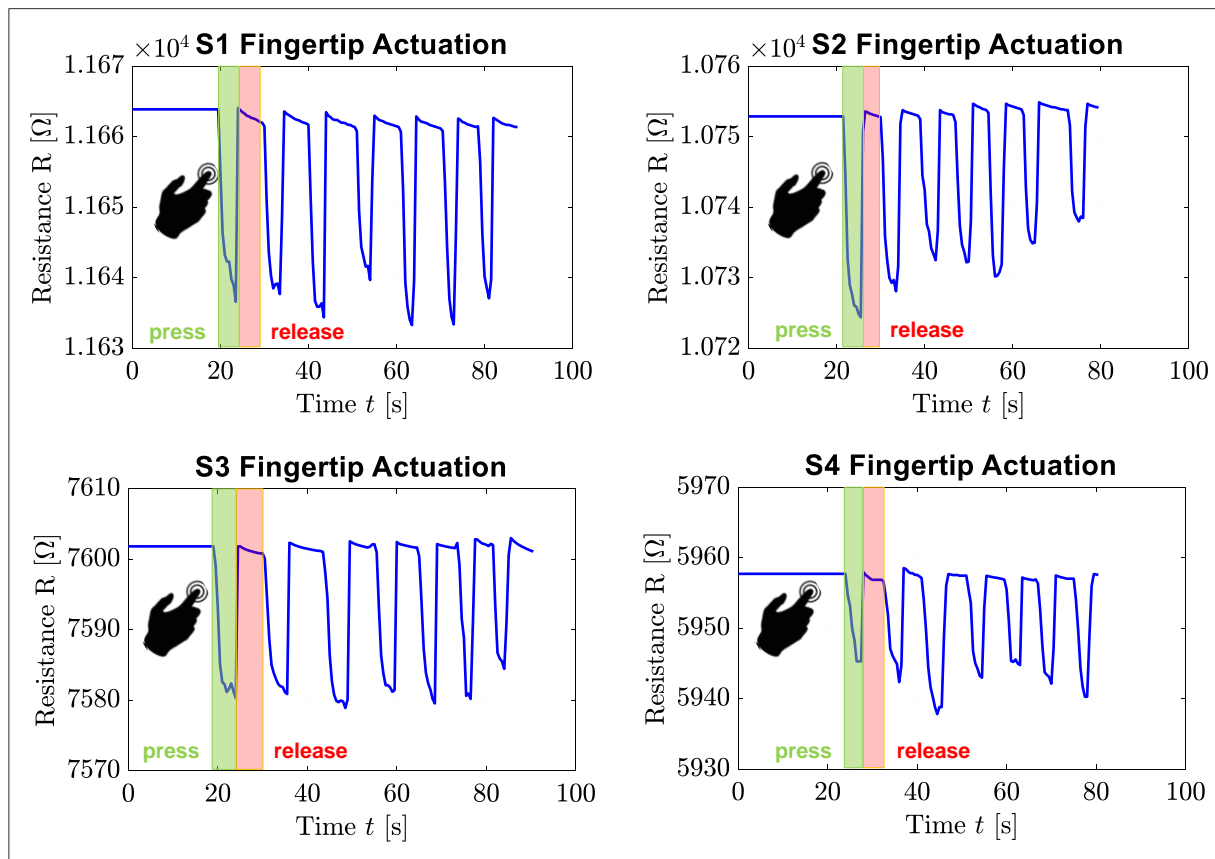


Figure 4.11: Cyclic fingertip actuation for each of the piezoresistive pressure sensors printed onto the curved PA substrate

As seen in Figure 4.11, all piezoresistive sensors start at a constant initial resistance. Applying pressure to the piezoresistive material results in a decrease in resistance. This is because when pressure is applied, the gap between the conductive particles in the polymer matrix decreases. This results in the formation of local conductive paths which are a result of the tunneling effect. This is the crossing of electrons between closely spaced nanomaterials, through the non-conductive barrier between them. When the piezoresistive material is decompressed, the elastic deformation is restored along with the value of electrical resistance.

As seen in Figure 4.11, the electrical resistance of each sensor approaches the initial resistance in the released state. In the compressed state however, there is a slight difference in the change of electrical resistance between multiple compressions. This is because the sensors are manually compressed, and the applied force differs slightly between compressions. The maximal recorded change along with the relative change in electrical resistance for each of the sensors is illustrated in Table 4.5.

Table 4.5: Electrical resistance of the sensor circuits

	S1	S2	S3	S4
Resistance between contact pads (kΩ)	11.65	10.76	7.61	5.94
Resistance between connection wires (kΩ)	11.63	10.75	7.60	5.94
Max change in electrical resistance (Ω)	30.50	28.50	22.92	19.89

When looking at the results in Table 4.5, we can see that the maximal change in electrical resistance seems to be higher when the initial resistance of the sensor is higher. For example, the maximal change in electrical resistance for the first sensor which has an initial resistance of 11.63kΩ is 30.50Ω, while the maximal change in electrical resistance for the fourth sensor which has an initial resistance of 5.94kΩ is 19.89Ω. However, note that the values of Table 4.5, which report about the change in electrical resistance, must be compared with caution because the exact applied pressure might differ for the different sensors.

4.3.4.1 Conclusion

By using the adapted screen-printing procedure and the developed coupling for the readout circuit, we were able to complete the piezoresistive pressure sensor matrix. A quick validation using fingertip actuation shows that the sensors are working as supposed.

5 VALIDATION 5-AXIS MOVEMENT NEBULA 5X-100s

This chapter describes the experiments that were conducted to evaluate the 5-axis movements of the NEBULA X-100S, for freeform sensor fabrication with practically no limitations on the curvature of the substrate.

The NEBULA printer is equipped with three translation axes (x,y,z) and two rotation axes (a,c), where the a-axis rotates around the x-axis and the c-axis rotates around the z-axis, as seen in Figure 5.1.

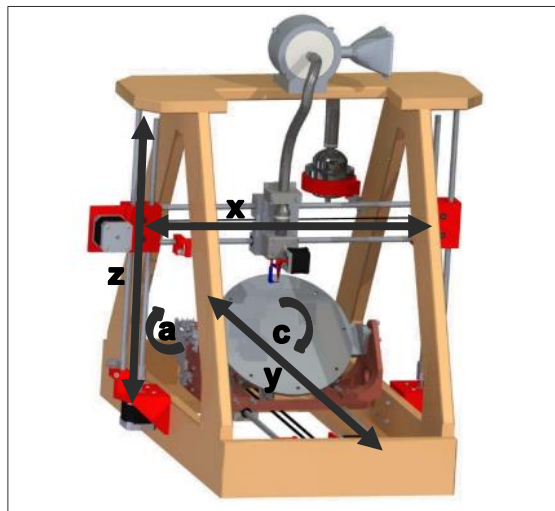


Figure 5.1: Axis annotation on the NEBULA 5X-100s

In previous work conducted by Deprince et al. [75], a postprocessor was written which converts PTC Creo CAM software toolpaths into specific NC control for Linux CNC. This postprocessor was written using the postprocessor tool “Option File Generator” in the Creo menu. The goal of this postprocessor was to enable simultaneous 5-axis deposition with the machine. However, when a simultaneous 5-axis program is executed, the desired result is not obtained. This can be caused by either the machine or the postprocessor. To investigate these events, both machine movements and postprocessor are assessed.

5.1 Experimental procedure and results of the machine movements

In this experiment, the machine movements are examined for each combination of controlled axes. This experiment is conducted because the machine can perform 3-axis linear movements but seems to struggle when a rotation is implemented. The goal is to determine if the machine can provide a correct translation and rotation of each axis for every given combination of simultaneously controlled axes.

To conduct this experiment, the printing nozzle is replaced by a text marker, as seen in Figure 5.2a, from which the writing point is at the same position as the printing nozzle. The center of the bed is determined by lowering the text marker at a random position to the print bed surface. The print bed is then rotated 360° to create a circle from which the center coincides with the center of the print bed. To determine the center of the circle, an enclosed rectangle is drawn

inside the circle from which the intersection of the diagonals marks the center of the bed. The center of the print bed will always be in the same spatial position, no matter the rotations. It will thus be used as a reference point to measure the translation of the text marker tip in x, y, and z-direction. We are now able to draw the x and y-axis through the center using the machine control. These will be used to measure the rotation around the c-axis of the machine and are illustrated in Figure 5.2b. A vertical reference line is drawn on the gear driving the a-axis to determine its position, as illustrated in Figure 5.2c. The translations and rotations are measured respectively with a caliper and angular ruler. This does not guaranty a highly precise measurement but enables us to see if the machine can make the combined movements.

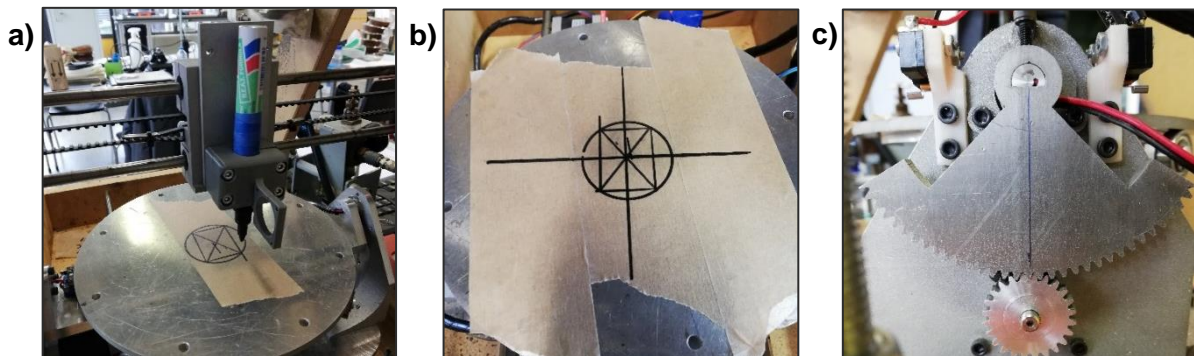


Figure 5.2: a) Nozzle replaced with text marker; b) determination of bed center; c) reference for rotation c-axis

All combinations of machine movements are examined to see whether the machine can perform the simultaneous 5-axis movements. The results of this experiment can be verified in "Appendix D: Experimental results. These results show that the machine can perform every combination of simultaneous movements without any problem. This leads to believe that the machine works fine, and further investigation of the postprocessor is required.

5.2 Investigation of the postprocessor

In this experiment, the simultaneous 5-axis g-code outputted by the postprocessor is examined more in detail. This experiment is conducted because the machine can perform 3-axis linear movements but seems to struggle when a rotation is implemented. The goal is to improve the postprocessor, so it provides the correct simultaneous 5-axis g-code to print the desired pattern.

First, the current postprocessor is examined. The latest version of the file was adjusted by Simen Stryckers under the name "uncx01.p04", and is used as a starting point. Using Creo CAM and the postprocessor, g-code for three basic lines as illustrated in Figure 5.3a is used to conduct the experiments. For the first line (L1) translation and rotation around xyza-axes are required. For the second and third lines (L2 and L3) translation and rotation around the xyzac-axes are required. The g-code will be tested on the machine where the printing nozzle is replaced by a text marker, as seen in Figure 5.3b, from which the writing point is at the same position as the printing nozzle. This way we can visualize what the machine is doing without spilling any ink. To save on PA substrates, PLA substrates are designed to be conformal to the shapes of the PA substrates and are used instead. The substrates are fixed to the bed with double-sided tape. To position the substrates according to the workpiece origin, reference lines

are drawn onto the build plate as seen in Figure 5.3c. The results of these experiments will then be used to make improvements to the postprocessor.

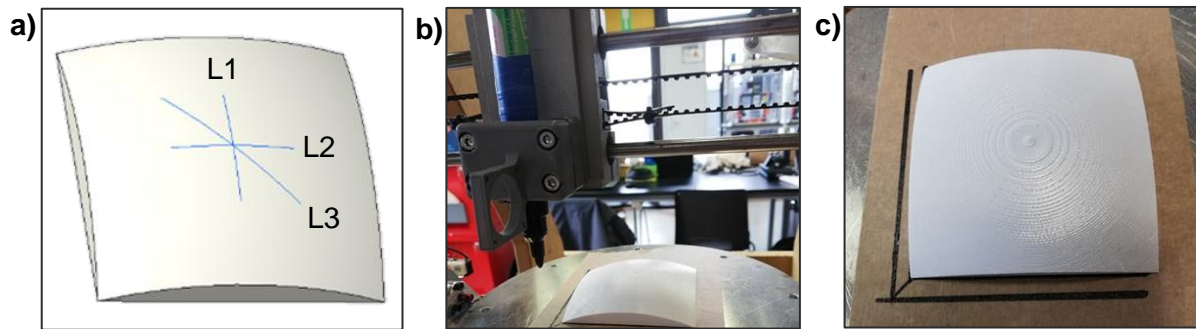


Figure 5.3: a) basic testing lines; b) nozzle replaced with text marker; c) substrate on bed

First, the functionality of the postprocessor for 3-axis movements is assessed. This is done by running the 3-axis g-code of the lines illustrated in Figure 5.4a. The results of this experiment are shown in Figure 5.4b, from which we can conclude that the postprocessor is able to create a proper 3-axis g-code. The g-code can be consulted in Appendix E: G-code.

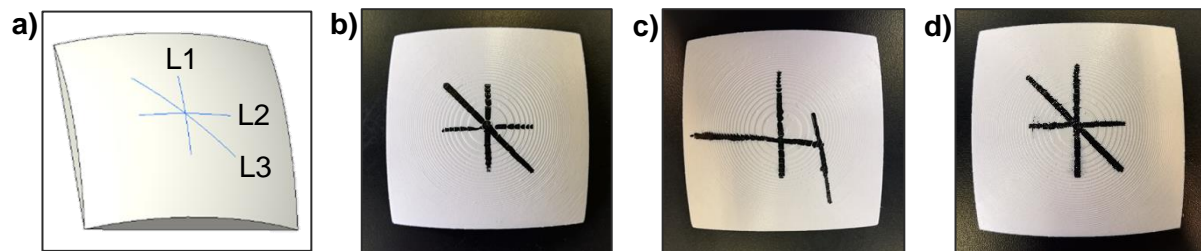


Figure 5.4: a) CAD line pattern; b) lines printed with 3-axis code; c) lines printed with 5-axis code; d) lines printed with 5 axis code rotations set to zero

Next, the functionality of the postprocessor for simultaneous 5-axis movements is assessed. This is done by running the 5-axis g-code of the lines illustrated in Figure 5.4a. The results of this experiment are shown in Figure 5.4c, from which we can conclude that the postprocessor is not able to produce a proper 5-axis g-code. This gives reason to take a critical look at the generated g-code, which can be consulted in Appendix E. The position of the lines is chosen in such a way that line 2 (L2) can be created with the g-code of line 1 (L1) when a rotation of -90° around the c-axis is implemented at the beginning of the code. A top view of L1 and L2 is visualized in Figure 5.5a. When the bed is rotated -90° around the c-axis, as visualized in Figure 5.5b, it is clear to see that L2 can be made with the same g-code as L1. When comparing the g-code of L1 with L2, we indeed notice a rotation of -90° around the c-axis at line 8 of the g-code, meaning that the rest of the g-code for L2 should be the same as for L1. When looking at the g-code we can see that this is not the case, which results in a toolpath that is different than the intended programmed line. This is due to the postprocessor which indeed rotates the c-axis -90° but does not take this rotation into account for the creation of the rest of the g-code, as illustrated in Figure 5.5c. The same applies to the g-code of L1 and L3.

A third experiment is conducted where a 5-axis g-code of the lines, as illustrated in Figure 5.4a, is created. To prove that the postprocessor does not take the rotations into account for the creation of the xyz-coordinates, rotations of the code are manually set to zero. The results of this manually adapted g-code are illustrated in Figure 5.4c, where we can see that the pattern

is properly made onto the substrate. Note that this however should not be the case because we took all the rotations out of a 5-axis g-code. From this, we can conduct that the postprocessor indeed does the rotations but does not take the rotations into account for the creation of the rest of the g-code.

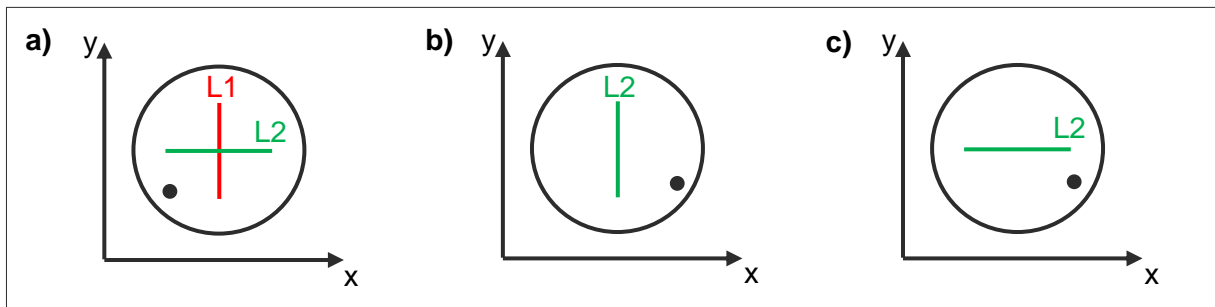


Figure 5.5: a) Original position of L1 and L2; b) Desired position of L2 after rotation 90°; c) Position of L2 allocated by the postprocessor after rotation 90°

5.3 Improvements postprocessor

Attempts were conducted to make the 5-axis postprocessor work but without any success. The postprocessor is made in “Creo option file generator” from which there is not much information or experience available. However, a small change is made to the initial sequence of the g-code. With the previous postprocessor, the g-code started with the tip of the nozzle at 10mm above the printing bed. To avoid tool crashes with the curved substrates, the initial distance to the bed is set at 30mm.

5.4 Conclusion

From these results, we can conclude that the NEBULA 5X-100s is able to perform simultaneous 5-axis movements. However, it is shown that the postprocessor is not able to produce an adequate 5-axis g-code. Attempts were made to get the postprocessor working but without any success. A proposal for future work is the creation of a new postprocessor in another program such as Siemens NX.

6 CONCLUSION AND FUTURE WORK

6.1 Conclusion

This research project concerned the characterization and implementation of piezoresistive pressure sensors on non-planar PA substrates. The pressure sensors are made using a combination of AJP and screen-printing techniques.

Piezoresistive pressure sensors were developed on flat PA substrate using the Optomec Aerosol Jet® Printer. To get a better understanding of the characteristics of the sensor, compression testing was conducted on the Instron 3367 mechanical testing system, where the change in resistance was measured in function of the applied pressure. Experiments were conducted to investigate the sensitivity, hysteresis, time-drift, and repeatability of the sensors. From the results of these experiments, we can conclude that the piezoresistive sensors have a mode of high sensitivity and low reliability ranging from 0 to 0.1MPa, where there also is a slight amount of hysteresis, opposed to a second mode with low sensitivity and high reliability which ranges from 0.1 to 1.25MPa. We can also conclude that the sensor size does not influence the sensitivity of the sensor and that the change in resistance decreases in function of both time and number of compression cycles.

Since the electrodes of the pressure sensor are produced using the NEBULA-5x100s aerosol jet-based printer, optimal process parameters were determined for the non-planar PA substrate. These experiments showed optimal conductivity of the printed lines when using a nozzle diameter of 0.84mm, a print speed of 50mm/min, an atomizer pressure of 1.5bar, a standoff distance of 1.5mm, 40 numbers of layers, a sintering temperature of 150°C, and a sintering time of 4h.

The sensor design was made using Creo Parametric and the g-code was extracted using a 3-axis postprocessor. The sensor electrodes were printed using the NEBULA-5X100s aerosol jet-based printer which was operated with the experimentally determined optimal printing parameters. The PA substrate was polished using 600 and 2400 grit paper and the ink was sintered at a temperature of 150°C for 4 hours. This resulted in nicely printed electrodes where a maximal resistance of only 60,04Ω was measured. The piezoresistive ink was screen printed between the sensor electrodes. To perform the screen printing onto the curved PA substrate, a patterned screen was used in combination with a squeegee, the edge of which had the same radius as the curved surface of the substrate. This resulted in an even distribution of the piezoresistive ink in the desired pattern. According to the data from the ink supplier and experiments conducted on the curved PA substrate, an optimal ink composition ratio of 60wt% CI-2050HR: 40wt% CI-2050LR was found. A coupling with the readout circuit was provided by attaching conductive copper wires onto the contact pads, using conductive epoxy adhesive. A pull relief was also provided to prevent tension from being applied directly onto the connection between the contact pads and the output wires. Finally, a validation of the piezoresistive sensor matrix was conducted by actuating the sensors using a fingertip. This showed a decrease in electrical resistance when the piezoresistive material between the electrodes is compressed, where a maximal change in resistance of 30.5Ω was recorded.

5-axis machine movement would be preferred to produce the sensor electrodes onto the non-planar PA substrate. The examination of the machine showed that when a simultaneous 5-

axis command was given directly into the command window, the machine was able to execute this without any problem. The examination of the postprocessor showed that it was not able to produce an adequate 5-axis g-code because it did not take the rotations into account for the creation of the xyz-coordinates. Attempts were made to get the postprocessor working but without any success in the remaining time.

Although, we can conclude that the final goal of this master thesis is achieved with the production of a functional piezoresistive pressure sensor configuration, printed onto a curved PA substrate using a hybrid of AJP and screen printing techniques. Not only does this bring us one step closer to the implementation of printed piezoresistive pressure sensors in medical devices, it also provides a new and innovative approach to the use of printed pressure sensors and opens up a whole new spectrum of applications.

6.2 Perspectives and future work

Further experimental testing can be conducted to get an even better understanding of the piezoresistive pressure sensor's characteristics. Proposed experiments are:

- UV-degradation testing.
- Temperature and humidity testing.

Since the NEBULA-5X100s is being continuously improved, some proposals for future improvements are:

- Overall improvement of the ink aerosolization and aerosol transport to the deposition nozzle. This also implies a reduction of expensive ink spillage. Currently, more ink is lost after cleanup inside the components than there is deposited onto the substrate.
- The addition of a functional shutter. This way one does not have to close the gas supply manually when printing non-connected features.
- The development of an adequate 5-axis postprocessor for the NEBULA-5X100s.

To improve the functionality of the piezoresistive pressure sensors, further experiments and implementations can be conducted:

- Further investigation of the piezoresistive ink composition on the piezoresistive properties of the sensor. This can be done by conducting an experiment where piezoresistive sensors are produced on flat substrates each having a different piezoresistive ink composition. Compression testing can be done to evaluate which ratio gives the highest change in electrical resistance.
- Further investigation on the influence of the thickness of the piezoresistive layer on the piezoresistive behavior of the pressure sensor.
- Providing a PDMS encapsulation to improve the biocompatibility of the sensors and establishing its influence on their piezoresistive properties.
- In the current design, the connection with the readout circuit is made through the contact pads which are located on the curved upper surface of the substrate. This restricts the compression possibilities to the area enclosed by the contact pads. By printing the contact pads to the side of the substrate, the entire upper surface can be compressed. This implies printing the electrodes over a 90° edge which is challenging but possible according to the literature.

LIST OF FIGURES

Figure 2.1: Classification of printing techniques for PE [1] [4]	4
Figure 2.2: Influencing parameters on the AJP process [30].....	7
Figure 2.3: Schematic illustration of the pneumatic Aerosol Jet printing process [42]	10
Figure 2.4: Schematic illustration of the ultrasonic atomizer [23]	11
Figure 2.5: Schematic illustration of the pneumatic atomizer [23]	11
Figure 2.6: Schematic illustration of the virtual impactor [31]	12
Figure 2.7: Schematic illustration of the deposition head with annular sheet gas [31].....	12
Figure 2.8: Effect of focusing ratio on (a) line width and (b) thickness for different nozzle sizes. [30].....	13
Figure 2.9: Effect of carrier gas flow on (a) line width and (b) thickness for different focusing ratios. [30]	13
Figure 2.10: Effect of stage speed on (a) line width and (b) thickness for different focusing ratios.[30]	14
Figure 2.11: Effect of (a) focusing ratio and (b) stage speed on resistance per length. [30]..	14
Figure 2.12: Overspray phenomenon, combination of [31] and [48].....	15
Figure 2.13: Ag line printed on a hydrophilic surface (left) and hydrophobic (right) surface [1]	16
Figure 2.14: Wetting angle of a droplet on substrate [52].....	16
Figure 2.15: Schematic illustration of the sintering process [52]	17
Figure 2.16: Schematic production process of TFT using AJP [9].....	19
Figure 2.17: Schematic illustration of the OLED structure [11].....	19
Figure 2.18: Schematic illustration of the solar cell structure [10]	19
Figure 2.19: Schematic diagram for the shell structure (a) and the effective (local) conductive path (b) of a nanocomposite [62]	21
Figure 2.20: Sandwich sensor structure (a) planar finger sensor structure (b) [59]	24
Figure 2.21: Sensor hysteresis Ramalingame et al. [59].....	25
Figure 2.22: Sensor hysteresis Valle-Lopera et al. [8]	25
Figure 2.23: Sensitivity of a piezoresistive sensor [59]	26
Figure 2.24: Cyclic test of a piezoresistive sensor [67]	26
Figure 2.25: Time drift testing at constant load [67]	27
Figure 2.26: Temperature and humidity drift testing [67].....	27
Figure 2.27: Silver lines printed over a 500 μ m trench [5].....	28

Figure 2.28: Antenna printed on curved substrate [6]	28
Figure 2.29: Serial printing patterns for the production of a heating element. Adjusted from [38]	28
Figure 2.30: 5-axis printing on ping pong ball [75]	28
Figure 3.1: Project flow and methodological approach	30
Figure 3.2: Arrangement of 6 piezoresistive pressure sensors printed on PA substrate, with a sensing area ranging from 100mm ² to 25mm ² , and label strategy	31
Figure 3.3 Experimental setup.....	33
Figure 3.4: Change in experimental setup a) first setup; b) second setup; c) third setup..	34
Figure 3.5: a) non-conductive tape and crocodile clamps; b) rubber patch on compression head; c) distribution of pressure through rubber patch.....	35
Figure 3.6: NEBULA 5X-100s Aerosol Jet based printer.....	36
Figure 3.7: Virtual impactor a) cross-section of the previous design; b) cross-section of the improved design; c) full view of the improved design.....	38
Figure 3.8: a) filter b) bracket atomizer	38
Figure 3.9: Substrates a) glass slides [website VWR]; b) flat PA substrate; c) curved PA substrate	40
Figure 3.10: a) 2D sensor sketch; b) projected sketch on curved substrate; c) complete sensor with piezoresistive material between electrodes	41
Figure 3.11: a) position of piezo-ink between electrodes; b) screen for printing; c) curved squeegee	42
Figure 3.12: a) Coupling readout hardware b) CAD pull relief c) Pull relief in assembly	43
Figure 4.1: Increasing load change in resistance in function of pressure	45
Figure 4.2: Hysteresis change in resistance in function of pressure.....	46
Figure 4.3: Time drift change in resistance at 125N in function of time	46
Figure 4.4: Cyclic force change in resistance in function of loading cycles	47
Figure 4.5: Silver lines printed on polished PA substrate after sintering.....	48
Figure 4.6: a) CAD sensor electrode design, b) pattern tested on PLA with text marker, c) pattern tested on PLA with AJP, d) sensor electrodes printed on PA substrate	49
Figure 4.7: a) improved sensor design b) sensor electrodes printed on curved PA substrate c) top view of electrodes with indications.....	50
Figure 4.8: a) sensor configuration design b) sensor electrode configuration printed on PA substrate c) indications for table	51
Figure 4.9: a) enumeration of sensors; b) sensor configuration printed on PA substrate; c) enlarged view of a single pressure sensor.....	52
Figure 4.10: a) enumeration of sensors; b) sensor configuration with output wires; c) enlarged view of wire connection to contact pad	52

Figure 4.11: Cyclic fingertip actuation for each of the piezoresistive pressure sensors printed onto the curved PA substrate53

Figure 5.1: Axis annotation on the NEBULA 5X-100s.....55

Figure 5.2: a) Nozzle replaced with text marker; b) determination of bed center; c) reference for rotation c-axis.....56

Figure 5.3: a) basic testing lines; b) nozzle replaced with text marker; c) substrate on bed 57

Figure 5.4: a) CAD line pattern; b) lines printed with 3-axis code; c) lines printed with 5-axis code; d) lines printed with 5 axis code rotations set to zero57

Figure 5.5: a) Original position of L1 and L2; b) Desired position of L2 after rotation 90°; c) Position of L2 allocated by the postprocessor after rotation 90°.....58

Figure 5.0.1: Virtual impactor a) before acetone treatment , b) after acetone treatment..... 1

Figure 5.0.2: a) raw resistance data, b) normalized resistance in function of pressure 5

LIST OF TABLES

Table 2.1: Market of printed electronics (values from [12], [13]).....	3
Table 2.2: Indirect printing techniques	4
Table 2.3: Direct printing techniques	5
Table 2.4: Comparison between the properties of Ink Jet and Aerosol Jet printing. [14][27][29]	6
Table 2.5: Commonly used AJP substrates and their characteristics.....	9
Table 2.6: Comparison between pneumatic and ultrasonic atomization [14][29].....	11
Table 2.7: Effect on line width, thickness, and resistance for independently increasing each of the process variables [31] (increase: ↑, decrease: ↓, no effect: -)	14
Table 2.8: Key sensor parameters.....	24
Table 3.1: Ink properties.....	32
Table 3.2: Printing parameters for Optomec 300 series.....	32
Table 3.3: Settings of the digital multimeter	34
Table 3.4: Conducted tests and testing conditions.....	35
Table 3.5: Nordson EFD precision tips	37
Table 3.6: Ink properties.....	39
Table 3.7: Process parameters for PA substrate	40
Table 4.1: Mean sensitivity and standard deviation for the two regions of sensitivity (low & high load).....	44
Table 4.2: Line width and conductivity on polished PA after sintering i.f.o. number of layers.	48
Table 4.3: Electrical resistance of different parts sensor electrodes.....	50
Table 4.4: Electrical resistance of different parts sensor configuration.....	51
Table 4.5: Electrical resistance of the sensor circuits	54

BIBLIOGRAPHY

- [1] S. Faraz Hasan, "Springer briefs in electrical and computer Engineering Emerging Trends in Communication Networks," 2014. [Online]. Available: <http://www.springer.com/series/10059>.
- [2] Y. Khan, A. Thielens, S. Muin, J. Ting, C. Baumbauer, and A. C. Arias, "A New Frontier of Printed Electronics: Flexible Hybrid Electronics," *Advanced Materials*, vol. 32, no. 15. Wiley-VCH Verlag, Apr. 01, 2020, doi: 10.1002/adma.201905279.
- [3] J. S. Chang, A. F. Facchetti, and R. Reuss, "A Circuits and Systems Perspective of Organic/Printed Electronics: Review, Challenges, and Contemporary and Emerging Design Approaches," *IEEE Journal on Emerging and Selected Topics in Circuits and Systems*, vol. 7, no. 1, pp. 7–26, Mar. 2017, doi: 10.1109/JETCAS.2017.2673863.
- [4] S. M. F. Cruz, L. A. Rocha, and J. C. Viana, "Printing Technologies on Flexible Substrates for Printed Electronics," in *Flexible Electronics*, InTech, 2018.
- [5] B. H. King and M. J. Renn, "Aerosol Jet® Direct Write Printing for Mil-Aero Electronic Applications," *Whitepaper - Optomec*, 2008.
- [6] M. Hedges and A. B. Marin, "3D Aerosol Jet® Printing - Adding Electronics Functionality to RP/RM," *Whitepaper - Optomec*, pp. 14–15, 2012.
- [7] S. J. Woo, J. H. Kong, D. G. Kim, and J. M. Kim, "A thin all-elastomeric capacitive pressure sensor array based on micro-contact printed elastic conductors," *Journal of Materials Chemistry C*, vol. 2, no. 22, pp. 4415–4422, Jun. 2014, doi: 10.1039/c4tc00392f.
- [8] D. A. Valle-Lopera, A. F. Castaño-Franco, J. Gallego-Londoño, and A. M. Hernández-Valdivieso, "Test and fabrication of piezoresistive sensors for contact pressure measurement," *Revista Facultad de Ingeniería*, vol. 2017, no. 82, pp. 47–52, 2017, doi: 10.17533/udea.redin.n82a06.
- [9] S. Lu *et al.*, "Flexible, Print-in-Place 1D-2D Thin-Film Transistors Using Aerosol Jet Printing," *ACS Nano*, vol. 13, no. 10, pp. 11263–11272, Oct. 2019, doi: 10.1021/acsnano.9b04337.
- [10] P. Kopola *et al.*, "Aerosol jet printed grid for ITO-free inverted organic solar cells," *Solar Energy Materials and Solar Cells*, vol. 107, pp. 252–258, Dec. 2012, doi: 10.1016/j.solmat.2012.06.042.
- [11] J. G. Tait *et al.*, "Uniform Aerosol Jet printed polymer lines with 30 μm width for 140 ppi resolution RGB organic light emitting diodes," *Organic Electronics*, vol. 22, pp. 40–43, Jul. 2015, doi: 10.1016/j.orgel.2015.03.034.
- [12] M. A. M. Leenen, V. Arning, H. Thiem, J. Steiger, and R. Anselmann, "Printable electronics: Flexibility for the future," *Physica Status Solidi (A) Applications and Materials Science*, vol. 206, no. 4, pp. 588–597, 2009, doi: 10.1002/pssa.200824428.
- [13] D. Raghu and P. Harrop, "RFID Forecasts , Players and Opportunities 2014-2024," *IDTechEX*, vol. i, no. October 2013, pp. 2009–2019, 2013.

- [14] A. Wadhwa, "Run-time Ink Stability in Pneumatic Aerosol Jet Printing Using a Split Stream Solvent Add Back System," p. 59, 2015, [Online]. Available: <https://scholarworks.rit.edu/theses>.
- [15] Z. Cui, "Printed Electronics: Materials, Technologies and Applications Zheng Cui," *MRS Bulletin*, vol. 42, no. 10, pp. 765–766, 2017, doi: 10.1557/mrs.2017.228.
- [16] H. Kipphan, *Handbook of print media: technologies and production methods*. New York: Springer, 2001.
- [17] X.-Y. Y. Fei Zhang, *Physical Chemistry of Gas-Liquid Interfaces*. Amsterdam: Elsevier, 2018.
- [18] Y. Xia and G. M. Whitesides, "Soft Lithography," *Angewandte Chemie International Edition*, vol. 37, no. 5, pp. 550–575, 1998, doi: 10.1002/(sici)1521-3773(19980316)37:5<550::aid-anie550>3.0.co;2-g.
- [19] J. Cai, C. Lv, and A. Watanabe, "Laser Direct Writing and Selective Metallization of Metallic Circuits for Integrated Wireless Devices," *ACS Applied Materials and Interfaces*, vol. 10, no. 1, pp. 915–924, Jan. 2018, doi: 10.1021/acsami.7b16558.
- [20] C. B. Arnold, P. Serra, and A. Piqué, "Laser Direct-Write Techniques for Printing of Complex Materials," *Mrs bulletin* •, vol. 32, 2007.
- [21] S. Gamerith, A. Klug, H. Scheiber, U. Scherf, E. Moderegger, and E. J. W. List, "Direct ink-jet printing of Ag-Cu nanoparticle and Ag-precursor based electrodes for OFET applications," *Advanced Functional Materials*, vol. 17, no. 16, pp. 3111–3118, Nov. 2007, doi: 10.1002/adfm.200600762.
- [22] N. J. Wilkinson, M. A. A. Smith, R. W. Kay, and R. A. Harris, "A review of aerosol jet printing—a non-traditional hybrid process for micro-manufacturing," *International Journal of Advanced Manufacturing Technology*, vol. 105, no. 11, pp. 4599–4619, Dec. 2019, doi: 10.1007/s00170-019-03438-2.
- [23] A. Mette, P. L. Richter, M. Hörteis, and S. W. Glunz, "Metal aerosol jet printing for solar cell metallization," *Progress in Photovoltaics: Research and Applications*, vol. 15, no. 7, pp. 621–627, Nov. 2007, doi: 10.1002/pip.759.
- [24] L. A. Baldwin *et al.*, "Synthesis of a Two-Component Carbosilane System for the Advanced Manufacturing of Polymer-Derived Ceramics," *Chemistry of Materials*, vol. 30, no. 21, pp. 7527–7534, Nov. 2018, doi: 10.1021/acs.chemmater.8b02541.
- [25] C. Yang, E. Zhou, S. Miyanishi, K. Hashimoto, and K. Tajima, "Preparation of active layers in polymer solar cells by aerosol jet printing," *ACS Applied Materials and Interfaces*, vol. 3, no. 10, pp. 4053–4058, Oct. 2011, doi: 10.1021/am200907k.
- [26] E. W. C. Phuah, W. L. Hart, H. Sumer, and P. R. Stoddart, "Patterning of biomaterials by aerosol jet printing: A parametric study," *Bioprinting*, vol. 18, Jun. 2020, doi: 10.1016/j.bprint.2020.e00081.
- [27] R. Salary *et al.*, "Computational Fluid Dynamics Modeling and Online Monitoring of Aerosol Jet Printing Process," *Journal of Manufacturing Science and Engineering, Transactions of the ASME*, vol. 139, no. 2, Feb. 2017, doi: 10.1115/1.4034591.

- [28] J. M. Hoey, A. Lutfurakhmanov, D. L. Schulz, and I. S. Akhatov, "A review on aerosol-based direct-write and its applications for microelectronics," *Journal of Nanotechnology*, 2012, doi: 10.1155/2012/324380.
- [29] T. Seifert, E. Sowade, F. Roscher, M. Wiemer, T. Gessner, and R. R. Baumann, "Additive manufacturing technologies compared: Morphology of deposits of silver ink using inkjet and aerosol jet printing," *Industrial and Engineering Chemistry Research*, vol. 54, no. 2, pp. 769–779, Jan. 2015, doi: 10.1021/ie503636c.
- [30] A. Mahajan, C. D. Frisbie, and L. F. Francis, "Optimization of aerosol jet printing for high-resolution, high-aspect ratio silver lines," *ACS Applied Materials and Interfaces*, vol. 5, no. 11, pp. 4856–4864, Jun. 2013, doi: 10.1021/am400606y.
- [31] N. J. Wilkinson, M. A. A. Smith, R. W. Kay, and R. A. Harris, "A review of aerosol jet printing—a non-traditional hybrid process for micro-manufacturing," *International Journal of Advanced Manufacturing Technology*, vol. 105, no. 11, pp. 4599–4619, Dec. 2019, doi: 10.1007/s00170-019-03438-2.
- [32] A. Kamyshny, J. Steinke, and S. Magdassi, "Metal-based Inkjet Inks for Printed Electronics," *The Open applied physics journal*, 2011.
- [33] S. Magdassi and A. Marmur, "Ink jet inks for silk printing," *Pigment & Resin Technology*, vol. 28, no. 6, pp. 3–52, 1999, doi: 10.1108/prt.1999.12928fad.011.
- [34] S. H. Kim, K. Hong, K. H. Lee, and C. D. Frisbie, "Performance and stability of aerosol-jet-printed electrolyte-gated transistors based on poly(3-hexylthiophene)," *ACS Applied Materials and Interfaces*, vol. 5, no. 14, pp. 6580–6585, Jul. 2013, doi: 10.1021/am401200y.
- [35] D. Alemu, H. Y. Wei, K. C. Ho, and C. W. Chu, "Highly conductive PEDOT:PSS electrode by simple film treatment with methanol for ITO-free polymer solar cells," *Energy and Environmental Science*, vol. 5, no. 11, pp. 9662–9671, Nov. 2012, doi: 10.1039/c2ee22595f.
- [36] Y. LI and B. S. ONG, "High mobility conjugated polymer semiconductors for organic thin film transistors," *Cosmos*, vol. 05, no. 01, pp. 59–77, May 2009, doi: 10.1142/s0219607709000427.
- [37] M. Hedges and A. B. Marin, "3D Aerosol Jet® Printing - Adding Electronics Functionality to RP/RM," *Whitepaper - Optomec*, pp. 14–15, 2012.
- [38] T. Blumenthal, V. Fratello, G. Nino, and K. Ritala, "Aerosol Jet® Printing onto 3D and Flexible Substrates," no. 253, [Online]. Available: www.Qi2.com%7C.
- [39] C. Cao, J. B. Andrews, and A. D. Franklin, "Completely Printed, Flexible, Stable, and Hysteresis-Free Carbon Nanotube Thin-Film Transistors via Aerosol Jet Printing," *Advanced Electronic Materials*, vol. 3, no. 5, pp. 1–10, 2017, doi: 10.1002/aelm.201700057.
- [40] Q. Jing, Y. S. Choi, M. Smith, C. Ou, T. Busolo, and S. Kar-Narayan, "Freestanding Functional Structures by Aerosol-Jet Printing for Stretchable Electronics and Sensing Applications," *Advanced Materials Technologies*, vol. 4, no. 7, 2019, doi: 10.1002/admt.201900048.

- [41] S. Agarwala *et al.*, “Wearable Bandage-Based Strain Sensor for Home Healthcare: Combining 3D Aerosol Jet Printing and Laser Sintering,” *ACS Sensors*, vol. 4, no. 1, pp. 218–226, 2019, doi: 10.1021/acssensors.8b01293.
- [42] F. Vogeler, W. Verheecke, A. Voet, and H. Valkenaers, “Aerosol Jet ® printed interconnections on extrusion based 3D printed substrates,” 2011.
- [43] M. S. Saleh, C. Hu, and R. Panat, “applied sciences and engineering Three-dimensional microarchitected materials and devices using nanoparticle assembly by pointwise spatial printing,” 2017. [Online]. Available: <http://advances.sciencemag.org/>.
- [44] M. Smith, Y. S. Choi, C. Boughey, and S. Kar-Narayan, “Controlling and assessing the quality of aerosol jet printed features for large area and flexible electronics,” *Flexible and Printed Electronics*, vol. 2, no. 1, Mar. 2017, doi: 10.1088/2058-8585/aa5af9.
- [45] W. Verheecke, M. van Dyck, F. Vogeler, A. Voet, and H. Valkenaers, “Optimizing Aerosol Jet® Printing of silver interconnects on polyimide film for embedded electronics applications,” in *Proceedings of the International Conference of DAAAM Baltic*, 2012, pp. 373–379.
- [46] G. Chen, Y. Gu, H. Tsang, D. R. Hines, and S. Das, “The Effect of Droplet Sizes on Overspray in Aerosol-Jet Printing,” *Advanced Engineering Materials*, vol. 20, no. 8, Aug. 2018, doi: 10.1002/adem.201701084.
- [47] E. B. Secor, “Principles of aerosol jet printing,” *Flexible and Printed Electronics*, vol. 3, no. 3, 2018, doi: 10.1088/2058-8585/aace28.
- [48] N. X. Williams, N. Watson, D. Y. Joh, A. Chilkoti, and A. D. Franklin, “Aerosol jet printing of biological inks by ultrasonic delivery,” *Biofabrication*, vol. 12, no. 2, 2020, doi: 10.1088/1758-5090/ab5cf5.
- [49] J. B. Lynch, P. D. Spence, D. E. Baker, and T. A. Postlethwaite, “Atmospheric Pressure Plasma Treatment of Polyethylene via a Pulse Dielectric Barrier Discharge: Comparison Using Various Gas Compositions Versus Corona Discharge in Air,” 1999.
- [50] V. di Virgilio, S. Bermejo, and L. Castañer, “Wettability increase by ‘corona’ ionization,” *Langmuir*, vol. 27, no. 15, pp. 9614–9620, Aug. 2011, doi: 10.1021/la2019583.
- [51] P. Ihalainen, A. Määttänen, J. Järnström, D. Tobjörk, R. Österbacka, and J. Peltonen, “Influence of surface properties of coated papers on printed electronics,” in *Industrial and Engineering Chemistry Research*, May 2012, vol. 51, no. 17, pp. 6025–6036, doi: 10.1021/ie202807v.
- [52] A. Roshanghias, M. Krivec, and M. Baumgart, “Sintering strategies for inkjet printed metallic traces in 3D printed electronics,” *Flexible and Printed Electronics*, vol. 2, no. 4, Dec. 2017, doi: 10.1088/2058-8585/aa8ed8.
- [53] K. Schuetz, J. Hoerber, and J. Franke, “Selective light sintering of Aerosol-Jet printed silver nanoparticle inks on polymer substrates,” in *AIP Conference Proceedings*, 2014, vol. 1593, pp. 732–735, doi: 10.1063/1.4873881.
- [54] J. Niittynen, R. Abbel, M. Mäntysalo, J. Perelaer, U. S. Schubert, and D. Lupo, “Alternative sintering methods compared to conventional thermal sintering for inkjet printed silver nanoparticle ink,” *Thin Solid Films*, vol. 556, pp. 452–459, Apr. 2014, doi: 10.1016/j.tsf.2014.02.001.

- [55] M. Zenou, O. Ermak, A. Saar, and Z. Kotler, "Laser sintering of copper nanoparticles," *Journal of Physics D: Applied Physics*, vol. 47, no. 2, Jan. 2014, doi: 10.1088/0022-3727/47/2/025501.
- [56] B. B. Narakathu *et al.*, "A novel fully printed and flexible capacitive pressure sensor," 2012, doi: 10.1109/ICSENS.2012.6411354.
- [57] B. Polzinger, J. Keck, V. Matic, W. Eberhardt, and H. Kück, "D4.1 - Inkjet and Aerosol Jet® Printed Sensors on 2D and 3D Substrates," pp. 566–569, 2020, doi: 10.5162/sensor2015/d4.1.
- [58] S. Rajala, M. Schouten, G. Krijnen, and S. Tuukkanen, "High Bending-Mode Sensitivity of Printed Piezoelectric Poly(vinylidene fluoride- co-trifluoroethylene) Sensors," *ACS Omega*, vol. 3, no. 7, pp. 8067–8073, 2018, doi: 10.1021/acsomega.8b01185.
- [59] R. Ramalingame *et al.*, "Flexible piezoresistive sensor matrix based on a carbon nanotube PDMS composite for dynamic pressure distribution measurement," *Journal of Sensors and Sensor Systems*, vol. 8, no. 1, pp. 1–7, 2019, doi: 10.5194/jsss-8-1-2019.
- [60] Z. Kappasov, J. Antonio Corrales Ramon, V. Perdereau, and J.-A. Corrales, "Tactile sensing in dexterous robot hands-Review," *Robotics and Autonomous Systems*, vol. 74, pp. 195–220, 2015, doi: 10.1016/j.robot.2015.07.015.
- [61] M. Amjadi, K. U. Kyung, I. Park, and M. Sitti, "Stretchable, Skin-Mountable, and Wearable Strain Sensors and Their Potential Applications: A Review," *Advanced Functional Materials*, vol. 26, no. 11. Wiley-VCH Verlag, pp. 1678–1698, Mar. 15, 2016, doi: 10.1002/adfm.201504755.
- [62] L. Wang, T. Ding, and P. Wang, "Thin flexible pressure sensor array based on carbon black/silicone rubber nanocomposite," *IEEE Sensors Journal*, vol. 9, no. 9, pp. 1130–1135, Sep. 2009, doi: 10.1109/JSEN.2009.2026467.
- [63] X. W. Zhang, Y. Pan, Q. Zheng, and X. S. Yi, "Time dependence of piezoresistance for the conductor-filled polymer composites," *Journal of Polymer Science, Part B: Polymer Physics*, vol. 38, no. 21, pp. 2739–2749, 2000, doi: 10.1002/1099-0488(20001101)38:21<2739::AID-POLB40>3.0.CO;2-O.
- [64] M. Kalantari, J. Dargahi, J. Kövecses, M. G. Mardasi, and S. Nouri, "A new approach for modeling piezoresistive force sensors based on semiconductive polymer composites," *IEEE/ASME Transactions on Mechatronics*, vol. 17, no. 3, pp. 572–581, 2012, doi: 10.1109/TMECH.2011.2108664.
- [65] S. S. Kumar and B. D. Pant, "Design principles and considerations for the 'ideal' silicon piezoresistive pressure sensor: A focused review," *Microsystem Technologies*, vol. 20, no. 7, pp. 1213–1247, 2014, doi: 10.1007/s00542-014-2215-7.
- [66] S. Wu, "Phase structure and adhesion in polymer blends: A criterion for rubber toughening," *Polymer*, vol. 26, no. 12, pp. 1855–1863, 1985, doi: 10.1016/0032-3861(85)90015-1.
- [67] J. Ahmad, H. Andersson, and J. Sidén, "Screen-Printed Piezoresistive Sensors for Monitoring Pressure Distribution in Wheelchair," *IEEE Sensors Journal*, vol. 19, no. 6, pp. 2055–2063, Mar. 2019, doi: 10.1109/JSEN.2018.2885638.

- [68] M. Hedges and A. B. Marin, "3D Aerosol Jet® Printing - Adding Electronics Functionality to RP/RM," *WHITEPAPER - Optomec*, pp. 14–15, 2012.
- [69] S. I. Yaniger, "Force Sensing resistors™ a review of the technology," in *Electro International, ELECTR 1991 - Conference Record*, 1991, pp. 666–668, doi: 10.1109/ELECTR.1991.718294.
- [70] S. Khan, W. Dang, L. Lorenzelli, and R. Dahiya, "Flexible Pressure Sensors Based on Screen-Printed P(VDF-TrFE) and P(VDF-TrFE)/MWCNTs," *IEEE Transactions on Semiconductor Manufacturing*, vol. 28, no. 4, pp. 486–493, 2015, doi: 10.1109/TSM.2015.2468053.
- [71] J. S. Kim and G. W. Kim, "Hysteresis compensation of piezoresistive carbon nanotube/polydimethylsiloxane composite-based force sensors," *Sensors (Switzerland)*, vol. 17, no. 2, Jan. 2017, doi: 10.3390/s17020229.
- [72] H. Montazerian, A. Dalili, A. S. Milani, and M. Hoorfar, "Piezoresistive sensing in chopped carbon fiber embedded PDMS yarns," *Composites Part B: Engineering*, vol. 164, no. March 2018, pp. 648–658, 2019, doi: 10.1016/j.compositesb.2019.01.090.
- [73] S. LLC., "FSR 101 Force Sensing Resistor Theory and Applications," pp. 1–15, 2017.
- [74] J. A. Paulsen, M. Renn, K. Christenson, and R. Plourde, "Printing conformal electronics on 3D structures with aerosol jet technology," *FIIW 2012 - 2012 Future of Instrumentation International Workshop Proceedings*, pp. 47–50, 2012, doi: 10.1109/FIIW.2012.6378343.
- [75] S. Peeters and T. Deprince, "Optimalisatie en validatie van een own-built aerosol gebaseerde printer," 2017.

APPENDIX

Appendix A: Procedures

Appendix B: Technical drawings

Appendix C: Matlab scripts

Appendix D: Experimental results

Appendix E: Datasheets

APPENDIX A: PROCEDURES

1. Procedure acetone smoothing

This procedure was carried out to perform the acetone smoothing on both parts of the virtual impactor.

File preparation & production:

- 1) A .stl file is produced of the top and bottom parts.
- 2) This file is uploaded to the Prusa slicer. Since we will melt some of the outer layers of the part with acetone, it is important that the part always keeps its structural integrity. Therefore, the outer wall count is increased to 5 layers.
- 3) Since there is quite some overhang in the part, support features are needed to ensure proper production. To make sure there is no sagging of the filament when bridging, the offset value between the support and the first layer printed on this support is set to zero.
- 4) The file is then uploaded to the Prusa i3 MK3S. Since ABS has the tendency to warp of the bed, bed adhesion is improved by spraying the bed with hair spray. An improvised enclosure is also built around the machine to prevent convection cooling.

Post-processing & acetone treatment:

- 5) First, the support features are removed from the printed part. This is quite difficult since they were printed with zero offset between the support and the first layer.
- 6) Next, the surface is treaded using acetone. This was done by applying acetone to the surface using a sponge.
- 7) After 15min the outer layer of the part was fully cured. Figure 5.1 gives an illustration of the part before (a) and after (b) acetone treatment.

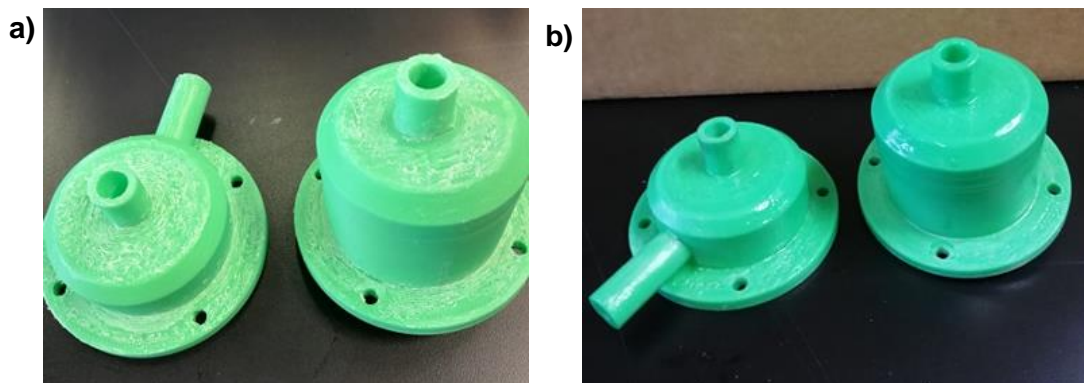


Figure 5.0.1: Virtual impactor a) before acetone treatment , b) after acetone treatment

2. Screen printing procedure

This procedure must be carried out to ensure a consistent screen print quality. During this procedure, when coming in contact with the ink, one must always wear a lab coat and rubber gloves.

Preparation:

- 1) Calculate the amount of both ink components that need to be weighed to obtain a certain mixing ratio. An optimal ratio of 60wt% CI-2050HR: 40wt% CI-2050LR was found. This corresponds to a ratio of 3g CI-2050HR to 2g CI-2050LR.
- 2) A disposable plastic cup and spoons are gathered and positioned at the weighing scale. Some paper towel is placed on the working table to avoid spillage of the ink.
- 3) The printing screen is positioned at a table along with a stool to ensure an ergonomic working stance. A Paper towel is placed at the side to dispose the contaminated components after usage.

Weighing and mixing:

- 4) The two ink components, CI-2050HR and CI-2050LR, are taken from the fridge where they are kept at 4°C.
- 5) The disposable plastic cup is placed onto the weighing scale and the weight is tared to zero. Both ink components are added according to the ratios, as discussed in point 2, using the plastic spoons.
- 6) After weighing, both ink components are placed back in the fridge and the plastic spoons are cleaned using isopropanol and a paper towel.
- 7) A clean plastic spoon is used to mix the two ink components. This is done by stirring the two components in a random pattern for three minutes.

Screen printing:

- 8) Somme mixed ink is deposited on the screen using the plastic spoons. Afterward, the spoons are deposited onto the provided paper towel.
- 9) The curved PA substrate is positioned beneath the 10x10mm pattern on the screen. The piezoresistive ink is pushed through the screen onto the substrate using the squeegee which has the same curvature as the substrate.
- 10) Five printing passes are performed using the squeegee, where the direction of travel is maintained during the different passes.
- 11) The substrate on which has been printed is placed in an oven at 150°C for 1h. This will cure the ink and improve its piezoresistive properties.
- 12) The screen and plastic spoons are cleaned using methylethylketone. The disposable plastic cup, which contains the remains of the ink, is put inside a rubber glove which is knotted before throwing it into the bin.

3. Procedure connection readout

This procedure discusses the steps that must be taken to establish the connection between the piezoresistive position sensors and the readout circuit.

Pull relief:

- 1) The pull reliefs are printed using Fused Filament Fabrication on a Prusa i3 MK3S, according to the provided design.
- 2) To attach the pull reliefs, holes are drilled into the sides of the substrate. First, the position of the hole is measured and indicated. Next, the substrate is positioned into a vise to simplify the drilling of the holes. The drill used to drill the holes has a diameter equal to the core diameter of the screw.

Wire preparation:

- 3) The wires, both positive and negative, are cut to the desired length of the user.
- 4) Solder pads are created by dropping some hot solder onto a cold stone working bench. The solder pads are then cut into the desired shape.
- 5) The ends of the wires are stripped from their insulation and one of the ends is soldered to a solder pad. This creates a large flat area at the end of the wires which will improve the connection of the wire to the contact pad of the sensor.

Conductive epoxy adhesive:

- 6) A disposable plastic cup is gathered along with some paper towel to avoid spillage of the ink.
- 7) The conductive epoxy adhesive consists of two components which are mixed at a 1 to 1 volume ratio. The two components (Bis-F Epoxy Resin Metallic Silver and Aliphatic Amines Metallic Silver) are deposited into the plastic cup using the syringes in which they are delivered. The scale onto the syringes is used to assess the deposited quantity.
- 8) A clean plastic spoon is used to mix the two ink components. This is done by stirring the two components in a random pattern for three minutes.

Assembly:

- 9) Some conductive epoxy adhesive is deposited onto the contact pads of the sensor configuration. Next, the ends of the wires which are equipped with flat solder pads are placed on top of the epoxy adhesive.
- 10) The solder pads are pressed to evenly distribute the conductive epoxy adhesive between the sensor pad and the solder pad.
- 11) The pads are then taped to the substrate to secure them while curing.
- 12) The conductive epoxy adhesive is cured at room temperature for 5 hours.
- 13) The conductive output wires which are now connected to the sensors are clamped into place using the pull relief. This is done by tightening the screws while the wires are put in the right place.
- 13) The plastic spoon is cleaned using methylethylketone. The disposable plastic cup, which contains the remains of the conductive epoxy adhesive, is put inside a rubber glove which is knotted before throwing it into the bin.

4. Procedure resistance measurement

The following procedure can be followed to perform the resistance measurement of the compression testing experiments using the Rigol DM3068 digital multimeter.

Performing experiment:

- 1) Plug in the digital multimeter and flick the power switch to the on state.
- 2) Insert the adapters of the positive and negative measuring probes in the provided sockets. (a 2-wire measuring method is used)
- 3) Set measurement type to RESISTANCE, set range to AUTO RANGE, set sampling frequency to 2Hz.
- 4) Insert a removable drive into the USB slot of the machine.
- 5) Attach the measurement probes to the contact pads of the sensors.
- 6) Perform the experiment.

Saving data on removable drive:

- 7) Push the HISTORY button.
- 8) Push the SAVE button.
- 9) Select the removable drive using the most left control button.
- 10) Select the data type MEAS_CSV using the second from the left control button.
- 11) Push the SAVE button.
- 12) Name the file using the control buttons.
- 13) Push the DONE button to save the data.
- 14) Push the RETURN button to return to the main screen.
- 15) The removable drive can now be removed from the Rigol DM3068 digital multimeter.

Data in excel:

- 16) Open the ".csv" file.
- 17) Save a copy of the ".csv" file as ".excel" file. Saving the data as ".csv" file results in a loss of resolution of the measured data which must be avoided.
- 18) To separate the sampling rate from the measurement data: select column A > text to columns > separated > separate by comma > complete.
- 19) To change the "." entity to ",": select the column containing the resistance values > search and select > replace > (to replace: ".", replaced by: ",") > replace everything.

5. Procedure data processing

The following procedure describes how the data is processed using the Matlab script. The steps will be described in chronologic order.

a) Loading the data

First, the experimental data is loaded into Matlab. This can be done using the following Matlab script:

```
%% load the data-----  
data = load('F.txt'); %force  
  
data11 = load('1.1.txt'); %resistance  
data12 = load('1.2.txt'); %resistance  
data13 = load('1.3.txt'); %resistance  
%-----
```

Note that only the measurements of the first sensor of board one are loaded. This will be sufficient to explain how the data processing works.

b) Calculating pressure

Next, the force data file is processed. The data file consists of two columns, where the first column contains the sampling time and the second the force measurement. Since the applied force was in the compression state, it is recorded with a negative sign. To make it easier to work, the applied force is made positive. Since we are interested in the applied pressure, the force is converted to pressure using the compressed area. This can be done using the following Matlab code:

```
%% prepare the pressure -----  
t = data(:,1); % first column  
y = -data(:,2); % second column  
y = y/(0.01*0.01) % force to pressure  
my = max(y) % max pressure  
%-----
```

c) Calculating resistance

Next, the resistance data file is processed. The data file consists of two columns, where the first column contains the sampling time and the second the resistance measurement. Plotting the resistance in function of the sampling time results in Figure 5.0.2a.

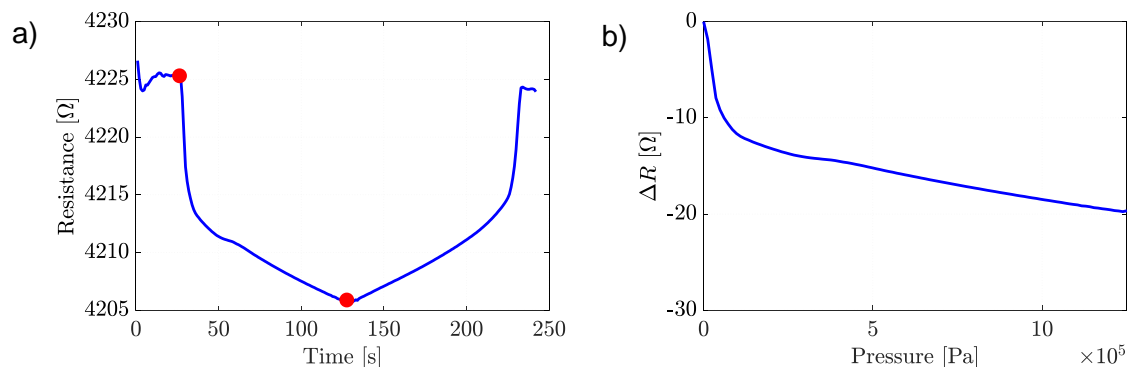


Figure 5.0.2: a) raw resistance data, b) normalized resistance in function of pressure

Using the zoom and data inspect function in the graph window, we can now determine the lower and upper boundary of the valid measurement (between red dots). This valid range of measurements is put into an id function, which is then used to extract the useful data from the data file.

Since the sampling rate from the Instron tensile setup (50Hz) is higher than the sampling rate of the Rigol DM (2Hz), there are a lot more data points of the pressure than there are of the resistance. In order to plot resistance in function of pressure, two datasets of the same length are required. The “linespace” command is used to reduce the amount of pressure data points, so the pressure dataset has the same length as the resistance data set.

Next, the resistance dataset is zero set by subtracting the maximal resistance (=initial resistance) of the entire dataset. Plotting the zero set resistance in function of the applied pressure then gives Figure 5.0.2b.

All this can be done by using the following Matlab code:

```

%% data11 preparation -----
x11 = data11(:,1); % first column
y11 = data11(:,2); % second column

figure,plot(x11,y11) % plot figure visual determination upper and lower boundary

id = find(x11>=9 & x11<=112);
y11 = y11(id); % correct resistance
P11 = linspace(0,my, size(y11,1));
y11 = (y11 - max(y11)); %normalisation of data

figure,plot(P11,y11)
%-----

```

This is done in a similar way for data12 and data13 which are the second and third measurements of sensor one.

d) Mean and standard deviation

To combine the three measurements and obtain a reliable dataset, the mean and standard deviation are calculated for the three measurements. This can be done by using the following Matlab code:

```

%% Mean and standard deviation -----
Y1 = [y11,y12,y13];
M1 = mean(Y1,2);
S1 = std(Y1,0,2);
%-----

```

e) Plotting and visual effects

Once we have obtained all the useful data, this data can be combined into a final graph. First, some overall figure settings can be defined using the following Matlab code:

```

%% plotting and the visual effects-----
% overall figure settings -----
figure1 = figure, hold all %all on one figure
set(figure1, 'position',[100,100, 650, 450])%define figure location and size

hh = set(gca, 'FontSize',20, 'ticklabelinterpreter','latex',...
    'gridlinestyle',':','xaxislocation','bottom','gridcolor',0.6*[1 1 1],...
    'minorgridlinestyle','none');]

```



```
box on, grid on, hold on;
```

```
%-----
```

Next, the mean resistance and standard variation can be plotted. The standard variation is visualized using the “patch” command. In order to use this command, the upper and lower limit of the patch are determined by respectively $(M1+S1)$ and $(M1-S1)$.

```
% plotting mean resistance and std -----
```

```
R1 = plot(P11,M1, '-','linewidth',2.5,'color','b') % plot resistance
```

```
X1 = [P11, fliplr(P11)]; %pressure dataset (0 - max - 0)
```

```
Y1_lower = M1'-S1'; %determining lower boundary standard deviation
```

```
Y1_upper = M1'+S1'; %determining upper boundary standard deviation
```

```
Y1 = [Y1_lower, fliplr(Y1_upper)]; % Std dataset (lower - end - upper)
```

```
P1 = patch(X1,Y1,'b','facealpha',0.25,'linestyle','none');
```

```
%-----
```

Next the labels and legend are added to the graph. This is done using the following Matlab code:

```
% labels -----
```

```
ylbl = ylabel('$\Delta R\$\ [\$\Omega\$]','Color',[0 0 0]);
```

```
set(ylbl,'fontsize',20,'interpreter','latex','color',[0 0 0])
```

```
set(gca,'ylim',[-30, 0])
```

```
set(gca,'ycolor',[0 0 0])
```

```
xlabel('Pressure [Pa]'); set(xlbl,'fontsize',20,'interpreter','latex')
```

```
set(gca, 'xlim',[0,my])
```

```
legend
```

```
leg = legend([R1], 'R1$\pm$std');
```

```
set(leg,'fontsize',13,'interpreter','latex')
```

```
%-----
```

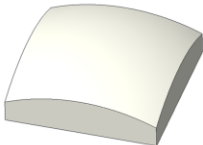
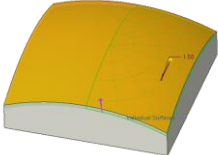
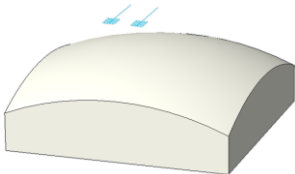
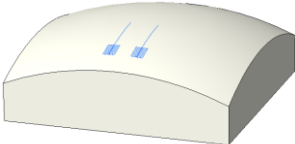
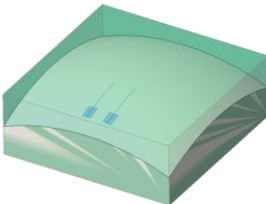
Note that this procedure only describes how to process the data of the first sensor of board1. To process all data, the code is expanded while maintaining the same strategy.

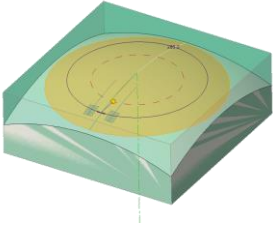
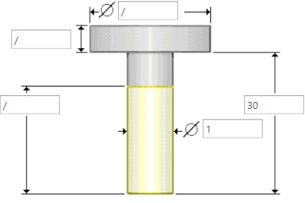
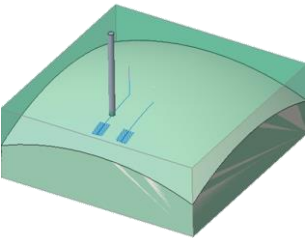
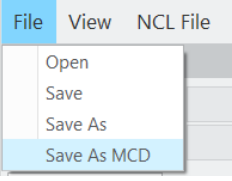
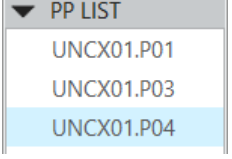
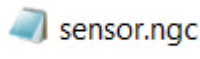
6. Step-by-step sensor design plan

A detailed explanation of how to create the sensor design and extract the g-code is given in Tabel 5.0.1. The process consists of three main parts:

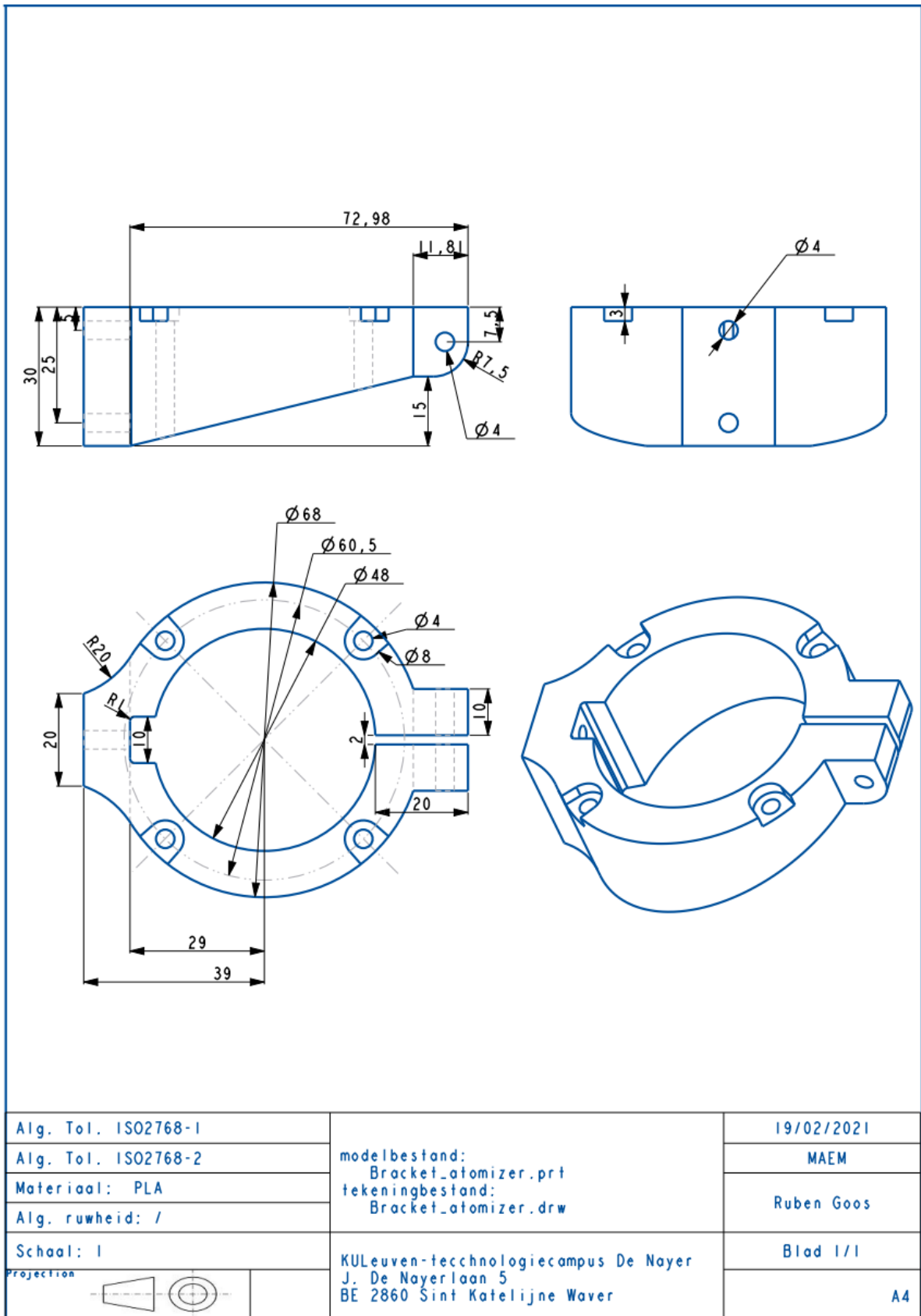
- Generating sensor design (CAD)
- Generating toolpaths (CAM)
- extracting g-code and postprocessing

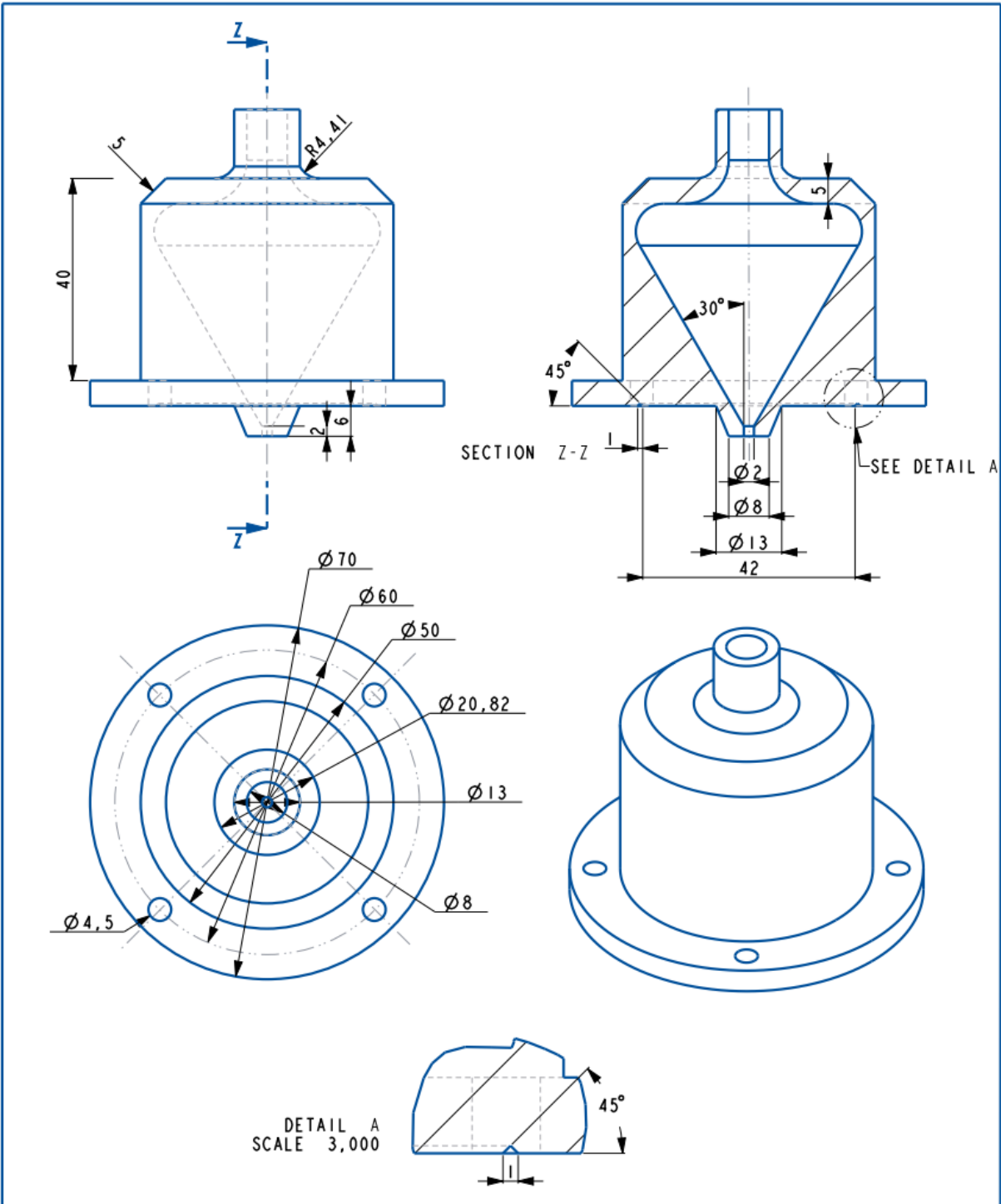
Tabel 5.0.1: Generating sensor design and g-code

Sensor design (CAD)		
Step	Image	Explanation
1.1		<ul style="list-style-type: none"> • Creation of a solid part CAD model of the substrate. • The substrate model will be used as a base for the sensor design.
1.2		<ul style="list-style-type: none"> • Offsetting the substrate geometry. • The offset value will act as the standoff distance between the workpiece and deposition nozzle. • The offset feature is found in the flexible modeling tab.
1.3		<ul style="list-style-type: none"> • A two-dimensional representation of the sensor design is made on a sketching plane that floats above the curved surface of the substrate and is perpendicular to the z-direction.
1.4		<ul style="list-style-type: none"> • The two-dimensional representation of the sensor design is then projected onto the curved surface of the substrate. • The projection feature is found in the editing tab.
Generating toolpaths (CAM)		
Step	Image	Explanation
2.1		<ul style="list-style-type: none"> • The previously made sensor design on the substrate is placed into the CAM environment in the default position. • A raw workpiece must be defined to continue with the 'milling' operations. • A workpiece origin is defined according to which the operations will be executed.

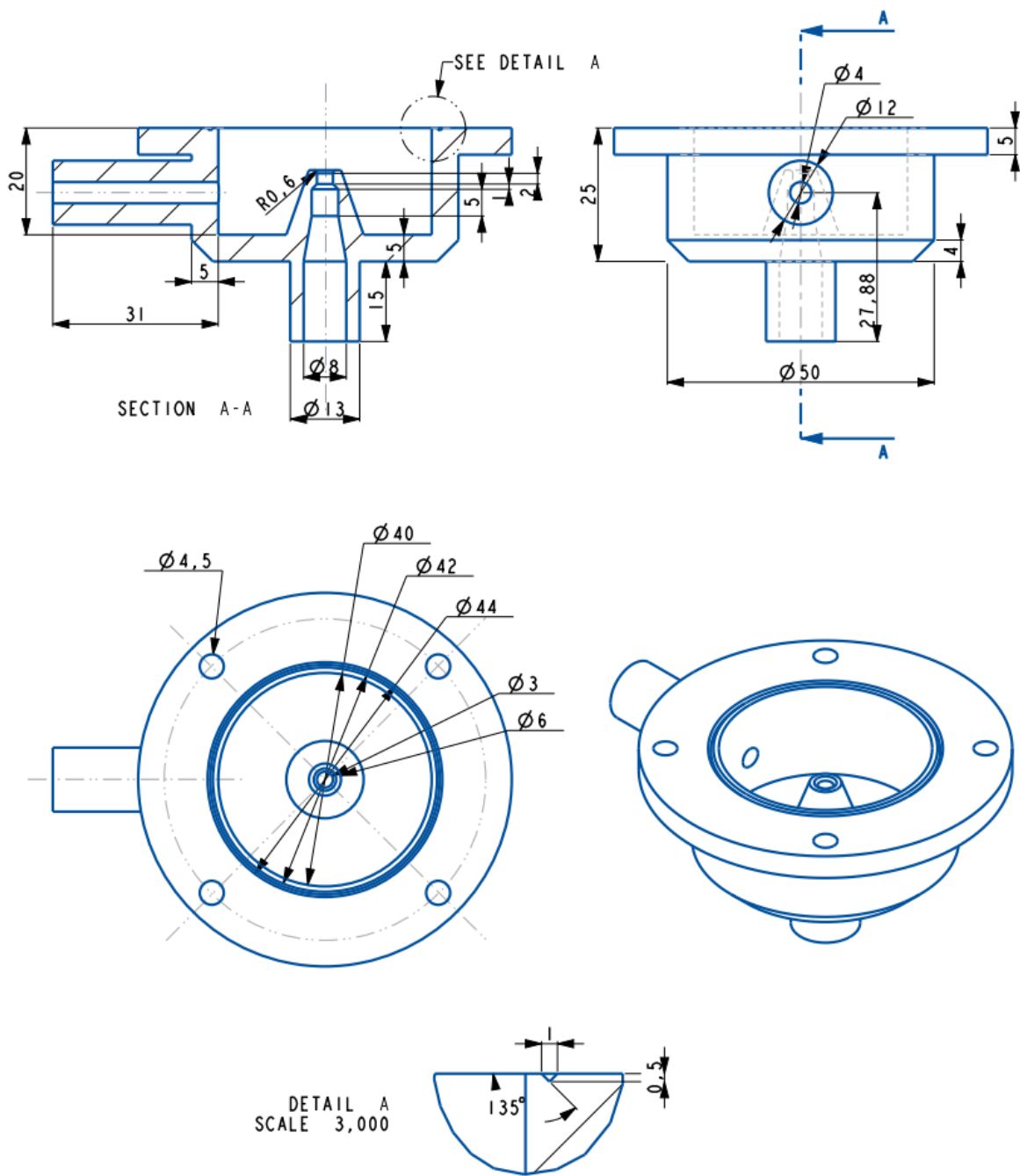
2.2		<ul style="list-style-type: none"> • A milling surface is generated which will be used as a reference surface for the 3 or 5-axis milling. • The milling surface coincides with the surface of the substrate. • The milling surface can also be used to control if the sensor design lies between the rotational degrees of the A-axis of the NEBULA 5X-100s (=45°)
2.3		<ul style="list-style-type: none"> • Define a 3 or 5-axis machine work center. • Create a new milling operation with the origin made in step 2.1 as reference. • Define a tool with the following properties: <ul style="list-style-type: none"> ▪ Type: end mill ▪ Diameter: 1mm ▪ Cutout length: 30mm (= nozzle length)
2.4		<ul style="list-style-type: none"> • Make an engraving operation where the tool defined in 2.3 follows the projected sketch of 1.4. • When creating 5-axis toolpaths, select the milling surface from 2.2 as a normal surface for the tool. This way the machine will operate the 5 axes, so the tool (nozzle in our case) is always directed normally to the substrate surface. • Define the following parameters: <ul style="list-style-type: none"> ▪ Cut feed: 50mm/min (= printing speed)
Extracting g-code and post-processing		
Step	Image	Explanation
3.1		<ul style="list-style-type: none"> • Use the sequence: play path > file > save as MCD > output, to generate the g-code. • Select the location to store the g-code file in.
3.2		<ul style="list-style-type: none"> • Select the postprocessor for the NEBULA 5X-100s from the list. • The name of the postprocessor file is: UNCX01.P04
3.3		<ul style="list-style-type: none"> • The g-code is now post-processed and saved in the location defined in step 3.3.

APPENDIX B: TECHNICAL DRAWINGS

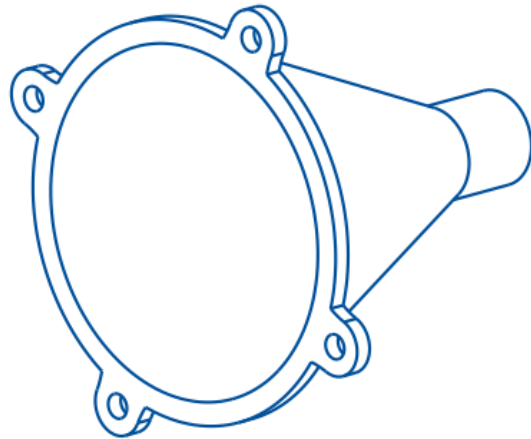
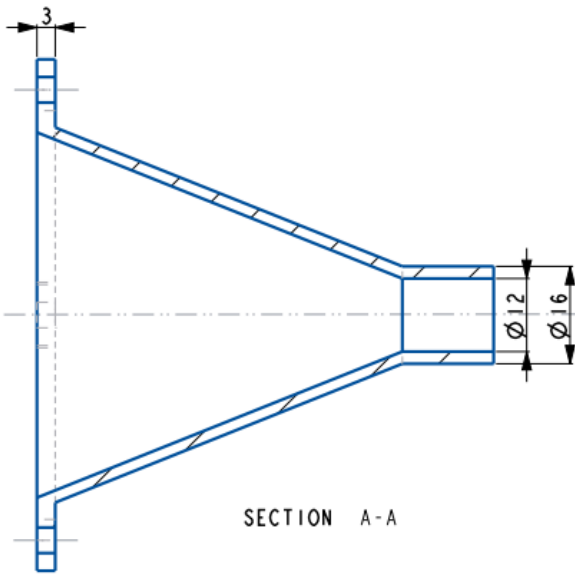
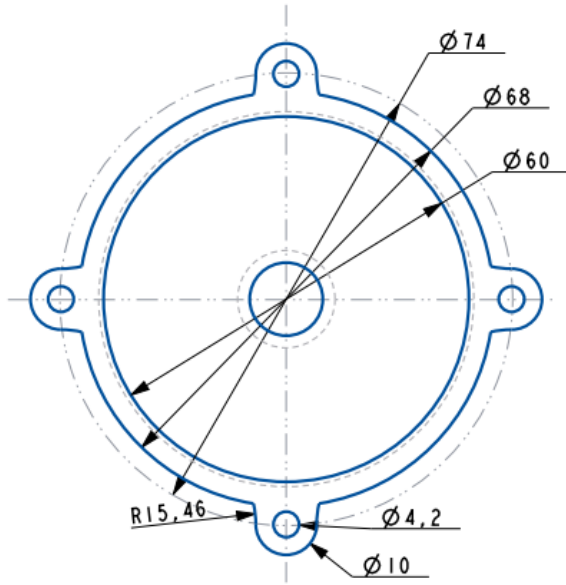
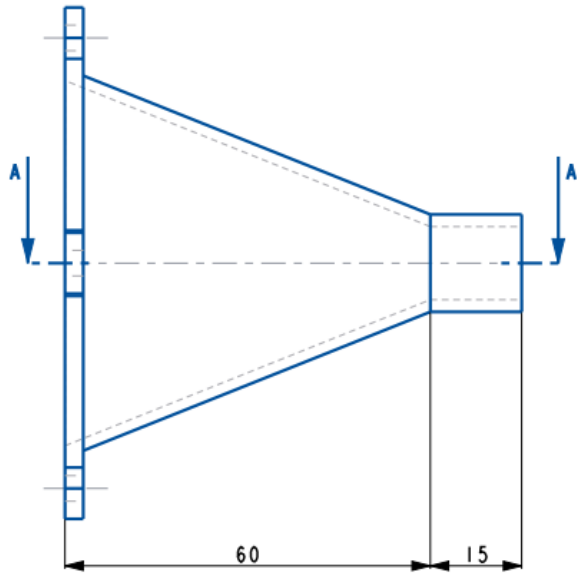




Alg. Tol. ISO2768-1	modelbestand: DENAYER_SOLID_PART_MMNS (PART) tekeningbestand: VIRTUAL_IMPACTOR_TOP .drw	25/02/2021
Alg. Tol. ISO2768-2		MAEM
Materiaal: ABS	KULeuven-technologiecampus De Nayer J. De Nayerlaan 5 BE 2860 Sint Katelijne Waver	Ruben Goos
Alg. ruwheid: /		Blad 1/1
Schaal: 1		A4
Projectie		

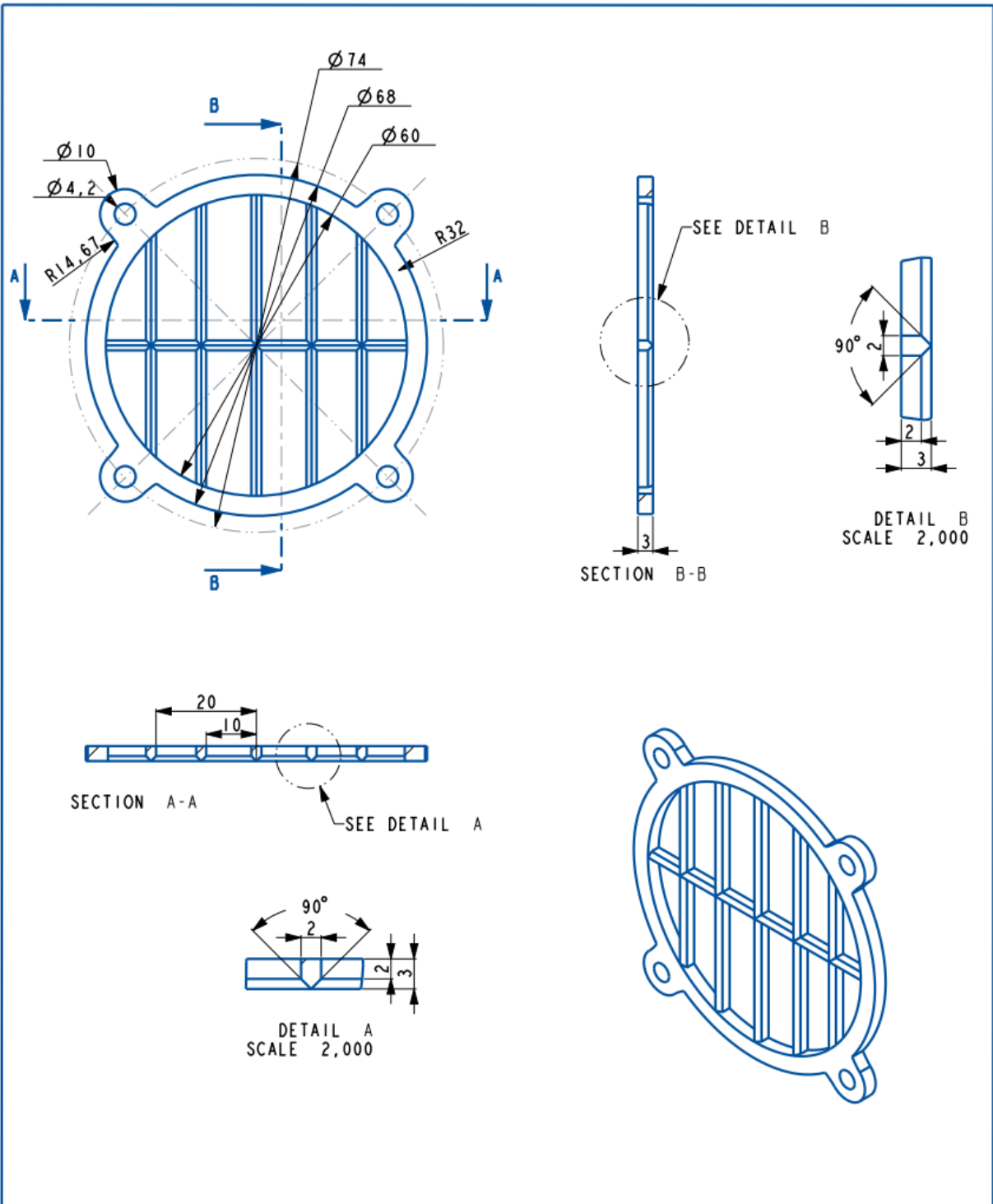


Alg. Tol. ISO2768-1	modelbestand: DENAYER_SOLID_PART_MMNS (PART) tekeningbestand: VIRTUAL_IMPACTOR_BOTTOM .drw	25/02/2021
Alg. Tol. ISO2768-2		MAEM
Materiaal: ABS		Ruben Goos
Alg. ruwheid: /		
Schaal: 1	KULeuven-technologiecampus De Nayer J. De Nayerlaan 5 BE 2860 Sint Katelijne Waver	Blad 1/1
Projectie		A4

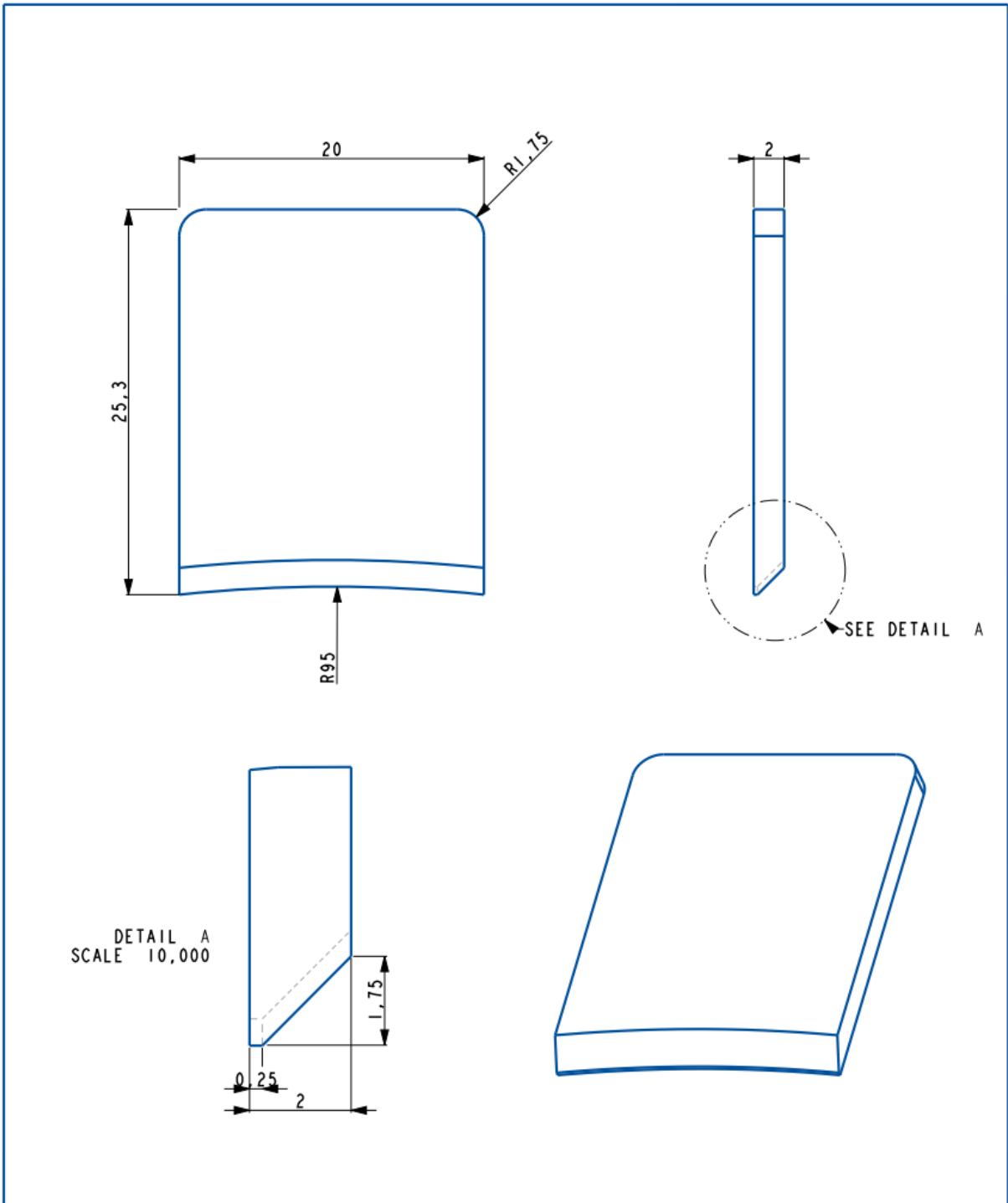


SECTION A-A

Alg. Tol. ISO2768-1	modelbestand: DENAYER_SOLID_PART_MMNS (PART) tekeningbestand: FILTER_MOUNT .drw	25/02/2021
Alg. Tol. ISO2768-2		MAEM
Materiaal: PLA		Ruben Goos
Alg. ruwheid: /		Blad 1/1
Schaal: 1	KULeuven-technologiecampus De Nayer J. De Nayerlaan 5 BE 2860 Sint Katelijne Waver	A4
Projectie		

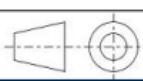


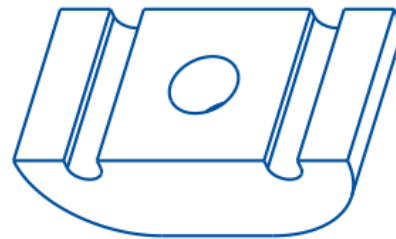
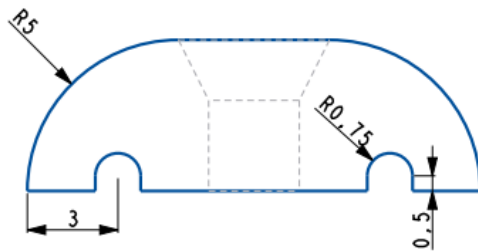
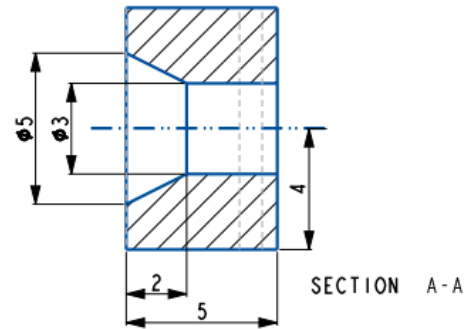
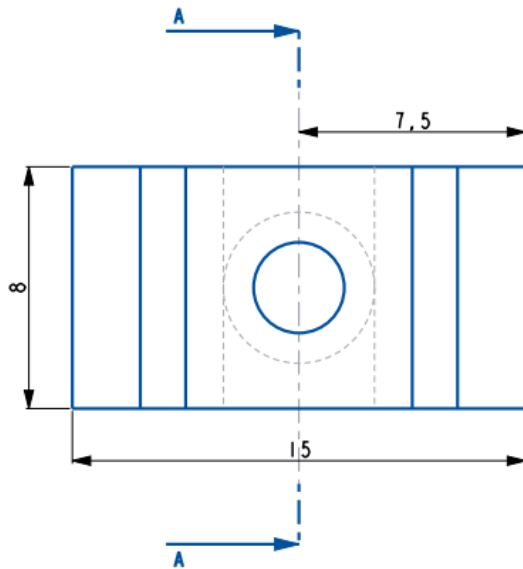
Alg. Tol. ISO2768-1	modelbestand: DENAYER_SOLID_PART_MMNS (PART) tekeningbestand: FILTER_GRIT .drw	25/02/2021
Alg. Tol. ISO2768-2		MAEM
Materiaal: PLA		Ruben Goos
Alg. ruwheid: /		
Schaal: 1	KULeuven-technologiecampus De Nayer J. De Nayerlaan 5 BE 2860 Sint Katelijne Waver	Blad 1/1
Projectie		A4



DETAIL A
SCALE 10,000

Alg. Tol. ISO2768-1	modelbestand: DENAYER_SOLID_PART_MMNS (PART) tekeningbestand: SQUEEGEE .drw	11/04/2021
Alg. Tol. ISO2768-2		MAEM
Materiaal: PLA		Ruben Goos
Alg. ruwheid: /		Blad 1/1
Schaal: 3	KULeuven-technologiecampus De Nayer J. De Nayerlaan 5 BE 2860 Sint Katelijne Waver	/A4
Projectie		





Alg. Tol. ISO2768-1	modelbestand: DENAYER_SOLID_PART_MMNS (PART) tekeningbestand: TREKONTLASTING .drw	11/04/2021
Alg. Tol. ISO2768-2		MAEM
Materiaal: PLA		Ruben Goos
Alg. ruwheid: /		Blad 1/1
Schaal: 5	KULEUVEN-TECHNOLOGIECAMPUS DE NAYER J. DE NAYERLAAN 5 BE 2860 SINT KATELIJNE WEVER	A4
Projectie 		

APPENDIX C: MATLAB SCRIPTS

1. Ramping load

```
%% load the data-----
data = load('F.txt'); %force

data11 = load('1.1.txt'); %resistance
data12 = load('1.2.txt'); %resistance
data13 = load('1.3.txt'); %resistance

data21 = load('2.1.txt'); %resistance
data22 = load('2.2.txt'); %resistance
data23 = load('2.3.txt'); %resistance

data31 = load('3.1.txt'); %resistance
data32 = load('3.2.txt'); %resistance
data33 = load('3.3.txt'); %resistance

data41 = load('4.1.txt'); %resistance
data42 = load('4.2.txt'); %resistance
data43 = load('4.3.txt'); %resistance

data51 = load('5.1.txt'); %resistance
data52 = load('5.2.txt'); %resistance
data53 = load('5.3.txt'); %resistance

data61 = load('6.1.txt'); %resistance
data62 = load('6.2.txt'); %resistance
data63 = load('6.3.txt'); %resistance

%% prepare the pressure-----
t = data(:,1); %first column
y = -data(:,2); %second column
y = y/(0.01*0.01) %calculate pressure
my = max(y) %maximal pressure

%% data11 preparation (ctr ENTER to run separate)-----
x11 = data11(:,1); %first column
y11 = data11(:,2); %second column

figure,plot(x11,y11) %Determine start and end point of measurement

id = find(x11>=9 & x11<=112); %ID start and end point measurement
y11 = y11(id); % correct resistance
P11 = linspace(0,my, size(y11,1)); %reduce samples pressure to match resistance
y11 = (y11 - max(y11)); %normalisation of data

%% data12 preparation (ctr ENTER to run separate)-----
x12 = data12(:,1); %first column
y12 = data12(:,2); %second column

figure,plot(x12,y12) %Determine start and end point of measurement

id = find(x12>=6 & x12<=109); %ID start and end point measurement
y12 = y12(id); % correct resistance
P12 = linspace(0,my, size(y12,1)); %reduce samples pressure to match resistance
y12 = (y12 - max(y12)); %normalisation of data

%% data13 preparation (ctr ENTER to run separate)-----
x13 = data13(:,1); %first column
y13 = data13(:,2); %second column
```

```

figure,plot(x13,y13) %Determine start and end point of measurement

id = find(x13>=27 & x13<=130); %ID start and end point measurement
y13 = y13(id); % correct resistance
P13 = linspace(0,my, size(y13,1)); %reduce samples pressure to match resistance
y13 = (y13 - max(y13)); %normalisation of data

%% data21 preparation (ctr ENTER to run separate)-----
x21 = data21(:,1); %first column
y21 = data21(:,2); %second column

figure,plot(x21,y21) %Determine start and end point of measurement

id = find(x21>=35 & x21<=138); %ID start and end point measurement
y21 = y21(id); % correct resistance
P21 = linspace(0,my, size(y21,1)); %reduce samples pressure to match resistance
y21 = (y21 - max(y21)); %normalisation of data

%% data22 preparation (ctr ENTER to run separate)-----
x22 = data22(:,1); %first column
y22 = data22(:,2); %second column

figure,plot(x22,y22) %Determine start and end point of measurement

id = find(x22>=48 & x22<=151); %ID start and end point measurement
y22 = y22(id); % correct resistance
P22 = linspace(0,my, size(y22,1)); %reduce samples pressure to match resistance
y22 = (y22 - max(y22)); %normalisation of data

%% data23 preparation (ctr ENTER to run separate)-----
x23 = data23(:,1); %first column
y23 = data23(:,2); %second column

figure,plot(x23,y23) %Determine start and end point of measurement

id = find(x23>=2 & x23<=105); %ID start and end point measurement
y23 = y23(id); % correct resistance
P23 = linspace(0,my, size(y23,1)); %reduce samples pressure to match resistance
y23 = (y23 - max(y23)); %normalisation of data

%% data31 preparation (ctr ENTER to run separate)-----
x31 = data31(:,1); %first column
y31 = data31(:,2); %second column

figure,plot(x31,y31) %Determine start and end point of measurement

id = find(x31>=11 & x31<=114); %ID start and end point measurement
y31 = y31(id); % correct resistance
P31 = linspace(0,my, size(y31,1)); %reduce samples pressure to match resistance
y31 = (y31 - max(y31)); %normalisation of data

%% data32 preparation (ctr ENTER to run separate)-----
x32 = data32(:,1); %first column
y32 = data32(:,2); %second column

figure,plot(x32,y32) %Determine start and end point of measurement

id = find(x32>=20 & x32<=123); %ID start and end point measurement
y32 = y32(id); % correct resistance
P32 = linspace(0,my, size(y32,1)); %reduce samples pressure to match resistance
y32 = (y32 - max(y32)); %normalisation of data

%% data33 preparation (ctr ENTER to run separate)-----
x33 = data33(:,1); %first column
y33 = data33(:,2); %second column

figure,plot(x33,y33) %Determine start and end point of measurement

```

```

id = find(x33>=17 & x33<=120); %ID start and end point measurement
y33 = y33(id); % correct resistance
P33 = linspace(0,my, size(y33,1)); %reduce samples pressure to match resistance
y33 = (y33 - max(y33)); %normalisation of data

%% data41 preparation (ctr ENTER to run separate)-----
x41 = data41(:,1); %first column
y41 = data41(:,2); %second column

figure,plot(x41,y41) %Determine start and end point of measurement

id = find(x41>=8 & x41<=111); %ID start and end point measurement
y41 = y41(id); % correct resistance
P41 = linspace(0,my, size(y41,1)); %reduce samples pressure to match resistance
y41 = (y41 - max(y41)); %normalisation of data

%% data42 preparation (ctr ENTER to run separate)-----
x42 = data42(:,1); %first column
y42 = data42(:,2); %second column

figure,plot(x42,y42) %Determine start and end point of measurement

id = find(x42>=17 & x42<=120); %ID start and end point measurement
y42 = y42(id); % correct resistance
P42 = linspace(0,my, size(y42,1)); %reduce samples pressure to match resistance
y42 = (y42 - max(y42)); %normalisation of data

%% data43 preparation (ctr ENTER to run separate)-----
x43 = data43(:,1); %first column
y43 = data43(:,2); %second column

figure,plot(x43,y43) %Determine start and end point of measurement

id = find(x43>=2 & x43<=105); %ID start and end point measurement
y43 = y43(id); % correct resistance
P43 = linspace(0,my, size(y43,1)); %reduce samples pressure to match resistance
y43 = (y43 - max(y43)); %normalisation of data

%% data51 preparation (ctr ENTER to run separate)-----
x51 = data51(:,1); %first column
y51 = data51(:,2); %second column

figure,plot(x51,y51) %Determine start and end point of measurement

id = find(x51>=15 & x51<=118); %ID start and end point measurement
y51 = y51(id); % correct resistance
P51 = linspace(0,my, size(y51,1)); %reduce samples pressure to match resistance
y51 = (y51 - max(y51)); %normalisation of data

%% data52 preparation (ctr ENTER to run separate)-----
x52 = data52(:,1); %first column
y52 = data52(:,2); %second column

figure,plot(x52,y52) %Determine start and end point of measurement

id = find(x52>=8 & x52<=111); %ID start and end point measurement
y52 = y52(id); % correct resistance
P52 = linspace(0,my, size(y52,1)); %reduce samples pressure to match resistance
y52 = (y52 - max(y52)); %normalisation of data

%% data53 preparation (ctr ENTER to run separate)-----
x53 = data53(:,1); %first column
y53 = data53(:,2); %second column

figure,plot(x53,y53) %Determine start and end point of measurement

id = find(x53>=9 & x53<=112); %ID start and end point measurement

```

```

y53 = y53(id); % correct resistance
P53 = linspace(0,my, size(y53,1)); %reduce samples pressure to match resistance
y53 = (y53 - max(y53)); %normalisation of data

%% data61 preparation (ctr ENTER to run separate)-----
x61 = data61(:,1); %first column
y61 = data61(:,2); %second column

figure,plot(x61,y61) %Determine start and end point of measurement

id = find(x61>=6 & x61<=109); %ID start and end point measurement
y61 = y61(id); % correct resistance
P61 = linspace(0,my, size(y61,1)); %reduce samples pressure to match resistance
y61 = (y61 - max(y61)); %normalisation of data

%% data62 preparation (ctr ENTER to run separate)-----
x62 = data62(:,1); %first column
y62 = data62(:,2); %second column

figure,plot(x62,y62) %Determine start and end point of measurement

id = find(x62>=8 & x62<=111); %ID start and end point measurement
y62 = y62(id); % correct resistance
P62 = linspace(0,my, size(y62,1)); %reduce samples pressure to match resistance
y62 = (y62 - max(y62)); %normalisation of data

%% data63 preparation (ctr ENTER to run separate)-----
x63 = data63(:,1); %first column
y63 = data63(:,2); %second column

figure,plot(x63,y63) %Determine start and end point of measurement

id = find(x63>=8 & x63<=111); %ID start and end point measurement
y63 = y63(id); % correct resistance
P63 = linspace(0,my, size(y63,1)); %reduce samples pressure to match resistance
y63 = (y63 - max(y63)); %normalisation of data

%% Calculating Mean and standard deviation-----
Y1 = [y11, y12, y13]; %combined dataset 3 measurements S1
M1 = mean(Y1,2); %mean 3 measurements S1
S1 = std(Y1,0,2); %Standard deviation 3 measurements S1

Y2 = [y21, y22, y23]; %combined dataset 3 measurements S2
M2 = mean(Y2,2); %mean 3 measurements S2
S2 = std(Y2,0,2); %Standard deviation 3 measurements S2

Y3 = [y31, y32, y33]; %combined dataset 3 measurements S3
M3 = mean(Y3,2); %mean 3 measurements S3
S3 = std(Y3,0,2); %Standard deviation 3 measurements S3

Y4 = [y41, y42, y43]; %combined dataset 3 measurements S4
M4 = mean(Y4,2); %mean 3 measurements S4
S4 = std(Y4,0,2); %Standard deviation 3 measurements S4

Y5 = [y51, y52, y53]; %combined dataset 3 measurements S5
M5 = mean(Y5,2); %mean 3 measurements S5
S5 = std(Y5,0,2); %Standard deviation 3 measurements S5

Y6 = [y61, y62, y63]; %combined dataset 3 measurements S6
M6 = mean(Y6,2); %mean 3 measurements S6
S6 = std(Y6,0,2); %Standard deviation 3 measurements S6

%% -----plotting and the visual effects-----

% overall figure settings -----
figure1 = figure, hold all %all on one figure
set(figure1, 'position',[100,100, 650, 450]) % define figure location and figure
size

```

```

hh = set(gca,'FontSize',20,'ticklabelinterpreter','latex',...
        'gridlinestyle',':','xaxislocation','bottom','gridcolor',0.6*[1 1 1],...
        'minorgridlinestyle','none');

box on, grid on, hold on;
% -----

%plotting of mean resistance -----
R1=plot(P11,M1,'-','linewidth',2.5,'color','b') % plot resistance S1
R2=plot(P21,M2,'-','linewidth',2.5,'color','k') % plot resistance S2
R3=plot(P31,M3,'-','linewidth',2.5,'color','c') % plot resistance S3
R4=plot(P41,M4,'-','linewidth',2.5,'color','m') % plot resistance S4
R5=plot(P51,M5,'-','linewidth',2.5,'color','g') % plot resistance S5
R6=plot(P61,M6,'-','linewidth',2.5,'color','y') % plot resistance S6
% -----

% plotting of standard variation with patching -----
X1 = [P11, fliplr(P11)]; %fliped
Y1_lower = M1'-S1' ; %lower boundary patch S1
Y1_upper = M1'+S1' ; %upper boundary patch S1
Y1 = [Y1_lower, fliplr(Y1_upper)]; % flipped
P1 = patch(X1,Y1,'b','facealpha',0.25,'linestyle','none'); %patching

X2 = [P21, fliplr(P21)]; %fliped
Y2_lower = M2'-S2' ; %lower boundary patch S2
Y2_upper = M2'+S2' ; %upper boundary patch S2
Y2 = [Y2_lower, fliplr(Y2_upper)]; %fliped
P2 = patch(X2,Y2,'k','facealpha',0.2,'linestyle','none'); %patching

X3 = [P31, fliplr(P31)]; %fliped
Y3_lower = M3'-S3' ; %lower boundary patch S3
Y3_upper = M3'+S3' ; %upper boundary patch S3
Y3 = [Y3_lower, fliplr(Y3_upper)]; %fliped
P3 = patch(X3,Y3,'c','facealpha',0.2,'linestyle','none'); %patching

X4 = [P41, fliplr(P41)]; %fliped
Y4_lower = M4'-S4' ; %lower boundary patch S4
Y4_upper = M4'+S4' ; %upper boundary patch S4
Y4 = [Y4_lower, fliplr(Y4_upper)]; %fliped
P4 = patch(X4,Y4,'m','facealpha',0.2,'linestyle','none'); %patching

X5 = [P51, fliplr(P51)]; %fliped
Y5_lower = M5'-S5' ; %lower boundary patch S5
Y5_upper = M5'+S5' ; %upper boundary patch S5
Y5 = [Y5_lower, fliplr(Y5_upper)]; %fliped
P5 = patch(X5,Y5,'g','facealpha',0.2,'linestyle','none'); %patching

X6 = [P61, fliplr(P61)]; %fliped
Y6_lower = M6'-S6' ; %lower boundary patch S6
Y6_upper = M6'+S6' ; %upper boundary patch S6
Y6 = [Y6_lower, fliplr(Y6_upper)]; %fliped
P6 = patch(X6,Y6,'y','facealpha',0.2,'linestyle','none'); %patching
% -----

%y-label-----
ylbl = ylabel('$\Delta R$  [$\Omega]$');
set(ylbl,'fontsize',20,'interpreter','latex','color',[0 0 0])
set(gca,'ylim',[-30, 0])
% -----

%X-label-----
xlbl = xlabel('Pressure [Pa]');
set(xlbl,'fontsize',20,'interpreter','latex')
set(gca, 'xlim',[0,my])
% -----

%legend-----

```

```
leg = legend([R1 R2 R3 R4 R5  
R6], 'S1$\pm$std', 'S2$\pm$std', 'S3$\pm$std', 'S4$\pm$std', 'S5$\pm$std', 'S6$\pm$std');  
set(leg, 'fontsize', 13, 'interpreter', 'latex')  
%-----
```


APPENDIX D: EXPERIMENTAL RESULTS

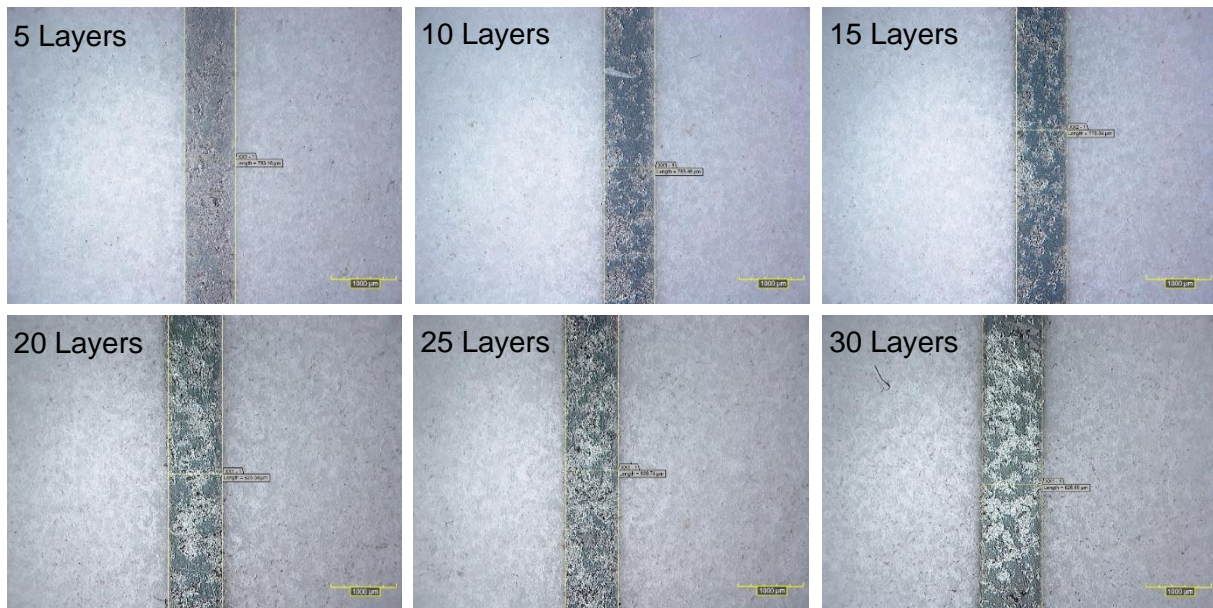
1. Experiment's printing parameters NEBULA5X-100s

To determine the optimal printing parameters for the NEBULA-5X100s on PA substrate, multiple experiments are conducted as explained in section 3.3.4. The results of the intermediate experiments are discussed in the following.

Experiment 1: Process parameters

Environment	Parameter	Value
T = 22.5°C RH = 35%	Substrate	Polished PA (2400 grit)
	Layers	5, 10, 15, 20, 25, 30
	Sintering temperature	130°C
	Sintering time	1h

Experiment 1: Microscopy



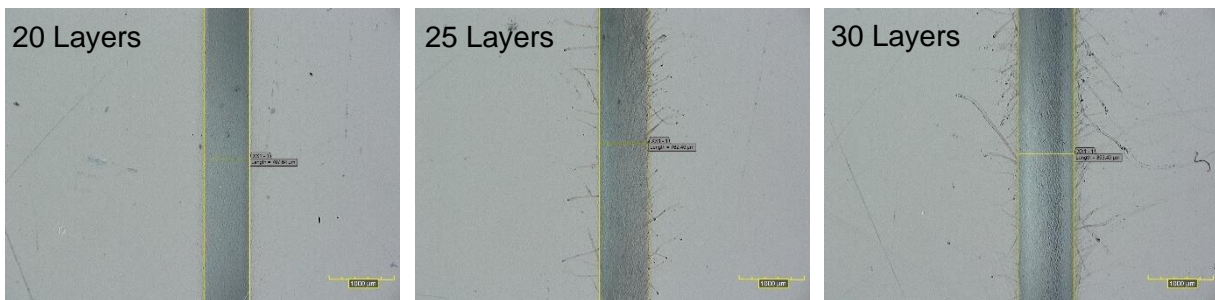
Experiment 1: Results

Number of layers	Average line width (µm)	Average resistance (kΩ)
5	759.59	/
10	784.87	/
15	784.87	/
20	787.68	/
25	824.18	3.81
30	933.69	2.16

Experiment 2: Process parameters

Environment	Parameter	Value
T = 23.5°C RH = 37%	Substrate	Glass
	Layers	20, 25, 30
	Sintering temperature	150°C
	Sintering time	4h

Experiment 2: Microscopy



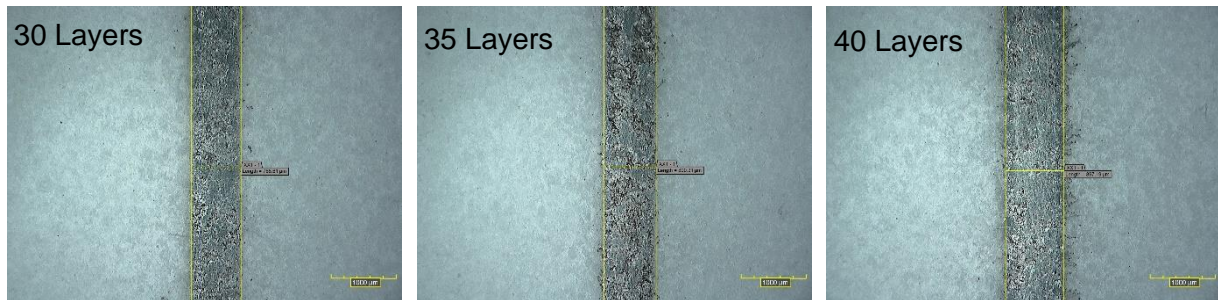
Experiment 2: Results

Number of layers	Average line width (μm)	Average resistance (Ω)
20	718.87	105.68
25	773.63	81.71
30	855.07	74.01

Experiment 3: Process parameters

Environment	Parameter	Value
T = 21.5°C RH = 40%	Substrate	Polished PA (2400 grit)
	Layers	30, 40, 50
	Sintering temperature	150°C
	Sintering time	4h

Experiment 3: Microscopy



Experiment 3: Results

Number of layers	Average line width (µm)	Average resistance (Ω)
30	768.01	157.42
35	805.23	84.27
40	900.00	43.91

2. Experiments printing parameters NEBULA5X-100s

Combination	x	y	z	a	c	Approval
1	x					✓
2		x				✓
3			x			✓
4				x		✓
5					x	✓
6	x	x				✓
7	x		x			✓
8	x			x		✓
9	x				x	✓
10		x	x			✓
11		x		x		✓
12		x			x	✓
13			x	x		✓
14			x		x	✓
15				x	x	✓
16	x	x	x			✓
17	x	x		x		✓
18	x	x			x	✓
19	x		x	x		✓
20	x		x		x	✓
21	x			x	x	✓
22		x	x	x		✓
23		x		x	x	✓
24			x	x	x	✓
25	x	x	x	x		✓
26	x		x	x	x	✓
27	x	x		x	x	✓
28	x	x	x		x	✓
29	x	x	x	x		✓
30	x	x	x	x	x	✓

APPENDIX E: G-CODE

1. 3-axis g-code test lines

#	G-code L1	G-code L2	G-code L3
1	G00G21G54G40G90	G00G21G54G40G90	G00G21G54G40G90
2	Z30	Z30	Z30
3	X0.Y0.A0.C0.	X0.Y0.A0.C0.	X0.Y0.A0.C0.
4	G99	G99	G99
5	T1M6	T1M6	T1M6
6	S5000M3	S5000M3	S5000M3
7	G0X40.Y55.	G0X55.Y40.	G0X25.Y55.
8	Z17.922	Z17.922	Z16.715
9	G1Z12.722F50.	G1Z12.722F50.	G1Z11.515F50.
10	G19	G18	X25.602Y54.398Z11.706
11	G3Y25.Z12.722J-15.K-93.808	G3X25.Z12.722I-15.K-93.808	X26.204Y53.796Z11.889
12	G1Z30.	G1Z30.	X26.808Y53.192Z12.064
13	M30	M30	X27.413Y52.587Z12.231
14			X28.019Y51.981Z12.39
15			X28.626Y51.374Z12.542
16			X29.234Y50.766Z12.686
17			X29.843Y50.157Z12.821
18			X30.453Y49.547Z12.949
19			X31.063Y48.937Z13.069
20			X31.675Y48.325Z13.181
21			X32.287Y47.713Z13.285
22			X32.899Y47.101Z13.381
23			X33.513Y46.487Z13.47
24			X34.127Y45.873Z13.55
25			X34.741Y45.259Z13.622
26			X35.356Y44.644Z13.686
27			X35.971Y44.029Z13.743
28			X36.586Y43.414Z13.791
29			X37.202Y42.798Z13.831
30			X37.818Y42.182Z13.864
31			X38.434Y41.566Z13.888
32			X39.051Y40.949Z13.904
33			X39.667Y40.333Z13.912
34			X40.284Y39.716
35			X40.9Y39.1Z13.905
36			X41.516Y38.484Z13.889

37			X42.132Y37.868Z13.866
38			X42.749Y37.251Z13.834
39			X43.364Y36.636Z13.794
40			X43.98Y36.02Z13.747
14			X44.595Y35.405Z13.691
42			X45.21Y34.79Z13.627
43			X45.824Y34.176Z13.556
44			X46.438Y33.562Z13.476
45			X47.051Y32.949Z13.389
46			X47.664Y32.336Z13.293
47			X48.276Y31.724Z13.19
48			X48.888Y31.112Z13.078
49			X49.498Y30.502Z12.959
50			X50.108Y29.892Z12.832
51			X50.717Y29.283Z12.697
52			X51.325Y28.675Z12.554
53			X51.932Y28.068Z12.403
54			X52.538Y27.462Z12.244
55			X53.143Y26.857Z12.077
56			X53.747Y26.253Z11.903
57			X54.35Y25.65Z11.721
58			X54.952Y25.048Z11.531
59			X55.Y25.Z11.515
60			Z30.
61			M30

2. 5-axis g-code test lines

#	G-code L1	G-code L2	G-code L3
1	G00G21G54G40G90	G00G21G54G40G90	G00G21G54G40G90
2	Z10	Z10	Z10
3	X0.Y0.A0.C0.	X0.Y0.A0.C0.	X0.Y0.A0.C0.
4	G99	G99	G99
5	T1M6	T1M6	T1M6
6	S5000M3	S5000M3	S5000M3
7	G0Z30.	G0Z30.	G0Z30.
8	X40.Y55.821C0.A9.085	X55.821Y40.C-90.A9.085	X24.179Y55.821C45.A12.903
9	Z17.857	Z17.857	Z16.584
10	G1Y55.Z12.722F50.	G1X55.Z12.722F50.	G1X25.Y55.Z11.515F50.
11	Y53.733Z12.916A8.312	X53.733Z12.916A8.312	X26.452Y53.548Z11.962A11.635
12	Y51.Z13.275A6.649	X51.Z13.275A6.649	X28.366Y51.634Z12.478A9.973
13	Y48.258Z13.554A4.987	X48.258Z13.554A4.987	X30.291Y49.709Z12.916A8.31
14	Y45.509Z13.754A3.325	X45.509Z13.754A3.325	X32.223Y47.777Z13.275A6.648
15	Y42.755Z13.874A1.662	X42.755Z13.874A1.662	X34.162Y45.838Z13.554A4.986
16	Y40.Z13.914A0.	X40.Z13.914A0.	X36.105Y43.895Z13.754A3.324
17	Y38.718Z13.905A-.773	X38.718Z13.905A-.773	X38.053Y41.947Z13.874A1.661
18	Y35.963Z13.828A-2.435	X35.963Z13.828A-2.435	X40.Y40.Z13.914A0.
19	Y33.211Z13.671A-4.098	X33.211Z13.671A-4.098	X41.486Y38.514Z13.89A-1.268
20	Y30.465Z13.434A-5.76	X30.465Z13.434A-5.76	X43.433Y36.567Z13.789A-2.93
21	Y27.727Z13.118A-7.423	X27.727Z13.118A-7.423	X45.378Y34.622Z13.609A-4.592
22	Y25.Z12.722A-9.085	X25.Z12.722A-9.085	X47.318Y32.682Z13.348A-6.254
23	Z30.	Z30.	X49.252Y30.748Z13.008A-7.917
24	M30	M30	X51.179Y28.821Z12.589A-9.579
25			X53.096Y26.904Z12.091A-11.242
26			X55.Y25.Z11.515A-12.903
27			Z30.
28			M30

3. 3-axis g-code improved sensor design

#	Electrode left (10 passes)	Electrode right (10 passes)
1	G00G21G54G40G90	G00G21G54G40G90
2	Z30	Z30
3	X0.Y0.A0.C0.	X0.Y0.A0.C0.
4	G99	G99
5	T1M6	T1M6
6	S5000M3	S5000M3
7	G0Z35.414	G0Z35.414
8	X35.65Y32.5	X44.35Y32.5
9	Z30.223	Z30.223
10	G1Z25.023F50.	G1Z25.023F50.
11	G19	G19
12	G3Y12.5Z21.31J7.5K-96.109	G3Y12.5Z21.31J7.5K-96.109
13	G2Y32.5Z25.023J27.5K-92.396	G2Y32.5Z25.023J27.5K-92.396
14	G3Y12.5Z21.31J7.5K-96.109	G3Y12.5Z21.31J7.5K-96.109
15	G2Y32.5Z25.023J27.5K-92.396	G2Y32.5Z25.023J27.5K-92.396
16	G3Y12.5Z21.31J7.5K-96.109	G3Y12.5Z21.31J7.5K-96.109
17	G2Y32.5Z25.023J27.5K-92.396	G2Y32.5Z25.023J27.5K-92.396
18	G3Y12.5Z21.31J7.5K-96.109	G3Y12.5Z21.31J7.5K-96.109
19	G2Y32.5Z25.023J27.5K-92.396	G2Y32.5Z25.023J27.5K-92.396
20	G3Y12.5Z21.31J7.5K-96.109	G3Y12.5Z21.31J7.5K-96.109
21	G2Y32.5Z25.023J27.5K-92.396	G2Y32.5Z25.023J27.5K-92.396
22	G1Z35.414	G1Z35.414
23	M30	M30

#	Contact pad left (10 passes)	Contact pad right (10 passes)
1	G00G21G54G40G90	G00G21G54G40G90
2	Z30	Z30
3	X0.Y0.A0.C0.	X0.Y0.A0.C0.
4	G99	G99
5	T1M6	T1M6
6	S5000M3	S5000M3
7	G0Z35.414	G0Z35.414
8	X33.85Y12.5	X46.15Y12.5
9	Z26.408	Z26.408
10	G1Z21.208F50.	G1Z21.208F50.
11	G19	G19
12	% ----- (repeated 5 times) -----	% ----- (repeated 5 times) -----
13	G2Y17.5Z22.552J27.5K-92.294	G2Y17.5Z22.552J27.5K-92.294
14	G1X34.25Z22.578	G1X45.75Z22.578

15	G3Y12.5Z21.233J22.5K-93.664	G3Y12.5Z21.233J22.5K-93.664
16	G1X34.65Z21.257	G1X45.35Z21.257
17	G2Y17.5Z22.601J27.5K-92.343	G2Y17.5Z22.601J27.5K-92.343
18	G1X35.05Z22.623	G1X44.95Z22.623
19	G3Y12.5Z21.28J22.5K-93.709	G3Y12.5Z21.28J22.5K-93.709
20	G1X35.45Z21.3	G1X44.55Z21.3
21	G2Y17.5Z22.644J27.5K-92.386	G2Y17.5Z22.644J27.5K-92.386
22	G1X35.85Z22.662	G1X44.15Z22.662
23	G3Y12.5Z21.319J22.5K-93.748	G3Y12.5Z21.319J22.5K-93.748
24	G1X36.25Z21.336	G1X43.75Z21.336
25	G2Y17.5Z22.679J27.5K-92.422	G2Y17.5Z22.679J27.5K-92.422
26	G1X36.65Z22.694	G1X43.35Z22.694
27	G3Y12.5Z21.352J22.5K-93.78	G3Y12.5Z21.352J22.5K-93.78
28	G1X37.05Z21.365	G1X42.95Z21.365
29	G2Y17.5Z22.708J27.5K-92.451	G2Y17.5Z22.708J27.5K-92.451
30	G1X37.45Z22.719	G1X42.55Z22.719
31	G3Y12.5Z21.377J22.5K-93.805	G3Y12.5Z21.377J22.5K-93.805
32	G2Y17.5Z22.719J27.5K-92.463	G2Y17.5Z22.719J27.5K-92.463
33	G1X37.05Z22.708	G1X42.95Z22.708
34	G3Y12.5Z21.365J22.5K-93.794	G3Y12.5Z21.365J22.5K-93.794
35	G1X36.65Z21.352	G1X43.35Z21.352
36	G2Y17.5Z22.694J27.5K-92.438	G2Y17.5Z22.694J27.5K-92.438
37	G1X36.25Z22.679	G1X43.75Z22.679
38	G3Y12.5Z21.336J22.5K-93.765	G3Y12.5Z21.336J22.5K-93.765
39	G1X35.85Z21.319	G1X44.15Z21.319
40	G2Y17.5Z22.662J27.5K-92.405	G2Y17.5Z22.662J27.5K-92.405
41	G1X35.45Z22.644	G1X44.55Z22.644
42	G3Y12.5Z21.3J22.5K-93.73	G3Y12.5Z21.3J22.5K-93.73
43	G1X35.05Z21.28	G1X44.95Z21.28
44	G2Y17.5Z22.623J27.5K-92.366	G2Y17.5Z22.623J27.5K-92.366
45	G1X34.65Z22.601	G1X45.35Z22.601
46	G3Y12.5Z21.257J22.5K-93.687	G3Y12.5Z21.257J22.5K-93.687
47	G1X34.25Z21.233	G1X45.75Z21.233
48	G2Y17.5Z22.578J27.5K-92.319	G2Y17.5Z22.578J27.5K-92.319
49	G1X33.85Z22.552	G1X46.15Z22.552
50	G3Y12.5Z21.208J22.5K-93.638	G3Y12.5Z21.208J22.5K-93.638
51	% ----- (repeated 5 times) -----	% ----- (repeated 5 times) -----
52	G1Z35.414	G1Z35.414
53	M30	M30

APPENDIX F: DATASHEETS

1. Silver ink CUR AG-001

SAFETY DATA SHEET

according to Regulation (EC) No 1907/2006 (REACH Annex II) and its amendments



CUR AG-001

SUBID : 000001013629

Version 0

Print Date 26.08.2015

Revision Date 00.00.0000

1. IDENTIFICATION OF THE SUBSTANCE/MIXTURE AND OF THE COMPANY/UNDERTAKING

1.1 Identification of the substance or mixture:

Product name : CUR AG-001
REACH Registration No : Registration numbers of the individual components: see section 3.2, if applicable.

1.2 Use of the substance/mixture:

Identified relevant uses : Electronic ink
Uses advised against : Do not use for private purposes (household). Do not use for products which come into direct contact with food stuffs. Do not use for products which come into direct contact with the skin.

1.3 Company/undertaking identification

Agfa-Gevaert NV
Septestraat 27
2640 Mortsel
Belgium
Tel. : +32 3 4445501
Fax : +32 3 4445503
E-mail: electronic.sds@agfa.com

1.4 Emergency telephone

Emergency telephone number : +32 3 4443333 (24h/24h)

2. HAZARDS IDENTIFICATION

2.1 Classification of the substance or mixture:

Regulation(EC) No 1272/2008 (CLP)	
• Hazard classes	Acute toxicity Oral
Hazard categories	Category 4
Hazard statements	H302
Classification procedure	According the classification criteria of CLP Regulation (EC) No 1272/2008.
• Hazard classes	Serious eye damage
Hazard categories	Category 1
Hazard statements	H318
Classification procedure	According the classification criteria of CLP Regulation (EC) No 1272/2008.
• Hazard classes	Chronic hazards to the aquatic environment
Hazard categories	Category 1
Hazard statements	H410
Classification procedure	According the classification criteria of CLP Regulation (EC) No 1272/2008.
• Hazard classes	Flammable liquids
Hazard categories	Category 3
Hazard statements	H226
Classification procedure	According the classification criteria of CLP Regulation (EC) No 1272/2008.

BE

1/17

EN

SAFETY DATA SHEET

according to Regulation (EC) No 1907/2006 (REACH Annex II) and its amendments



CUR AG-001

SUBID : 000001013629

Version 0

Print Date 26.08.2015

Revision Date 00.00.0000

• Hazard classes	Skin irritation
Hazard categories	Category 2
Hazard statements	H315
Classification procedure	According the classification criteria of CLP Regulation (EC) No 1272/2008.
• Hazard classes	Acute hazards to the aquatic environment
Hazard categories	Category 1
Hazard statements	H400
Classification procedure	According the classification criteria of CLP Regulation (EC) No 1272/2008.
• Hazard classes	Specific target organ toxicity - single exposure
Hazard categories	Category 3
Hazard statements	H335
Classification procedure	According the classification criteria of CLP Regulation (EC) No 1272/2008.
• Hazard classes	Specific target organ toxicity - single exposure
Hazard categories	Category 3
Hazard statements	H336
Classification procedure	According the classification criteria of CLP Regulation (EC) No 1272/2008.

Full text of each relevant H-phrase is listed in section 16.

2.2 Label elements:

Hazardous components which must be listed on the label :

- CAS-No. : 7440-22-4 silver nano (powder <1mm)
- 71-36-3 butan-1-ol; n-butanol

Symbol(s)



GHS07



GHS09



GHS02



GHS05

Signal word	: DANGER	
Hazard statements	: H302	Harmful if swallowed.
	H315	Causes skin irritation.
	H318	Causes serious eye damage.
	H410	Very toxic to aquatic life with long lasting effects.
	H226	Flammable liquid and vapour.
	H335	May cause respiratory irritation.
	H336	May cause drowsiness or dizziness.
Precautionary statements: prevention	: P280	Wear protective gloves/protective clothing/eye protection/face protection.
	P273	Avoid release to the environment.
	P210	Keep away from heat, hot surfaces, sparks, open flames and other ignition sources. No smoking.
	P261	Avoid breathing dust/fume/gas/mist/vapours/spray.
Precautionary statements:	: P337+P313	If eye irritation persists: Get medical advice/attention.

BE

2/17

EN

SAFETY DATA SHEET

according to Regulation (EC) No 1907/2006 (REACH Annex II) and its amendments



CUR AG-001

SUBID : 000001013629

Version 0

Print Date 26.08.2015

Revision Date 00.00.0000

response

P391 Collect spillage.
 P305+P351+P338 IF IN EYES: Rinse cautiously with water for several minutes. Remove contact lenses, if present and easy to remove. Continue rinsing.
 P310 Immediately call a POISON CENTER/doctor/...
 P403+P235 Store in a well-ventilated place. Keep cool.

Precautionary statements:
 storage

2.3 Other hazards:

This product does not meet the criteria concerning PBT or vPvB substances as described in Annex XIII of the REACH regulation (1907/2006 EC)

3. COMPOSITION/INFORMATION ON INGREDIENTS

3.1 Mixture related information:

Photographic chemical, mainly consisting of:

3.2 Hazard ingredients:

The hazard and labelling information in this section is that of the individual ingredients. The corresponding information relative to this product as supplied is given in section 2.1.

Hazardous components in the meaning of regulation(EC) No 1272/2008 (CLP)

• silver nano (powder <1mm)	Concentration [%] :	10,0	-	30,0
CAS-No.	:	7440-22-4		
EINECS-No.	:	231-131-3		
REACH Registration No	:	01-2119555669-21-XXXX		
Hazard classes	:	Acute hazards to the aquatic environment, Chronic hazards to the aquatic environment		
Hazard categories	:	Category 1, Category 1		
Hazard statements	:	H400, H410		
• 2-Phenoxyethanol	Concentration [%] :	25,0	-	55,0
CAS-No.	:	122-99-6		
Index-No.	:	603-098-00-9		
EINECS-No.	:	204-589-7		
REACH Registration No	:	01-2119488943-21-XXXX		
Hazard classes	:	Acute toxicity Oral, Serious eye irritation		
Hazard categories	:	Category 4, Category 2		
Hazard statements	:	H302, H319		
• Propylene carbonate	Concentration [%] :	0,0	-	15,0
CAS-No.	:	108-32-7		
Index-No.	:	607-194-00-1		
EINECS-No.	:	203-572-1		
REACH Registration No	:	01-2119537232-48-XXXX		
Hazard classes	:	Serious eye irritation		
Hazard categories	:	Category 2		
Hazard statements	:	H319		
• butan-1-ol, n-butanol	Concentration [%] :	0,0	-	35,0
CAS-No.	:	71-36-3		
Index-No.	:	603-004-00-6		

BE

3/17

EN

SAFETY DATA SHEET

according to Regulation (EC) No 1907/2006 (REACH Annex II) and its amendments



CUR AG-001

SUBID : 000001013629

Version 0

Print Date 26.08.2015

Revision Date 00.00.0000

EINECS-No. : 200-751-6
REACH Registration No : 01-2119484630-38-XXXX
Hazard classes : Flammable liquids, Acute toxicity Oral, Specific target organ toxicity - single exposure, Skin irritation, Serious eye damage, Specific target organ toxicity - single exposure
Hazard categories : Category 3, Category 4, Category 3, Category 2, Category 1, Category 3
Hazard statements : H226, H302, H335, H315, H318, H336

Components with a community workplace exposure limit

- silver nano (powder <1mm)
- 2-Phenoxyethanol
- butan-1-ol; n-butanol

M-factor

- silver nano (powder <1mm)
Acute hazards to the aquatic environment : 1
Chronic hazards to the aquatic environment : 10

3.3 Remark:

Full text of each relevant H-phrase is listed in section 16.

4. FIRST AID MEASURES

4.1 Description of first aid measures:

Eye contact : IF IN EYES: Rinse cautiously with water for several minutes. Remove contact lenses, if present and easy to remove. Continue rinsing. Consult ophthalmologist.
Skin contact : Wash off with soap and water. Consult a physician.
Ingestion : Rinse mouth with plenty of water. Do not induce vomiting. Consult a physician.
Inhalation : Take person to fresh air. If breathing is irregular or stopped, administer artificial respiration. Consult a physician.

4.2 Most important symptoms and effects:

Symptoms : Eyes: Corrosive, lacrimation, impaired vision, severe burns. Upon contact with skin: redness, pain.

4.3 Indication of immediate medical attention and special treatment needed:

General advice : Call a physician immediately.

5. FIRE-FIGHTING MEASURES

5.1 Extinguishing media

Suitable extinguishing media : Alcohol-resistant foam., Carbon dioxide (CO₂)., Dry extinguishing powder., Water.
Extinguishing media which must not be used for safety reasons : Do not use a solid water stream as it may scatter and spread fire.

BE

4/17

EN

SAFETY DATA SHEET

according to Regulation (EC) No 1907/2006 (REACH Annex II) and its amendments



CUR AG-001

SUBID : 000001013629

Version 0

Print Date 26.08.2015

Revision Date 00.00.0000

5.2 Special hazards arising from the substance or mixture:

Specific hazards during fire fighting : In case of fire, thermal decomposition with emission of hazardous fumes is possible Carbon oxides Vapours may form explosive mixtures with air.

Further information : Collect contaminated fire extinguishing water separately. This must not be discharged into drains. Cool closed containers exposed to fire with water spray.

5.3 Advice for fire-fighters:

Special protective equipment for fire-fighters : Regular fire intervention clothes. In the event of fire, wear self-contained breathing apparatus.

6. ACCIDENTAL RELEASE MEASURES

6.1 Personal precautions, protective equipment and emergency procedures:

Personal precautions : Cleanup personnel must use appropriate personal protective equipment.

Additional advice : Observe normal precautions when handling chemicals. Take measures to prevent the build up of electrostatic charge. All parts of the installation should be earthed carefully. Keep away from heat and sources of ignition.

6.2 Environmental precautions:

Environmental precautions : The product should not be allowed to enter drains, water courses or the soil.

6.3 Methods and material for containment and cleaning up:

Methods for cleaning up : Dike the spill if necessary. If spill occurs, apply a suitable absorbent material and collect into an impervious waste container. Collect the product in a plastic vessel. Carefully collect leftovers.

6.4 Reference to other sections:

For waste disposal see section 13.

For personal protection see section 8.

7. HANDLING AND STORAGE

7.1 Precautions for safe handling:

Advice on safe handling : Prevent product from diffusing.

Hygiene measures : Observe normal precautions when handling chemicals. Employees should wash their hands and face before eating, drinking, or using tobacco products. Keep away from foodstuffs, drinks and tobacco. Strict hygiene.

Advice on protection against fire and explosion : Use fire-proof electrical material. Take precautionary measures against static discharges. Keep away from heat and sources of ignition.

BE

5/17

EN

SAFETY DATA SHEET

according to Regulation (EC) No 1907/2006 (REACH Annex II) and its amendments



CUR AG-001

SUBID : 000001013629

Version 0

Print Date 26.08.2015

Revision Date 00.00.0000

7.2 Conditions for safe storage:

- Requirements for storage areas and containers : Keep container tightly closed. Keep in a dry, cool place.
- Further information on storage conditions : Keep container in a well-ventilated place. Protect against extremes of temperature and direct sunlight.
- Advice on common storage : Store away from oxidizing agents. Store away from strong alkalis.

7.3 Specific end use:

This substance is used only by trained professionals under restricted conditions.

8. EXPOSURE CONTROLS / PERSONAL PROTECTION

8.1 Control parameters:

8.1.1 Components with occupational exposure limits resp. biological occupational exposure limits requiring monitoring:

8.1.1.1 Occupational exposure limits:

Air limit values

- silver nano (powder <1µm)

CAS-No.: 7440-22-4

Basis	Revision Date	Value	Type
OEL (BE)	10 2002	0,1 mg/m ³	TWA
EU ELV	05 2003	0,1 mg/m ³	TWA

- butan-1-ol; n-butanol

CAS-No.: 71-36-3

Basis	Revision Date	Value	Type
OEL (BE)	06 2009	62 mg/m ³ 20 ppm	TWA

Biological limit values

We are not aware of any national exposure limit.

8.1.1.2 Additional exposure limits under the conditions of use:

No other exposure limits applicable.

8.1.1.3 DNEL/DMEL and PNEC-values:

DNEL

No DNEL/DMEL value determined. No Chemical Safety Report performed.

PNEC

No PNEC value determined. No Chemical Safety Report performed.

8.2 Exposure controls:

Occupational exposure controls:

- Instruction measures to prevent exposure:

BE

6/17

EN

2. Piezoresistive ink EMS CI-2050



Engineered Conductive Materials by
Engineered Materials Systems, Inc.

132 Johnson Drive
Delaware, Ohio 43015-8699
Tel: (740) 362-4444
Fax: (740) 362-4433
www.conductives.com

Technical Data Sheet

CI-2050 HR/ CI-2050 LR
Conductive Ink

DESCRIPTION CI-2050 LR Is a carbon based screen printable polymer thick film. When properly configured it can provide a variable printed resistor. CI-2050 LR offers adhesion to a wide spectrum of substrates including polyester, paper, cloth, and most plastic films. CI-2050 LR has been formulated to have good flexibility, and fast curing properties. While CI-2050 LR is application ready with no dilution needed, the electrical resistance can be adjusted with CI-2050 HR

ADVANTAGES

- ✓ Excellent adhesion
- ✓ Superior flexibility
- ✓ Extended screen residence times
- ✓ No dilution required
- ✓ Fast curing
- ✓ Excellent printability

**TYPICAL
UNCURED
PROPERTIES**

Color	Black
Appearance	Thixotropic paste
Total Solids Content	CI-2050 HR = 31% CI-2050 LR = 32%
Density	CI-2050 HR =10.13 lbs/Gal.
Density	CI-2050 LR =10.3 lbs/Gal
Flash Point	212°F (100°C) Tag Closed Cup
VOC	CI-2050 HR 1132 grams/liter
VOC	CI-2050 LR 835.6 grams/liter
Theoretical Coverage	CI-2050 HR 447 Sq ft ² /Gal/Mil 9.02 m ² /kilogram/25.4 microns 14.23 grams / sq. inch / Mil CI-2050 LR 450 Sq ft ² /Gal/Mil 8.16 m ² /kilogram/25.4 microns 13.88 Gms/ Sq. Inch / Mil

**TYPICAL CURED
PROPERTIES**

Electrical Resistance	CI-2050 LR 1,500 – 2,500 ohms/sq/mil
	CI-2050 HR >10M ohms/sq/mil

APPLICATION INFORMATION

- Screen print **CI-2050 LR** with any screen emulsion/mesh combination that yields a wet film thickness of 0.5-0.8 mils. The dry film will yield a dry film thickness of 0.3-0.5 mils.
- Typical screens used are 180-220 mesh with a 1.0 mil emulsion.
- Stainless steel fabric can be used to increase dry film thickness.
- Repeating the cure cycle and observing the electrical resistance change can confirm complete cure. The electrical resistance should not decrease by more than 3%.
- Typically, it is not possible to over cure **CI-2050 LR**. Added curing will improve the flexibility and reduce the electrical resistance.
- **CI-2050 LR** can also be cured with infrared energy. This method often provides improved properties over conventional heat curing.
- **CI-2050 LR** can be blended with **CI-2050 HR** to increase electrical resistance values. Please contact an ECM technical Service professional for recommendations.

CURE SCHEDULE

CI-2050 LR: 10 Min @ 250 ° F. Peak cure temperature should exceed peak operating temperature by 100° F.

CLEAN UP

CI-2050 LR can be cleaned up with M.E.K (Methyl Ethyl Ketone) or a blend of solvents that will completely remove a cured film. Screens and printing tools should be allowed to dry completely before reuse. To avoid possible squeegee swelling, a solvent resistant material such as polyurethane should be used. Typically a high durometer squeegee will provide the best results.

STORAGE AND HANDLING

- Shelf life is six (6) months in an unopened container, stored below 70°F.
- Store product below 70°F for maximum shelf life and minimal solvent loss. Avoid high temperature exposure.
- It is suggested that the product be stored at < 55°F to increase shelf life. The product must be conditioned back to room temperature before used.

HEALTH AND SAFETY

- Use with adequate ventilation.
- Avoid skin contact.
- If ingested, consult a physician immediately.
- Consult the product Material Safety Data Sheet for additional information.

APPLICATION ASSISTANCE

ECM's application specialists are available to assist you with your production start-up. For more information, please call ECM at 1.740.362.4444.

Notice: All statements, recommendations, and information contained herein are based on test results that Engineered Conductive Materials, LLC believes to be accurate and reliable. The user shall determine the suitability of this material for his intended purpose and application. No warranties, whether expressed or implied for fitness for a particular purpose shall apply to this material.

3. Silver conductive epoxy adhesive

Silver Conductive Epoxy Adhesive, Moderate Cure / High Conductivity



RoHS
Compliant

Description

This is a two-part, smooth, silver paste adhesive that cures to form a hard, durable polymer. In its cured state, it is highly electrically and thermally conductive. It adheres strongly to metals and glass, and it adheres well to most plastics used in electronic assemblies.

It has a convenient 1-to-1 mix ratio and a 10-minute working life. It achieves an operational cure in five hours at room temperature and full cure in a day. At 65°C, it cures in only 15 minutes.

Applications and Usages

The MC002966 can be used as a solder replacement for bonding heat-sensitive electronic components and for making conductive bonds where solder is not an option, such as when bonding to glass, plastics, or soft metals. It allows for quick, cold soldering repairs of electronic devices. Furthermore, it makes excellent thermal connections, provides excellent EMI/RFI shielding, and is very effective at filling in seams between metal plates. It is especially useful in repairing rear window defrosters on automobiles.

Its primary applications are in the repair and assembly of electronic devices. It is used in the automobile, aerospace, marine, communication, instrumentation, and industrial control equipment industries. It is also widely used by hobbyists and makers.

Benefits and Features

- Electrical resistivity: 0.007 $\Omega \cdot \text{cm}$
- Thermal conductivity: 0.90 W/(m·K)
- 1:1 mix ratio by volume
- Working life: 10 minutes
- Cure time: 24 hours at room temperature or 15 minutes at 65°C
- Good adhesive strength
- Strong resistance to water, brine, acids, bases, and aliphatic hydrocarbons
- Room temperature storage
- Shelf life greater than three years

Usage Parameters

Properties	Value
Working Time ^{a)}	10 min
Shelf Life	≥ 3 year
Service Cure @ 22°C (72°F)	5 hour
Full Cure @ 22°C (72°F)	24 hour
Full Cure @ 65°C (149°F)	15 min
Full Cure @ 90°C (194°F)	12 min
Full Cure @ 125°C (257°F)	7 min
Full Cure @ 150°C (302°F)	5 min

Temperature Ranges

Properties	Value
Constant Service Temperature	-55 to 150°C
	(-67 to 302°F)
Storage Temperature of Unmixed Parts	16 to 27°C
	(60 to 80°F)

^{a)} Cure and life values 5 g and room temperature unless stated otherwise.

Principal Components

Part A: Bis-F Epoxide Resin
Metallic Silver
Part B: Aliphatic Amines
Metallic Silver

www.element14.com
www.farnell.com
www.newark.com



Silver Conductive Epoxy Adhesive, Moderate Cure / High Conductivity



Properties of Cured MC002966

Physical Properties	Method	Value ^{a)}	
Colour	Visual	Silver Grey	
Density @ 26°C (79°F)	ASTM D 1475	2.44 g/mL	
Hardness	Shore D durometer	70D	
Tensile Strength	ASTM D 638	15 N/mm ²	(2200 lb/in ²)
Elongation	ASTM D 638	0.3%	
Compression Strength	ASTM D 695	39 N/mm ²	(5700 lb/in ²)
Shear Strength	ASTM D 732	1.6 N/mm ²	(230 lb/in ²)
Lap Shear Strength (Aluminium 5052)	ASTM D 1002	8.0 N/mm ²	(1 160 lb/in ²)
Izod Impact ^{b)}	ASTM D 256	1.7 kJ/mm ²	(0.80 ft * lb/in)
Flexural Strength	ASTM D 790	17 N/mm ²	(2500 lb/in ²)
Water Absorption	ASTM D 570	0.04%	
Outgassing (Total Mass Loss) @ 24 h	ASTM E 595	6.27%	
Water Vapor Release (WVR)	ASTM E 595	0.09%	
Collectable Volatile Condensable Material	ASTM E 595	0.16%	
Solderable		No	
Electric Properties	Method	Value	
Volume Resistivity ^{c)}	Method 5011.5 in MIL-STD-883H	0.007 × Ω * cm	
Thermal Properties	Method	Value	
Thermal Conductivity @ 25°C (77°F)	ASTM E 1461	0.903 W/(m*K)	
Thermal Conductivity @ 50°C (122°F)	ASTM E 1461	0.893 W/(m*K)	
Thermal Conductivity @ 100°C (212°F)	ASTM E 1461	0.813 W/(m*K)	
Glass Transition Temperature (T _g)	ASTM D 3418	50°C (122°F)	
Heat Deflection Temperature	ASTM D 648	48°C	
CTE ^{d)} Prior T _g	ASTM E 831	54 ppm/°C	
CTE ^{d)} After T _g	ASTM E 831	169 ppm/°C	

Note: Specifications are for epoxy samples that were cured at 65 °C for 15 minutes. Additional curing time at room temperature was given to allow for optimum curing. Samples were conditioned at 23°C and 50% RH prior to most tests.

^{a)} N/mm² = MPa; lb/in² = psi; ^{b)} Cantilever beam impact

^{d)} The uncured epoxy mixture does not conduct electricity well and can have high resistance. To attain stated resistivity, ensure that the mix ratio is followed and that the product is fully cured by heat curing. Room temperature cures may give higher resistivity.

^{d)} Coefficient of Thermal Expansion (CTE) units are in ppm/°C = in/in/°C × 10⁻⁶ = unit/unit/°C × 10⁻⁶

Silver Conductive Epoxy Adhesive, Moderate Cure / High Conductivity



Properties of Uncured MC002966

Physical Property	Mixture (1A:1B)	
Colour	Silver Grey	
Density a)	2.55 g/mL	
Mix Ratio by Volume (A:B)	1.0:1.0	
Mix Ratio by Weight (A:B)	1.2:1.0	
Solids Content (w/w)	93%	
Physical Properties	Part A	Part B
Colour	Silver Grey	Silver Grey
Density	2.46 g/mL	2.37 g/mL
Flash Point	>150°C (302°F)	>93°C (199°F)
Resistivity of uncured material	Off-scale (no reading)	Off-scale (no reading)

a) Calculated value based on measured densities of each part

Compatibility

Adhesion - As seen in the substrate adhesion table, the MC002966 epoxy adheres to many materials found on printed circuit assemblies; however, contaminants like water, oil, and greasy flux residues may affect adhesion. If contamination is present, clean the printed circuit assembly with electronic cleaner.

Substrate Adhesion in Decreasing Order

Physical Properties	Adhesion	
Aluminium	Stronger	
Steel	↓	
Fiberglass		
Wood		
Paper, Fiber		
Glass		
Rubber		
Polycarbonate		
Acrylic		
Polypropylene a)		Weaker

a) Does not bond to polypropylene

Storage

Store between 16 and 27°C (60 and 80 °F) in dry area away from sunlight. Prolonged storage or storage at or near freezing temperatures can result in crystallization. If crystallization occurs, reconstitute the component to its original state by temporarily warming it to 50 to 60°C (122 to 140°F). To ensure full homogeneity, stir thoroughly the warm component, reincorporating all settled material. Re-secure container lid and let cool down before use.

Application Instructions

Follow the procedure below for best results.

For mixing quantities that are less than 1 mL in size or for stricter stoichiometry control, mix by weight ratio instead (requires a high precision balance). Heat cure is recommended to get the best possible conductivity.

www.element14.com
www.farnell.com
www.newark.com



Silver Conductive Epoxy Adhesive, Moderate Cure / High Conductivity



To prepare 1:1 (A:B) epoxy mixture by volume

1. Remove syringe cap or jar cover.
2. For jars, stir each part individually to re-incorporate material that may have settled during storage.
3. Measure one part by volume of A.
4. Measure one part by volume of B.
5. Thoroughly mix the parts together with a stir stick until homogeneous.
6. Apply to with an appropriate sized stick for the application area.

NOTE: Remember to recap the syringe or container promptly after use.

TIP: Due to the high viscosity and abrasiveness of the silver filler, you may preheat part A and part B to increase the flow and improve air release, but doing so will also reduce the working time by about half for each 10°C increments.

To heat cure the MC002966 epoxy

Put in oven at 65°C (149°F) for 15 minute

TIP: Hair dryers are normally rated not to exceed 60 °C, so they can generally be used to accelerate the cure.

You can cure the epoxy faster by using higher temperatures of up to 150°C (302°F).

ATTENTION: Keep the curing temperature well below temperature limit of heat sensitive components that may be present. As a guideline, remember that commercial grade devices normally can be safely operated up to 70°C, industrial grade up to 85°C, and military grade up to 175°C.

ATTENTION: Heat guns can easily exceed the temperature limits for your assembly: they should not be used.

To room temperature cure the MC002966 epoxy

Let stand for 5 to 24 hours

TIP: While the product can be cured at room temperature, the better conductive performance is achieved with heat curing.

Packaging

Packaging	Net Volume		Net Weight	
Syringe	6mL	0.2 fl oz	14.4g	0.51 oz

Part Number Table

Description	Part Number
Silver Conductive Epoxy Adhesive, Moderate Cure/High Conductivity, 6mL, Syringe	MC002965

Important Notice : This data sheet and its contents (the "Information") belong to the members of the Premier Farnell group of companies (the "Group") or are licensed to it. No licence is granted for the use of it other than for information purposes in connection with the products to which it relates. No licence of any intellectual property rights is granted. The Information is subject to change without notice and replaces all data sheets previously supplied. The Information supplied is believed to be accurate but the Group assumes no responsibility for its accuracy or completeness, any error in or omission from it or for any use made of it. Users of this data sheet should check for themselves the Information and the suitability of the products for their purpose and not make any assumptions based on information included or omitted. Liability for loss or damage resulting from any reliance on the Information or use of it (including liability resulting from negligence or where the Group was aware of the possibility of such loss or damage arising) is excluded. This will not operate to limit or restrict the Group's liability for death or personal injury resulting from its negligence. Multicomp is the registered trademark of the Group. © Premier Farnell Limited 2016.

www.element14.com
www.farnell.com
www.newark.com

